STRUCTURE AND MECHANISM OF THE BACTERIAL TRANSPORTER LEUT

By

Chayne L. Piscitelli

A DISSERTATION

Presented to the Department of Biochemistry and Molecular Biology
and the Oregon Health & Science University
School of Medicine
in partial fulfillment of
the requirements for the degree of

Doctor of Philosophy

January 2011

School of Medicine

Oregon Health & Science University

CERTIFICATE OF APPROVAL

This is to certify that the Ph.D. dissertation of

Chayne L. Piscitelli

has been approved

Eric Gouaux, Mentor/Advisor

David Farrens, member

Buddy Ullman, member

Francis Valiyaveetil, member

Ujwal Shinde, member

TABLE OF CONTENTS

ACKNOWLEDGEMENTS

There are several people that I would like to explicitly acknowledge for their part in making this PhD possible.

First, I must thank my advisor, Dr. Eric Gouaux, for the astute guidance and support that he gave throughout my graduate studies. The quality of his scientific mentorship was absolutely essential in getting me where I am today.

I also thank the members of my research advisory and examination committees: Dr. David Farrens, Dr. Buddy Ullman, Dr. Francis Valiyaveetil, and Dr. Ujwal Shinde, for their time, patience, and dedication to their role as professors.

Much of the excellence in my training as a research scientist I attribute to the interactions with fellow members of the Gouaux lab. There are numerous individuals of extraordinary talent that have helped me out along the way, and I wholeheartedly thank all of them. In particular, I owe much gratitude to Dr. Satinder Singh, who, during my nascent years in the lab, dedicated a lot of her time to teach me the fundamentals necessary for my research and, along the way, taught me a lot about being a scientist.

Finally, I thank my wife, Kate, for her heroic patience while I finished graduate school. I am forever indebted for all that she has sacrificed during these past years, and I would not want to have done this without her as my teammate. Thank you, Kate.

Financial support for the work presented here came from Howard Hughes Medical Institute, National Institutes of Health, and the Oregon chapter of the Achievement Rewards for College Scientists scholarship program.

LIST OF ABBREVIATIONS

^{3}H	tritium
4-F-Phe	4-fluoro-phenylalanine
5-HT	5-hydroxytryptamine (serotonin)
A	alanine
Å	ångström (1.0 x 10^{-10} meters)
ADHD	attention-deficit hyperactivity disorder
ADP	adenosine 5'-diphosphate
ala	alanine
ALS	Advanced Light Source
arg	arginine
asp	aspartate
ATP	adenosine 5'-triphosphate
b.d.l.	below detection limit
BgT1	betaine/GABA transporter
C_{12}M	*n*-dodecyl β-D-maltoside
cDNA	complementary deoxyribonucleic acid
Ci	curie (3.7 x 10^{10} becquerels)
cm	centimeter
CMI	clomipramine
CPK	Corey-Pauling-Koltun
CPM	counts per minute
CT1	creatine transporter
D	aspartate
DAACS	Dicarboxylate/Amino Acid:Cation Symporter
DAT	dopamine transporter
DDM	*n*-dodecyl β-D-maltoside
DNP	2',4'-dinitrophenol
DPM	disintegrations per minute (0.0167 becquerels
DTT	dithiothreitol
EAAT	Excitatory Amino Acid Transporter
ED	equilibrium dialysis
EL	extracellular loop
F	phenylalanine
FSEC	fluorescence size exclusion chromatography
G	glycine
GABA	γ-amino butyric acid
GAT	GABA transporter
GlpT	glycerol 3-phosphate:phosphate antiporter
Glt$_{Ph}$	glutamate/aspartate transporter from *Pyrococcus horikoshii*
gly	glycine
GlyT1	glycine transporter
HEPES	4-(2-hydroxyethyl)-1-piperazineethanesulfonic acid
his	histidine
hNET	human norepinephrine transporter

HP	hairpin loop
I	isoleucine
IL	intracellular loop
ile	isoleucine
ITC	isothermal titration calorimetry
K	lysine
kDa	kilodalton
L	leucine
LacY	lactose permease
leu	leucine
LeuT	leucine transporter
LSC	liquid scintillation counter
lys	lysine
M	methionine
MDMA	3,4-Methylenedioxymethamphetamine
met	methionine
MetP	Na^+-coupled methionine and alanine transporter
MFS	Major Facilitator Superfamily
mg	milligram
Mhp1	hydantoin transporter (*Microbacterium liquefaciens*)
min	minute
mM	millimolar
mmol	millimole
mRNA	messenger ribonucleic acid
MWCO	molecular weight cutoff
NADH	nicotinamide adenine dinucleotide
NCS1	Nucleobase:Cation Symporter family 1
NE	norepinephrine
NhaA	Na^+/H^+ antiporter 1
NiNTA	nickel nitrilotriacetic acid
nM	nanomolar
nm	nanometer
NSLS	National Synchrotron Light Source
NSS	Neurotransmitter:Sodium Symporter family
PDB	Protein Data Bank
PEG	polyethylene glycol
pmol	picomole
ProT	proline transporter (human)
PutP	proline transporter (bacteria)
Q	glutamine
qAAA	quantitative amino acid analysis
R	arginine
RMSD	root mean squared deviation
RND	Resistance, Nodulation, Cell Division family
s.e.m.	standard error of the mean
SAD	single-wavelength anomalous dispersion

SCAM	substituted cysteine accessibility method
SDS-PAGE	sodium dodecyl sulfate-polyacrylamide gel electrophoresis
SEC	size exclusion chromatography
SeMet	seleno-methionine
SERT	serotonin transporter
SGLT1	sodium-coupled glucose transporter (human)
SLC5	solute carrier 5 family
SLC6	solute carrier 6 family
SMD	steered molecular dynamics
SNRI	serotonin and norepinephrine reuptake inhibitor
SPA	scintillation proximity assay
SSRI	selective serotonin reuptake inhibitor
SSS	Sodium:Solute Symporter family
T	threonine
TauT	taurine transporter
TBOA	DL-*threo*-β-benzyloxyaspartic acid
TC	transport commission
TCA	tricyclic antidepressant
TCEP	tris(2-carboxyethyl)phosphine
TM	transmembrane
TnaT	Na^+-coupled tryptophan transporter (*Symbiobacterium thermophilum)*
Tris	tris(hydroxymethyl)aminoethane
trp	tryptophan
tSIE	transformed spectral index of external standard
tyr	tyrosine
TyT1	Na^+-coupled tyrosine transporter (*Fusobacterium nucleatum)*
UTR	untranslated region
V	valine
val	valine
VMAT	vesicular monoamine transporter
vSGLT	Na^+-coupled galactose transporter (*Vibrio parahaemolyticus)*
W	tryptophan
Y	tyrosine
β-ME	β-mercaptoethanol
β-OG	*n*-octyl-β-D-glucopyranoside
μg	microgram
μL	microliter
μM	micromolar
μm	micrometer

ABSTRACT

The mechanism of ion-coupled secondary transport is universally utilized in every kingdom of life to catalyze the concentrative uptake of molecules across cellular membranes. Ion-coupled transporters are central to many physiological functions ranging from nutrient uptake to neural synaptic transmission. Recently, the crystal structure of the ion-coupled transporter LeuT, a bacterial homolog of the Neurotransmitter:Sodium Symporter (NSS) family, was solved. This structure revealed a novel transporter motif characterized by an internal 2-fold structural repeat, with the substrate L-leucine and two sodium ions bound in a centrally located occluded binding site, suggestive of an alternating access transport mechanism. To date, LeuT presents one of only a small handful of sodium-coupled secondary transporters structures, and remains the only NSS transporter to have yielded to crystallographic studies. LeuT has therefore become widely used as the structural blueprint for modeling and interpreting the structure, function, and pharmacology of the human NSS members which include the monoamine transporters for serotonin, dopamine, and norepinephrine. Insights into transporter mechanism from LeuT and the quality by which it can be used as a modeling template depend deeply upon our knowledge of the structure and function of LeuT itself. Thus, in an effort to further understand the structural principles of LeuT transport, we have undertaken more detailed studies of LeuT structure and function.

In this dissertation, I present the experiments, results, and conclusions from crystallographic and functional investigations of LeuT. In these studies, we probe

the structure and mechanism of LeuT using transport and binding assays together with X-ray crystallography with different substrates and mutations. We show that LeuT binds and transports aliphatic and aromatic amino acids, and that binding of transportable substrates results in the stabilization of an occluded conformation. Transport is competitively inhibited by L-tryptophan, which traps the transporter in an open-to-out conformation and has tryptophans bound both in the central binding site and at a second site that opened up in the extracellular permeation pathway. Though this open state has two apparent binding sites, detailed measurements show that the occluded state, by contrast, harbors only a single high-affinity substrate binding site. Further work identified a mutation that allows LeuT to transport L-tryptophan and we show that this gain of function corresponds to the ability of LeuT to form the occluded state with tryptophan bound only in the central binding site. These data together suggests that the occluded state is a necessary intermediate in the transport mechanism, and that the second site identified in the open-to-out state is likely a low-affinity site transiently occupied during substrate permeation. Our findings are used to construct a structural description of the alternating access mechanism for the transport cycle of LeuT, which we believe contains general principles that provide insights into how other structurally and functionally related transporters work.

Chapter 1

Introduction and Fundamental Concepts

Crossing the membrane

In every kingdom of life, cells are bounded by lipidic bilayered membranes that separate the intracellular components from the external environment. While hydrophobic compounds may passively diffuse through cellular membranes, most ions and polar molecules cannot. Membranes thus form a barrier impermeant to most substances needed to sustain life. To rectify this, embedded within membranes are a vast array of proteins that facilitate the selective transfer of solutes across the lipid bilayer. These proteins enable and regulate the flux of ions, nutrients, waste products, and signaling molecules, often acting as gate and gatekeeper together to promote and maintain the function of the cell.

These transmembrane proteins are dynamic machines that operate by a number of thermodynamically and physically distinct mechanisms. The primary mechanistic distinction that classifies most of these transmembrane machines is derived from the kinetic profile of the solute flux that the protein facilitates. Steady-state flux rates are often observed to have either a simple linear dependence on solute concentration or the flux exhibits a more complex concentration-dependence characterized by an asymptotically saturating steady-state flux rate [1]. The former kinetic observation is characteristic of "channel" proteins, which is distinct from the latter that is characteristic of "transporter" proteins.

The simple kinetics of channel proteins reflect an underlying mechanism that serves to facilitate diffusion of a chemiosmotic solute gradient. The direction and magnitude of flux will be dictated by the direction and magnitude of the chemiosmotic (or electrochemical potential) gradient [2]. Channel proteins, in essence, are pores in the membrane that selectively allow solutes to diffuse in and out of the cell; however they may also be gated to provide temporal control over the opening of the pore, effectively changing the stochastic probability that any single channel will open [3]. Channel gating can be responsive to a number of stimuli including activation by ligand binding, voltage sensing, mechano-sensory transduction, or photon absorption. Furthermore, gating kinetics can be modulated to control the rate of solute flux, for example, via secondary ligand binding, which may stimulate or depress gating, or by temporal desensitization, which decouples the gating stimulus from pore opening, leading to pore closure during prolonged stimulation. Generally, the kinetics of solute flux through channels is described by terms analogous to electrical circuits: Solute flux, or single channel current, is proportional to the unitary conductance (the product of the open probability of the channel and the maximal conductance) and the chemical/electrochemical potential established across the membrane.

In contrast to channels, the saturable kinetics of transport proteins underscores the notion that transporters are more akin to enzymes and are, in fact, well-characterized by kinetic enzyme models [1] (**Figure 1.1**). Instead of simply serving as a gated pore that facilitates diffusion across the membrane, transporters methodically transfer solute from one side of the membrane to the other by coordinating the binding and releasing of solute to conformational changes in the protein structure that alternately exposes the substrate binding site to opposite sides of the membrane [4-8] (**Figure 1.2**). In this manner, transporters can exert an exquisite amount of structural control over the flux and selectivity of the transport process. This attribute permits transporters to couple solute flux to exergonic processes which effectively enables the transporter to pump solutes against chemiosmotic and electrochemical potential gradients.

Most transporters do act as pumps and thus are called “active” transporters to differentiate from passive transport mechanisms where solute flux is not coupled to the energetics of a second process. Active transporters are classified in two categories: primary active transporters and secondary active transporters. Primary active transporters are so-called because they harbor the ability to directly use a primary source of energy such as phosphodiester bond hydrolysis (e.g. ATPase activity), decarboxylation, oxidoreduction (e.g. NADH reductase or cytochrome c oxidase activity), or photon absorption to drive an otherwise thermodynamically unfavorable translocation of solute across the membrane [9-11]. Coupling enzymatic activity, such as the phosphodiesterase activity utilized in the majority of primary active transporters, to selective transport means that primary transporters are dual-function transmembrane proteins and are often assembled as multi-domain oligomers [12].

One key role of primary active transporters in cell physiology is to establish and maintain the ionic electrochemical gradients across the plasma and organelle membranes. These electrochemical gradients effectively store the chemical energy used by primary transporters as potential energy across the membrane. This transmembrane potential energy is a “secondary” energy source for the cell, and is harnessed by secondary active transporters to drive solute translocation. In a general sense, secondary transporters are thus “thermodynamic couplers” that can convert the energy released from the exergonic movement of one solute across the membrane to the endergonic movement of a second solute.

Secondary transporters encompass an incredibly diverse collection of proteins, with approximately 100 families identified, genetically disparate, with distinct solute (substrate) specificities (www.tcdb.org) [10, 11]. The majority of the known secondary transporters are cation-coupled, utilizing either Na^+ or H^+ gradients to drive solute transfer; however a small number of transporters are driven by gradients of K^+, Cl^-, OH^-, or inorganic phosphate [10]. The coupling of gradient discharge to solute flux can be either "symport", where ion and solute flow in the same direction, or "antiport", where ion and solute flow in opposite directions across the membrane (**Figure 1.3**). Though ion:solute symport or antiport is the most common general mechanism for secondary transport, concentrative uptake can also be accomplished by solute:solute antiport (e.g. the mitochondrial ATP:ADP exchanger family, TC #2.A.29). Solute:solute antiport and phenomena related to solute exchange will be discussed in greater detail later.

Sodium-coupled secondary transport

In 1952, Christensen *et al*. observed that erythrocytes can concentrate amino acids from the extracellular solution, and that the transport activity is dependent on the presence of sodium [13]. They noted that the activity was curiously insensitive to respiration inhibitors such as azide, cyanide, arsenate, and 2,4 dinitrophenol (DNP). The idea that sodium is coupled to active transport was nascent at the time and the significance of the apparently respiration-uncoupled mechanism had yet to be appreciated. This was around the same time that Hans Ussing was working out the basis of active sodium transport in frog skin epithelial cells, identifying that Na^+ and K^+ are actively exchanged across frog skin preparations against both electrical and chemical concentration differences [14, 15], and that the transport is tightly coupled to respiration, being strongly inhibited by DNP, and requiring an almost stoichiometric consumption of O_2 [16, 17]. The active Na^+/K^+ exchange activity in frog skin was indeed identified as an ATPase-coupled pump [18] (TC #3.A.3.1.1). Thus, finding Na^+-coupled active transport that was apparently independent of respiration was a harbinger of the underlying mechanistic divergence from primary and secondary sodium-coupled transport.[1]

In addition to Christensen's observations of concentrative amino acid uptake, the phenomenon of sodium-driven substrate flux was also being observed for glucose uptake into cells. Early studies examining glucose transport showed that glucose uptake is sodium dependent and well-described by Michaelis-Menten kinetic parameters [1, 19]. Using excised frog intestines, Csaky and Thale showed that the direction of the sodium gradient is critical for transfer of the non-metabolizable analog 3-methylglucose across epithelial tissue [20]. A flurry of research thereafter quickly established that sodium indeed drives uptake of amino acids, glucose, and other essential nutrients (reviewed in [21]), placing sodium-coupled secondary transporters as key elements to many central physiological processes.

In 1987 Matthias Hediger and Ernest Wright developed the technique of expression cloning to successfully identify the cDNA of the rabbit Na^+/glucose

---

[1] It is of interest to note that the Na^+K^+ ATPase is also in fact the main primary active transporter that maintains that transmembrane Na^+ gradient utilized by sodium-coupled secondary transport processes.

cotransporter, which was the first mammalian co-transporter to be cloned [22]. With cDNA in hand, they subsequently identified the human Na^+/glucose transporter SGLT1 (TC #2.A.21.3.1) [23], which opened up the rapid identification of genetic polymorphisms that underlie disease states [24]. More recently, in 2008, the crystal structure of a prokaryotic homolog of SGLT1, the sodium/galactose co-transporter from *Vibrio parahemolyticus* (vSGLT), was solved bound with galactose and sodium [25]. The vSGLT crystal structure and its mechanistic implications are discussed more extensively in Chapter 5 of this dissertation.

Neurotransmitter uptake by sodium-coupled secondary transporters

Around the same time that amino acid and glucose transport was being discovered to be sodium dependent, Axelrod and colleagues were studying the mechanism by which neurotransmitter signaling is terminated. In 1961, Whitby, Axelrod, and Weil-Malherbe reported on experiments that followed the tissue-specific accumulation of injected [^{3}H]-norepinephrine (NE) [26]. They found that [^{3}H]-NE is rapidly absorbed into tissues within two minutes after injection, and is particularly localized to the heart, spleen, and adrenal gland, and that the sites for tissue absorption are likely to be localized to nerve endings, as binding of catchecolamines to tissues is dependent upon intact sympathetic nerve endings [27]. Shortly thereafter, L.L. Iversen reported on a series of elegant kinetic assays measuring [^{3}H]-NE uptake in rat heart perfusions. These assays showed that [^{3}H]-NE is concentrated into tissues by a stereospecific mechanism that obeys Michaelis-Menten kinetics (**Figure 1.4**). Iversen also demonstrated that cocaine inhibits [^{3}H]-NE uptake dose-dependently, with an $EC_{50} \sim 0.5 - 1\ \mu M$ (**Figure 1.4**) [28]. A few years later Iversen and Kravitz demonstrated that norepinephrine uptake at nerve terminals is sodium-dependent, and predicted that the uptake of the neurotransmitters γ-amino butyric acid (GABA) and glutamate is also sodium-dependent [29]. Subsequently, Iversen and Neal showed that GABA is in fact rapidly transported into rat cerebral cortex slices by an active transport process well described by Michaelis-Menten kinetics and is steeply dependent on the external sodium concentration [30].

In the same time period, tissue-specific uptake of the neurotransmitter 5-hydroxytryptamine (5-HT, serotonin) was also being examined. Early studies examining neuronal uptake observed that 5-HT appeared to be transported by a 5-HT specific system that is inhibited by cocaine, amphetamine, and desipramine [31, 32]. It was also observed that blood platelets contain a high affinity transport system for 5-HT. Blood platelet uptake of 5-HT also demonstrated a saturable [33] and specific sodium-dependent active transport system [34] that is inhibited by tricyclic antidepressants such as imipramine and clomipramine [35, 36]. By 1970 it was widely accepted that neurotransmitters are rapidly cleared from synaptic and extraneuronal spaces by specific sodium-dependent transport systems, and that this functioning is central to the physiology of neurons.[2] It was also becoming clear that a rich pharmacological profile existed for these transporters, and that inhibition of transmitter uptake could be used to potentiate neuronal signaling [37].

---

[2] While the signaling by biogenic amine and amino acid neurotransmitters is terminated directly by synaptic reuptake transporters, signaling by the neurotransmitter acetylcholine is instead terminated by enzymatic cleavage via synaptic acetylcholinesterase activity. The resulting choline product is then transported back into neurons by a sodium-cotransporter.

The neurological and pharmacological importance of neurotransmitter transporters spurned significant efforts towards structural and functional characterization. In the 1970's, the use of isolated membrane vesicles was pioneered by Kaback [38, 39], which allowed researchers to study native membranes with greater control over the conditions on either side of the membrane. Thus, vesicles could be reconstituted with different internal and external solutions with tailored gradients, permitting detailed studies of ion-coupled transport activity in the absence of confounding factors such as cytoplasmic metabolic activity. Using this type of system, the naturally abundant transporters for GABA and 5-HT were studied using vesicles derived from either rat brain neurons for GABA transport studies [40-42], or blood platelet cells for 5-HT transport studies [43].

From native membrane vesicle preparations, the stoichiometry of GABA transport was observed to require the symport of 2 Na^+ ions for one molecule of GABA. The transporter was also found to co-transport Cl^-, acting as an allosteric enhancer of sodium binding [40, 44, 45]. Because the transport of GABA results in the net movement of one positive charge across the membrane, transport is electrogenic and thus sensitive to the membrane electrical potential. By contrast, 5-HT transport is driven by the co-transport of two Na^+ ions and one Cl^- ion, with the counter-transport of one K^+ ion. Thus, the overall mechanism for 5-HT transport is electroneutral [46].

Cloning of neurotransmitter transporters defines the NSS family

Studies of GABA and 5-HT transport in membrane vesicle preparations led to more sophisticated experimental approaches to measure transporter function [47, 48], and the ability to functionally purify transport activity [49]. This led to the landmark paper in 1990 which reported the first cloning of a neurotransmitter transporter, the GABA transporter GAT-1, by Baruch Kanner's group in collaboration with Henry Lester's lab [50]. From highly purified GABA transporter protein, cyanogen bromide digestion fragments were sequenced and used to design oligonucleotide probes for the GABA transporter gene. Rat brain cDNA libraries were screened with these probes by colony plaque hybridization techniques. From this they identified two positive colonies, one of which yielded mRNA that produced GABA transport activity when expressed in *Xenopus* oocytes.

Shortly after GAT-1 was cloned, in 1991 Susan Amara's group reported the cloning of the gene for the human norepinephrine transporter, hNET, using an expression cloning technique similar to that used by Hediger and Wright to clone the Na^+/glucose co-transporter [51]. Strikingly, hNET showed 46% sequence identity (68% similarity) to GAT-1 and contained a 20 residue stretch near the N-terminus (residues 78-98) that was completely identical, save for one single substitution at residue 87. Thus, the identification of GAT-1 and hNET together founded a family of neurotransmitter transporters that will become known as the NSS – Neurotransmitter Sodium Symporter - family.

Using the sequence alignments between GAT-1 and hNET, degenerate oligonucleotide probes were constructed to identify cDNA fragments encoding related transporter genes. Within an extremely rapid timeframe, the rat dopamine transporter (DAT) from was cloned [52, 53], followed by the serotonin transporter (SERT), also from rat [54, 55]. The NSS family grew to encompass neuronally-localized sodium-coupled transporters for most of the major neurotransmitters such as the amino acids GABA (GAT-1, GAT-2, and GAT-3), glycine (GlyT1), and proline (ProT), and the biogenic amine transmitters dopamine (DAT), norepinephrine (NET), and serotonin (SERT). Other NSS members include the transporters for the osmolytes taurine (TauT), creatine (CT1 and CT2), and betaine (BgT1 and BgT2), and several distinct gut epithelial transporters for the absorption of neutral and cationic amino acids. Bacterial homologs of the NSS family have also been discovered, including a tryptophan transporter (TnaT) [56], tyrosine transporter (TyT1) [57], methionine and alanine transporter (MetP) [58], and the primary subject of this dissertation: the aliphatic and aromatic amino acid transporter LeuT [59].

Disease and pharmacology of NSS family members

The enormous complexity of central nervous system diseases have proven difficult to demarcate according to specific functional polymorphisms in genes of known function. Nevertheless, several of the NSS family transporters have been directly associated with diseases, particularly mental disorders (reviewed in [60]), and are the principle targets for therapeutic interventions using a wide array of drug compounds. Of particular interest are the serotonin, norepinephrine, and dopamine transporters (SERT, NET, and DAT).

Serotonin is a key regulator of basic physiological functions such as mood, appetite, sleep, cognition, and sexual activity. As such, serotonin imbalance is implicated in a myriad of mental illnesses including depression, anxiety, autism, obsessive-compulsive disorder, and schizophrenia. Genetic polymorphisms in SERT have been linked to several of these disorders and are associated with aggravated impulsiveness and novelty-seeking type behaviors. Elevated expression of SERT has also been identified with certain types of alcoholism.

Norepinephrine and NET polymorphisms are implicated in attention-deficit hyperactivity disorder (ADHD) and depressive syndromes and are regulators for attention, memory, and learning. Norepinephrine is also a major neurotransmitter of the sympathetic nervous system and plays a role in regulating heart rate, blood pressure, and vascular tone. Decreased NET function is found in patients with orthostatic intolerance (marked by the inability to maintain blood pressure when transitioning ones posture from sitting to standing).

Dopamine uptake by DAT regulates motor functions, mood, and reward. DAT dysfunction is also implicated in ADHD, schizophrenia, bipolar disorder, autism and Parkinson's disease. Nonsynonymous polymorphisms encoding mutant DAT proteins are linked to bipolar disorder and ADHD. Polymorphisms in the 3' UTR of DAT mRNA has been observed to affect expression levels of DAT in association with alcoholism, drug abuse, and ADHD.

Among the first compounds developed to target monoamine transporters were the tricyclic antidepressants (TCAs). TCAs are generally based on the three-ringed dibenzazapine structure with various alkyl and halogen substituents to tune the activity of each compound (**Figure 1.5**). Examples of prescribed TCAs include imipramine, clomipramine, desipramine, nortryptyline, and amitryptyline. TCAs are potent inhibitors of SERT and NET with K_i values in low nanomolar range [61]. TCAs are effective in treating depression and other syndromes related to decreased serotonergic signaling, however the therapeutic usefulness of TCA compounds are limited by the range of severe side-effects. In addition to potent SERT and NET inhibition, TCA's antagonize neurotransmitter receptors at therapeutic concentrations, including $5HT2_A$, histamine H_1, muscarinic M_1, and α_1- and α_2-adrengergic receptors. This broad receptor antagonist activity is thought to account for the number of harsh side-effects of TCAs.

To combat this, a second generation antidepressants were developed – the so-called selective-serotonin reuptake inhibitors (SSRIs). These include some the most highly prescribed psychiatric drugs in history such fluoxetine (Prozac), sertraline (Zoloft), and citalopram (Lexapro). The chemical structures of SSRIs vary (**Figure 1.5**), and are classified together based on their moderate selectivity for SERT over NET inhibition. SSRIs inhibit SERT with low nanomolar affinity but can inhibit NET in the low micromolar range, thus showing about 1000 fold selectivity for SERT over NET. An exception is citalopram, which is highly selective for SERT and does not bind either NET or DAT to any significant extent. SSRIs are poor ligands for neurotransmitter receptors (K_d values are generally in the micromolar range for the receptors that potently antagonized by TCAs) and thus have reduced clinical side-effects compared to TCAs.

Though SSRIs are safer than TCAs, they are less efficacious for treating depression due to weak NET inhibition. A related class of drugs similar to SSRIs were developed that, like TCAs, are selective for SERT as well as NET, but without the broad receptor antagonism effects. These serotonin and norepinephrine reuptake inhibitors (SNRIs) include venlafaxine (Effexor), and duloxetine (Cymbalta) (**Figure 1.5**). SNRIs exhibit low to mid nanomolar K_i values for SERT and NET, and have a similar side-effect profile as SSRIs.

The dopamine transporter DAT is a principal target for psychostimulant drugs such as methylphenidate (Ritalin), cocaine, and amphetamines including 3,4-methylenedioxyamphetamine (MDMA, "ecstasy") (**Figure 1.5**). Methylphenidate, a piperadine derivative, is a DAT and NET inhibitor that is widely prescribed for the treatment of ADHD in children. K_i values for DAT and NET inhibition are around 60 and 100 nM, respectively. Cocaine also potently inhibits DAT uptake (K_i = 230 nM) as well as NET (K_i = 480 nM) and SERT (K_i = 740 nM), though the intense reward conditioning of cocaine administration is generally attributed to effects on the dopamine pathway. While methylphenidate and cocaine are non-transportable inhibitors of dopamine uptake, amphetamine and its congeners, including methamphetamine, are instead transportable substrates for DAT. Amphetamines compete with both DAT and NET uptake with K_i values around 100 – 700 nM and weakly inhibit SERT with K_i around 30 – 40 μM.

The primary effect of amphetamines, in addition to competing with neurotransmitter reuptake, is to induce DAT-dependent dopamine efflux from cells [62] thereby causing a rapid increase in the extracellular dopamine concentration. Serotonin release via amphetamine-induced SERT efflux has also been observed [63]. The precise mechanism of this induced efflux is not entirely clear, however it is thought to involve the release of monoamine neurotransmitter from filled presynpatic vesicles via the H^+-coupled vesicular monoamine transporters (VMATs) [64], interactions of DAT with syntaxin 1A [65], phosphorylation-dependent regulation of DAT via protein kinase C [66], and calmodulin-dependent kinase II [67].

Transport kinetics and thermodynamic coupling

The ion:solute stoichiometry and electrogenicity of transport are key determinants of the extent to which solute can be concentratively transported and the steady-state rate of transport. Considering the chemical reaction scheme for the simple transport of *a* moles of solute S coupled to the symport of *b* equivalents of sodium ion Na^+:

$$aS_{out} + bNa^+_{out} \rightarrow aS_{in} + bNa^+_{in}$$

When *a* or *b* is equal to one, the steady-state rate of transport will be hyperbolic with respect to the concentration of S_{out} or Na^+_{out}, respectively. For example, when $a = 1$ and sodium is not limiting, the rate, or transport velocity, V, as a function of $[S_{out}]$ is given by the Michaelis-Menten equation:

$$V = \frac{[S_{out}]V_{max}}{[S_{out}] + K_M}$$

It is commonly the case that $a = 1$ while $b > 1$. For $b > 1$, when solute is not limiting, transport may exhibit a sigmoidal response as a function of Na^+ concentration and is modeled by the Hill equation:

$$V = \frac{V_{max}[Na^+_{out}]^n}{[Na^+_{out}]^n + (K_M)^n}$$

where *n* is the Hill coefficient. *n* will approach *b* with increasing positive cooperativity of Na^+ binding. It is important to note that the manifestation of stoichiometry in the steady-state rate profile is dependent on this degree of cooperativity. When cooperativity is low, at low sodium concentrations a mixed population of transporters with fractional occupancy (occupancy less than *b* sites per transporter) of sodium sites will exist in equilibrium with fully occupied transporter, thereby "flattening" the sigmoidal response at the lowest concentrations to more closely resemble a hyperbolic response. In this case, the kinetics are better modeled by an ordered binding equation that gives explicit treatment for each fractionally occupied transporter specie. For the case when $b = 2$, the two-site ordered binding equation for velocity V as a function of sodium concentration Na_{out} is:

$$V = \frac{V_{\max} \dfrac{[Na^{+}_{out}]^2}{\alpha K^{2}_{Na}}}{1 + \dfrac{[Na^{+}_{out}]}{K_{Na}} + \dfrac{[Na^{+}_{out}]^2}{\alpha K^{2}_{Na}}}$$

where K_{Na} is an intrinsic dissociation constant for the single-occupied transporter term (i.e. the first Na^+ binding to the empty transporter), and α is the coefficient that modifies K_{Na} for the double-occupied transporter term (i.e. the second Na^+ binding subsequently to the single-occupied Na^+-transporter complex) and is related to the extent of binding cooperativity. For highly cooperative systems, α decreases, reflecting a lower intrinsic dissociation constant (i.e. a reduced αK_{Na} term) for the double-occupied transporter. For zero cooperativity, $\alpha = 1$, thus $\alpha K_{Na} = K_{Na}$ (the intrinsic dissociation for the single- and double-occupied states are the same), however the curve will maintain a sigmoidal shape equivalent to the Hill equation with n=1.25 (reference [68]). Kinetics arising from ordered two-site binding, whether cooperative or not, can therefore still be distinguished from simple single-site kinetic phenomenon.

These kinetic models require that the measured rate is dependent only on the concentration of either ion or solute, i.e. the experimental conditions are such that one specie is held in constant excess (at saturating concentration that does not appreciably change during the time period over which transport is measured) while the rate of transport is measured as a function of the other. This condition allows transport to be modeled using these simple bi-molecular kinetic models in which velocity is only dependent on enzyme (transporter) and one substrate concentration and assumes that the excess background substrate is in rapid equilibrium with the enzyme and can be kinetically ignored. From such a model, we are assuming that transport is approximated by the Briggs-Haldane model (shown here converted to relevant transporter terms), where the TS_{out} and TS_{in} species are assumed to be in steady-state:

$$T + S_{out} \underset{k-1}{\overset{k1}{\rightleftarrows}} TS_{out} \underset{k-2}{\overset{k2}{\rightleftarrows}} TS_{in} \xrightarrow{kcat} T + S_{in}$$

In practice, modeling transport by this type of scheme works, however the interpretation of K_M and V_{max} (or k_{cat}) from transport rate measurements must consider the simplicity of these assumptions and that the true kinetic model for transport may be much more complex. Most secondary transporters probably pass through several kinetically-relevant intermediates consisting of different transporter conformations, and ion and solute bound states. For sure, the above scheme does not faithfully illustrate the structural transitions of the transporter that are necessary to shuttle S_{out} to S_{in}, the ion or solute effect on stabilizing conformational intermediates, and the conformational transition(s) that recycles the transporter back to the initial state.

Indeed, recycling of empty transporter back to a state that is competent to bind S_{out} can be rate limiting to the overall transport process. For instance, in SERT Na^+ symport influx kinetics are stimulated by K^+ antiport activity that facilitates transporter recycling. It has also been observed for some transporters (i.e. GAT-1) [41] that the flux rate of labeled substrate is actually potentiated by the presence of unlabeled substrate on the opposite side of the membrane ("trans stimulation"), which leads to the rapid equilibration of unlabeled and labeled substrate across the membrane. Such observations can be explained by a substrate exchange mechanism where, following the release of labeled substrate, unlabeled substrate binds and is reverse-transported back to the other side of the membrane. Thus the conformation of the transporter is shuttled back and forth by labeled substrate on one side and unlabeled substrate on the other side, avoiding the otherwise rate-limiting empty-carrier turnover step.

While ion:substrate:transporter stoichiometry may or may not be obscured in kinetic measurements of transport, it is, in theory, inextricably linked to the thermodynamic profile of substrate accumulation. The extent to which substrate can be transported against its concentration gradient is directly determined by the ion coupling stoichiometry ratio and the relative "downhill" potential energy (i.e. chemical and/or electrical potentials stored in the driving ion gradient) that the transport mechanism can harness to counterbalance substrate gradient and "push" substrate “uphill” across the membrane. For an uncharged substrate, the chemical potential gradient, $\Delta\mu_S$, that must be overcome for inward transport is determined by it’s molar concentration ratio across the membrane:

$$\Delta\mu_S = RT \ln \frac{[S_{in}]}{[S_{out}]}$$

where R is the ideal gas constant and T is temperature in Kelvin.

The full electrochemical potential energy available in an ionic gradient across the membrane, $\Delta\mu_{Na}$, is given by:

$$\Delta\overline{\mu}_{Na} = RT \ln \frac{[Na_{in}]}{[Na_{out}]} + zF\Phi$$

where *z* is the charge on the ion (obviously *z* = 1 for sodium), *F* is the Faraday constant, and Φ is the electrical potential across the membrane. In essence, the *raison d’être* of a secondary active transporter is to combine $\Delta\mu_S$ and $\Delta\mu_{Na}$ together. For the symport reaction scheme stated above, the reaction energy $\Delta\mu_{rxn}$ is given by:

$$\Delta\widetilde{\mu}_{rxn} = a\Delta\mu_S + b\Delta\overline{\mu}_{Na}$$

At equilibrium, $\Delta\widetilde{\mu}_{rxn} = 0$, thus $a\Delta\mu_S = -\ b\Delta\overline{\mu}_{Na}$. This shows that if transport is allowed to reach equilibrium, then the electrochemical energy in the driving ion gradient will build a substrate gradient with a chemical energy equal to the electrochemical ion gradient multiplied by the stoichiometric ratio *b/a*. Therefore, theoretically (in the absence of ion leaks or transport “slippage”), the ion:substrate transport stoichiometry is will be a major determinant in the equilibrium concentrations, and the maximal extent to which substrate is accumulated in the cell. It is important to note that transport stoichiometry should be discriminated from binding stoichiometry. Ions or substrate may bind with stoichiometries different from the ratios in which they are transported across the membrane.

The crystal structure of LeuT

The bacterial NSS homolog LeuT, though distantly related to the eukaryotic neurotransmitter transporters, has recently become the subject of thorough investigations – and the subject to which the rest of this thesis is devoted. LeuT is a transporter from the hyperthermophilic bacterium *Aquifex aeolicus* and contains 20-25% sequence identity to the human NSS transporters [59, 69]. It is a sodium-coupled amino acid symporter, shares the same predicted 12 transmembrane (TM) helix topology, and is highly conserved in the regions of functional importance, including substrate and ion binding sites. It is therefore thought to operate by the same mechanistic principles as the other family members. In 2005, the crystal structure of LeuT was solved [59] providing the first and, to date, only blueprint for the architecture of an NSS family member. Thus, LeuT provides us with the ability to study the intimacies of NSS structure and function by combining crystallographic observations with functional experimentation to better understand the mechanism of transport.

The original LeuT structure revealed a completely novel protein fold characterized by a mostly α-helical secondary structure arranged as a bundle of 12 TM helices (**Figure 1.6A**). A notable feature of the TM helix arrangement is the formation on the extracellular side of the transporter a solvent accessible opening or depression that dips into the transporter nearly halfway into the transmembrane region (**Figure 1.6B**). The high resolution to which the crystals diffracted (1.65 Å) permitted the unambiguous identification of a molecule of L-leucine and two Na^+ ions bound near the base of this extracellular “vestibule” in the center of the transporter (**Figure 1.6B**). The binding sites for leucine and sodium are occluded from extracellular solvent by the side chains of just two residues, Y108 and F253, which lie at the base of the extracellular vestibule, thus forming a “thin” gate over the top of the substrate. By contrast, substrate is occluded from access to intracellular solvent by about 20 Å of ordered protein structure. The observation of the substrate binding site lying occluded at the base of an extracellular vestibule suggested that the structure was of an intermediate state of transport, which is dubbed as the “occluded state”. This notion implies that the transporter must therefore undergo conformational changes that alternately open and close the binding site to extracellular and intracellular permeation paths. The presence of an occluded state in the transport cycle demands that transporter must also transit through “open-to-out” and “open-to-in” states as part of the mechanism.

Insight into the nature of ion and substrate coupling was also revealed by the structure of LeuT. Two sodium ions are bound: one is coordinated completely by protein structure (Na2) between TM helices 1 and 8; however the other (Na1) is coordinated not only by protein structure, between TM helices 1 and 6, but also by a carboxylate oxygen from the bound leucine molecule (**Figure 1.7**). This demonstrates that ion-substrate coupling is reliant, at least in part, on the coordinated binding of ion and substrate.

The substrate binding site is formed by TM helices 1 and 6 on one side and TM helices 3 and 8 on the other side (**Figure 1.7**). In the region proximal to the ion and substrate binding sites, TM helices 1 and 6 are unwound and significantly kinked [70], which allows mainchain atoms to participate in hydrogen bonding interactions with the α-amino and carboxylate groups of the bound leucine. The aliphatic sidechain of bound leucine interacts with hydrophobic sidechains of residues in TM helices 3, 6 and 8. The substrate binding site can be broken down into two structural halves, with the polar amino and carboxylate groups coordinated by Na1 and the kinked region of TM helices 1 and 6 on one half, and the other half formed by the hydrophobic interactions of the aliphatic group with sidechains from TM helices 3 and 8. In this view, the substrate therefore bridges the two halves of the binding site.

The structure of LeuT also showed how the arrangement of residues that are highly conserved in the NSS family are important to function. Across the family, TM helices 1 and 6 are particularly enriched with conserved residues, and in LeuT these regions share roughly 50% sequence identity with human NSS members [59, 69]. The crystal structure revealed that many of the residues conserved in TM helices 1 and 6 are observed to either be directly involved in substrate and/or ion binding, or participate in interaction networks with other highly conserved residues to form putative extracellular and intracellular permeation pathway “gates”. On the extracellular side of the substrate binding site, R30 in TM helix 1 is strictly conserved and forms a water-mediated electrostatic bridge with the similarly conserved D404 in TM helix 10 (**Figure 1.8**). The R30-D404 bridge is located near the base of the extracellular vestibule directly above the aforementioned “thin gate” residues Y108 and F253 in TM3 and TM6 respectively, both of which are also highly conserved. The guanidinium group of R30 lies co-planar with the phenyl ring of F253 and is hydrogen-bonded with conserved Q250, which is one helical turn above F253 in TM helix 6 (**Figure 1.8**). Thus, a highly conserved extracellular interaction network is formed that appears to bridge the two “halves” of the transporter together. It is hypothesized that this network forms an extracellular gate that open up the bridge between R30 and D404 to allow substrate to permeate into the substrate binding site and then closes again to stabilize the occluded state. This notion is expounded upon in the following chapters.

On the intracellular side, a similarly organized highly conserved element is found, suggestive of an intracellular gate. Conserved residue R5 in TM helix 1 forms a direct salt-bridge with conserved D369 in TM helix 8. The hydroxyphenyl ring of Y268, also strictly conserved, lies co-planar to the guanidinium group of R5, apparently stabilizing the salt-bridge (**Figure 1.8**). This R5-D369-Y268 triad seems to form the core of a larger interaction network that may open to allow substrate to be released to the intracellular side and then reforms to stabilized the intracellularly-closed occluded state conformation [71].

The identification of highly conserved ion and substrate binding sites and gate structures that are formed on both sides on the binding site are suggestive of a permeation pathway that is lined on one side by TM helices 1 and 6, and on the other by TM helices 3, 8, and 10. Yamashita, *et al*., and Forrest, *et al*. [59, 72] proposed that TM helices 1 and 6 form part of a mobile domain that moves relative to 3 and 8 to open and close the extracellular and intracellular pathways. Furthermore, the unwound regions in the center of TM helices 1 and 6 may confer flexibility to the mobile domain, being a hinge region that may further allow the extracellular and intracellular halves to move independently. The intramolecular psuedosymmetry observed in the structure (discussed in Chapter 5) supports this notion. Forrest *et al*. further showed that such structural movements posited for LeuT are consistent with experimental mutagenesis and cysteine accessibility data for SERT [72].

The crystallographic accessibility of the LeuT structure has undoubtedly sharpened our knowledge of the mechanism of NSS transporters. In addition to providing an explicit structural model for the NSS family, the structure of LeuT has been used to resolve many other aspects of NSS function. For instance, by using LeuT as a structural template, the location of the Cl^- ion binding site found in SERT [73], GAT, and DAT [74] was identified. The structural basis of pharmacological inhibition has begun to be elucidated not only for LeuT itself [75-78] but also, by LeuT-based modeling, for the human transporters in numerous studies that marry experimental and computational approaches [79-90]. Furthermore, the structure has been of keen interest for studying the general biophysical principles that underlie secondary transport mechanisms, using experimental methods [75, 91-98] as well as molecular dynamics simulations [71, 72, 82, 83, 93, 95, 99-107].

Preview of this dissertation

The following chapters of this dissertation will describe the experimentation, results, and conclusions of structure-function studies for LeuT subsequent to the original work by Yamashita, *et al* [59]. In Chapter 2, we examine the substrate specificity profile of LeuT by measuring the binding, transport, and inhibition properties of a panel of putative substrates. We find that LeuT can bind and transport a range of aliphatic and aromatic L-amino acids from glycine to tyrosine, and is competitively inhibited by tryptophan, which binds but is not transported. Structural insight into the observed functional specificity is gained from crystal structures of LeuT in complex with glycine, alanine, methionine, 4-fluoro phenylalanine (an isosteric tyrosine analog), and tryptophan. These structures show that each transportable amino acid binds nearly identically to LeuT, maintaining the same α-amino and carboxylate interactions, and each complex forms the same occluded state conformation. Tryptophan also binds with the same α-amino and carboxylate interactions, but instead of forming the occluded state, the transporter is in an open-to-out conformation that is apparently "propped" open by the inability of the binding site to close up around the bulky indole sidechain of tryptophan. In this state, the R30-D404 bridge is opened and a second tryptophan molecule is observed bound between R30 and D404, suggestive of a transient binding site along a permeation pathway.

In Chapter 3, we describe a series of binding and transport assays designed to measure the stoichiometry with which substrate binds to the transporter. It was hypothesized that LeuT actually binds two leucine molecules with nanomolar affinity and act allosterically to promote transport [95], though a second leucine binding site has not been observed crystallographically. We performed isothermal titration calorimetry, equilibrium dialysis, and scintillation proximity assays to measure binding of leucine to LeuT and mutants that were proposed to knockout the second binding site. We also measured transport kinetics under different conditions to test if there is any underlying signature of a two-substrate kinetic profile. We find all data to be consistent with a single high-affinity binding site for leucine.

In Chapter 4, experiments are described in which we "engineer" LeuT to transport tryptophan based on homology to the related transporter TnaT. We find that tryptophan transport function is gained by simply a single substitution in the binding pocket: I359Q. The crystal structures of I359Q-LeuT with tryptophan show that, in contrast to wildtype, which binds tryptophan in an open state, the mutant now binds tryptophan in the same occluded state as every other transportable ligand. This lends strong evidence that the occluded state is a necessary structural intermediate in the transport cycle. Furthermore, the R30-D404 bridge is reformed in the I359Q-LeuT –tryptophan complex, with loss of the second tryptophan binding site thus demonstrating that the binding site between R30 and D404 is conformationally sensitive and that the previous observation of a second binding site (described in Chapter 2) was not an artifact of co-crystallization with tryptophan.

Chapter 5 presents a review of the principles of neurotransmitter transport, emphasizing the structural perspective from crystallographic studies. We examine two neurotransmitter transporter families, NSS and DAACS (Dicarboxylate/Amino Acid:Cation Symporter, crystallographically represented by the bacterial glutamate/aspartate transporter $\mathrm{Glt}_{\mathrm{Ph}}$ [108, 109]), describing the crystallographic and functional data from these two families. From our analysis, we suggest both a conserved general principal of transport and postulate specific mechanisms for each. Data from other transporter families that have been found to also adopt the "LeuT-fold" is synthesized to build a structural description of an alternating access mechanism for NSS and structurally related transporters.

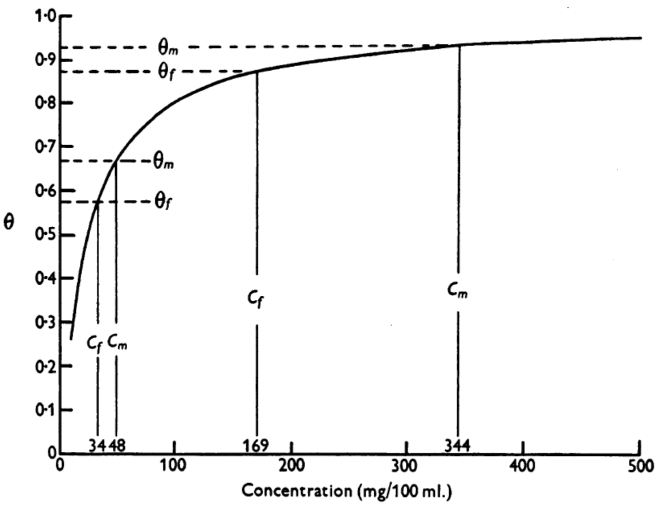

Fig. 4. Type of curve obtained from eqn. (1) relating saturation fraction (θ) to concentration. In this illustration the value of the constants of eqn. (1) have been arbitrarily fixed such that $\phi/k = 25$ mg/100 ml. to show how it would be possible for the difference in saturation of maternal and foetal carriers to be less when $C_m = 344$, $C_f = 169$ ($C_m - C_f = 175$ mg/100 ml.) than when $C_m = 48$, $C_f = 34$ ($C_m - C_f = 14$ mg/100 ml.).

Figure 1.1. Figure from Widdas, 1951 in which he illustrates the theoretical hyperbolic saturation profile of glucose transfer across sheep placenta membranes. In this paper, he relates the observed dependence of glucose uptake with Michaelis-Menten kinetics, and proposes a carrier-transfer hypothesis for glucose absorption. However, in this nascent era of transport studies, it was still assumed that the carrier was a mobile specie that physically crossed interfaces to transfer solute.

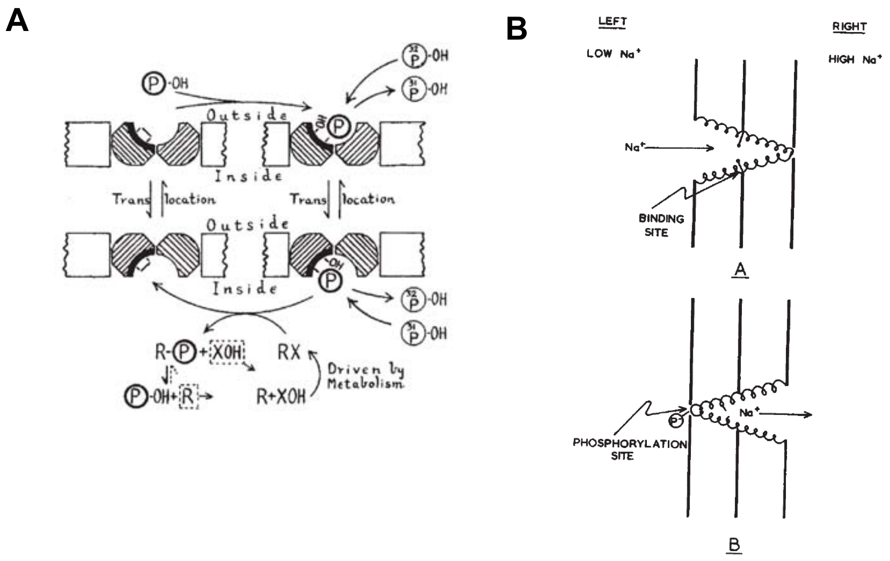

Figure 1.2. Early illustrations describing an alternating-access type mechanism for transporters. (**A**) Fig. 1 from Mitchell, 1957 describing a hypothetical carrier mechanism for the uptake of phosphate by an alternating binding site coupled to a group-transfer reaction. (**B**) Fig. 1 from Jardetzky, 1966 showing how an allosteric Na^+ pump might work via an alternating-access mechanism that is coupled to phosphorylation.

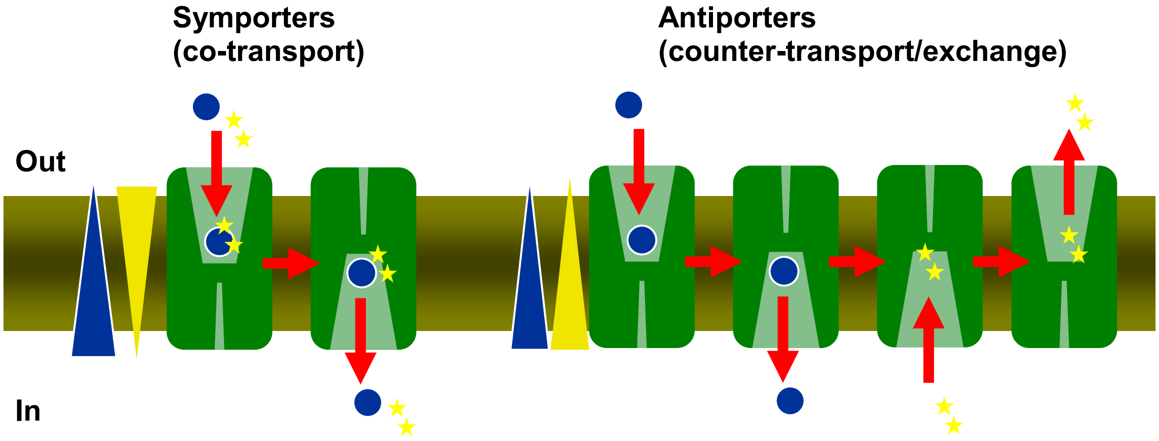

Figure 1.3. Cartoon diagram illustrating examples of ion and solute flow in symport and antiport mechanisms by secondary transporters. Blue circles and yellow stars indicate solute and ions, respectively. The blue and yellow triangles indicate the direction of the respective solute and ion gradients(thin to thick is low to high concentration). The brown shaded bar demarcates the membrane.

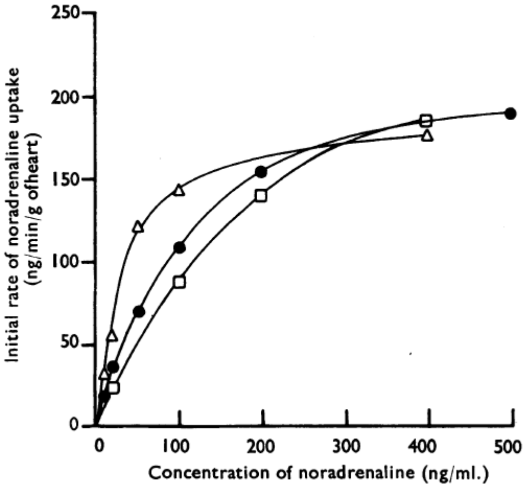

Fig. 5. Initial rates of noradrenaline uptake by the rat isolated heart perfused with various concentrations of noradrenaline. △, (−)-noradrenaline; □, (+)-noradrenaline; and ●, (±)-noradrenaline.

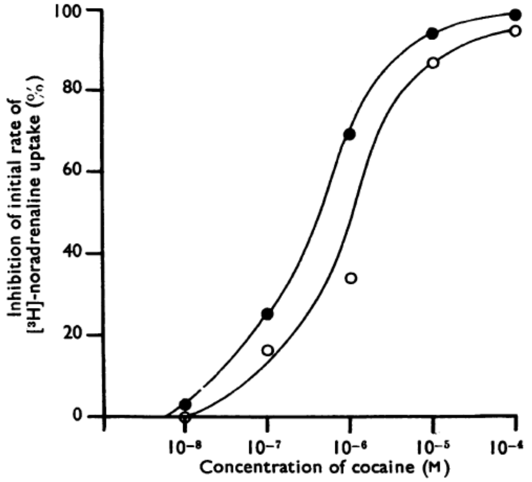

Fig. 8. Log dose/response curves for inhibition by cocaine of initial rates of uptake of [^{3}H]-noradrenaline by the rat isolated heart perfused with (±)-[^{3}H]-noradrenaline (20 ng/ml., ●; and 200 ng/ml., ○).

Figure 1.4. Figures from Iversen, 1963. The top panel shows the stereoselective saturation kinetics for noradrenaline (norepinephrine) uptake, fitted by the Michaelis-Menten function. The bottom panel shows the dose-dependent inhibition of noradrenaline uptake by cocaine.

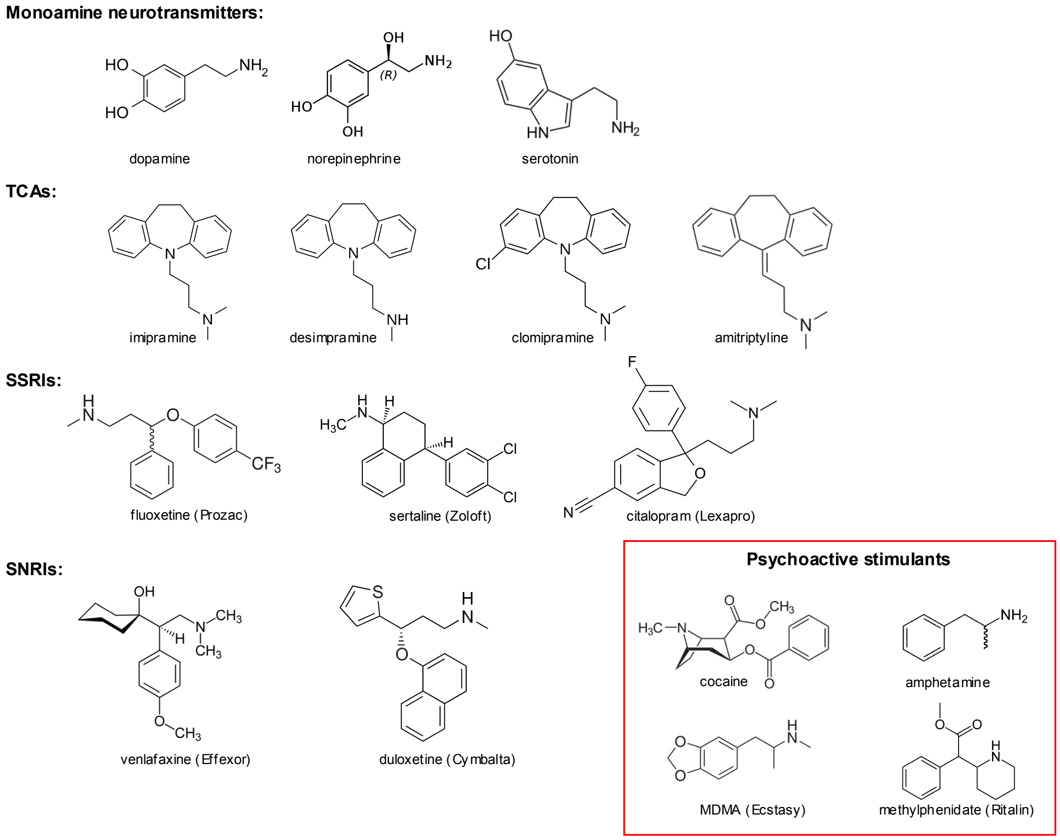

Figure 1.5. Chemical structures of monoamine neurotransmitters and a selection of drugs that target NSS transporters.

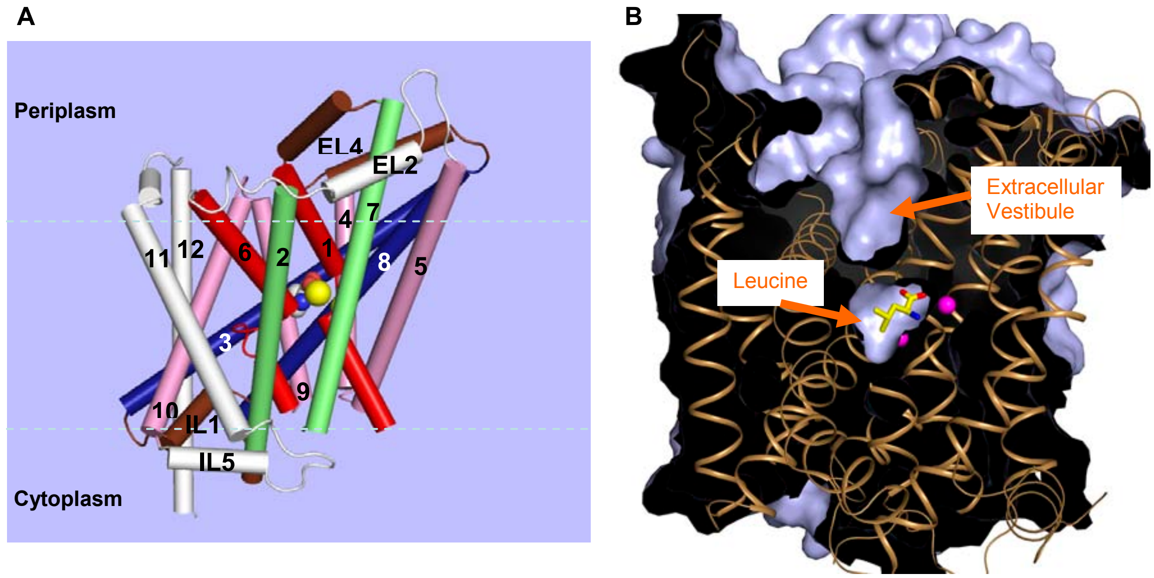

Figure 1.6. (**A**) LeuT structure. View is from the side, parallel to the membrane plane. The approximate position of the membrane relative to LeuT is indicated by dashed lines. Helices are numbered. Elements that are related by the intramolecular two-fold symmetry are similarly colored. Bound leucine and Na$^+$ are shown as spheres. (**B**) Cross-sectional slice of the LeuT structure, showing the solvent accessible surface area (blue surface), and leucine (yellow sticks) bound in an occluded binding pocket at the base of the extracellular vestibule. Na$^+$ ions are shown as magenta spheres.

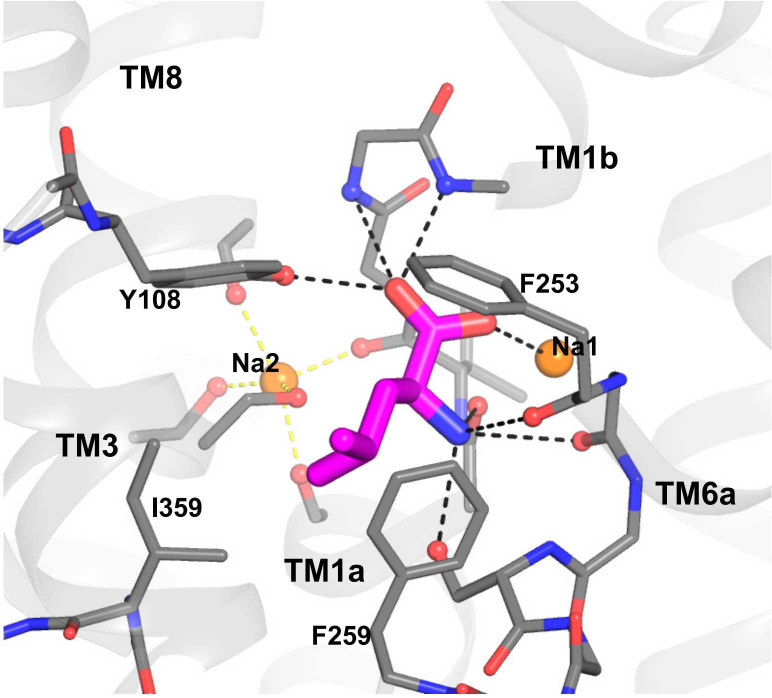

Figure 1.7. Substrate and ion binding sites in LeuT. Leucine (magenta) and Na^+ ions (orange). The α-carboxylate and amino group of leucine are bound mainly by mainchain atoms in the unwound region of TM helices 1 and 6. The carboxylate of leucine also coordinates Na1, forming a bridge between Na1 and Y108. The aliphatic sidechain of bound leucine extends across the binding site to interact with F259, I359, and Y108. Na2 is coordinated entirely by protein structure from TM helices 1 and 8.

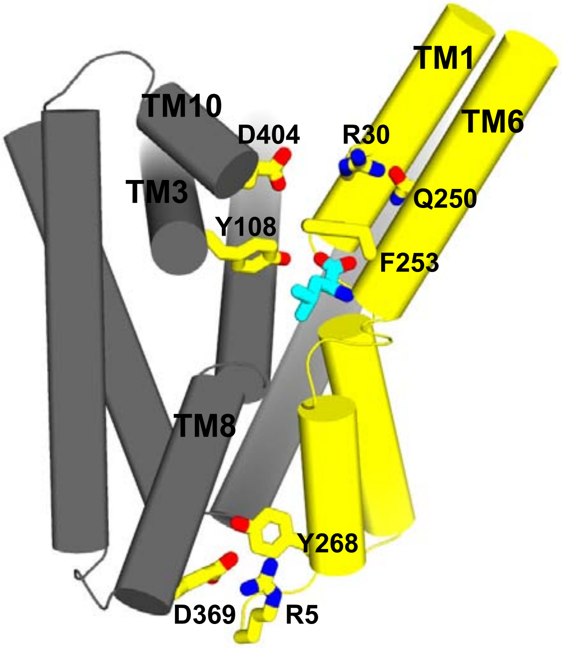

Figure 1.8. Conserved residues form extracellular and intracellular "gate" elements above and below the substrate binding site. Selected core helices of LeuT are shown, with TM helices 1 and 6 highlighted in yellow. The bound leucine molecule is shown in cyan. Conserved residues that form putative gating structures are shown as yellow sticks. TM helices 3 and 10 are truncated for clarity, Na^+ ions and water molecules are not shown.

Chapter 2

Substrate Specificity and Competitive Inhibition of LeuT

The contents of this chapter are published in modified form:

Singh, S.K., Piscitelli, C.L., Yamashita, A., Gouaux, E. (2008) A competitive inhibitor traps LeuT in an open-to-out conformation. *Science* 322(5908) 1655-1661

Author contributions: CLP and SKS conjointly performed most experiments with the following exceptions: Competition binding experiments, determination of the LeuT-methionine crystal structure, and DynDom analysis were performed by CLP; inhibition of binding and transport screens and steady-state transport measurements were performed by SKS; and the determination of the LeuT-alanine crystal structure was performed by SKS and AY. CLP, SKS, and EG analyzed all data and prepared the manuscript.

Abstract

Secondary transporters are workhorses of cellular membranes, catalyzing the movement of small molecules and ions across the bilayer, coupling substrate passage to ion gradients. However, the conformational changes that accompany substrate transport, the mechanism by which substrate moves through the transporter, and principles of competitive inhibition remain unclear. Here we use crystallographic and functional studies on LeuT, a model for neurotransmitter sodium symporters, to show that various amino acid substrates induce the same occluded conformational state, and that a competitive inhibitor, tryptophan, traps LeuT in an open-to-out conformation. In the Trp complex the extracellular gate residues, Arg30 and Asp404, define a second weak binding site for substrates as they permeate from extracellular solution to the primary substrate site, demonstrating how residues that participate in gating also mediate substrate permeation.

Introduction

Secondary active transporters are ubiquitous integral membrane proteins that couple the potential energy stored in pre-existing ion gradients to the concentrative uptake of polar and charged molecules across the lipid bilayer [110-112]. Members of the solute carrier 6 (SLC6) family of sodium-coupled transporters, also known as neurotransmitter sodium symporters (NSS), comprise one of the most widely investigated and pharmacologically important classes [113, 114]. SLC6 proteins play a central role in diverse physiological processes, ranging from the maintenance of cellular osmotic pressure [115] to the reuptake of small molecule neurotransmitters in the brain [116]. SLC6 dysfunction is implicated in numerous debilitating illnesses such as depression [117], obsessive-compulsive disorder [118], epilepsy [119], autism [120], orthostatic intolerance [121], X-linked creatine deficiency syndrome [122], and retinal degeneration [123]. Importantly, the transport activity of these molecular machines can be inhibited by many different compounds, including tricyclic antidepressants (TCAs) [124], selective-serotonergic reuptake inhibitors (SSRIs) [124], anticonvulsants [125] and cocaine [126].

Unraveling the molecular principles that define a substrate, a molecule that can be transported, versus a competitive inhibitor, a molecule that can displace the substrate but is not itself transported, is intimately linked to the larger goal of elucidating transport mechanism and ultimately to the development of new therapeutic agents. LeuT, a prokaryotic SLC6 member [59], affords an opportunity to couple functional and structural data to uncover the molecular mechanisms of transport and inhibition. Recently, a model for noncompetitive inhibition was proposed using a combination of steady-state kinetics [76], binding, and crystallographic studies with LeuT and three TCAs [76, 77]. The structures of LeuT bound to the TCA clomipramine [76], imipramine [76], or desipramine [76, 77] revealed that each of these drugs binds to LeuT in the extracellular vestibule, about 11 Å above the substrate and directly above the extracellular gating residues, R30 and D404 [76, 77], stabilizing the occluded state in a closed conformation. Zhou et al. have proposed that the TCA binding site observed in LeuT is equivalent to the TCA site in SERT and the norepinephrine transporter (NET), the therapeutic targets in humans. However, in SERT and NET, TCAs are competitive inhibitors [127-129] and their binding site likely overlaps with the substrate binding site [130]. Therefore, we suggest that the LeuT-TCA complexes do not provide a model for competitive inhibition of eukaryotic SLC6 transporters.

Here we show that LeuT is capable of transporting many hydrophobic amino acids and that a fundamental requirement for a molecule to be a substrate is that it must fit within the occluded substrate-binding cavity. Molecules such as tryptophan which can bind but are too large to be accommodated within the occluded state cavity are not substrates but instead are competitive, non-transportable inhibitors. Structural analysis of the LeuT-Trp complex reveals that tryptophan traps LeuT in an open-to-out conformation and unveils the movements that accompany transition from the occluded- to an open-to-out state. Molecular insights gleaned from our studies are especially relevant to transporter mechanism because many other transporter families, including SLC5 [25], have the same fold as LeuT and likely share mechanistic principles.

Materials and Methods

Protein expression and purification for functional experiments

LeuT protein reconstituted into lipid vesicles was expressed and purified as described previously [59]. Protein employed for both the radioligand binding and fluorescence titration experiments was purified similarly [76] except for the presence of 100 mM L-alanine during the solubilization and NiNTA chromatographic steps to displace the endogenously-bound L-leucine. The alanine concentration was subsequently decreased to 20 mM during the size-exclusion chromatographic (SEC) step in buffer I (20 mM HEPES-Tris [pH 7.0], 100 mM choline chloride) containing 1 mM n-dodecyl-β-D-maltoside [DDM] and then finally allowed to fall below 100 nM during extensive dialysis against the same buffer. All functional data were analyzed via nonlinear regression in GraphPad Prism 4.03.

Preparation of LeuT proteoliposomes

LeuT was reconstituted into lipid vesicles with a 1:110 protein:lipid ratio and loaded with buffer II (20 mM HEPES-Tris [pH 7.0], 100 mM potassium gluconate) as outlined elsewhere [76].

Inhibition of binding and transport screens

These experiments were performed at 20°C as described [76]. For binding, a typical reaction contained 100 nM LeuT, 50 nM L-[^{3}H]leucine (11.7 Ci/mmol), and 1 mM of the indicated amino acid (none for the positive control), along with 1 mM DDM, in buffer III (20 mM HEPES-Tris [pH 7.0], 100 mM NaCl). Nonspecific binding obtained in the presence of 1 mM alanine was subtracted from each data point, and binding was terminated as described [76]. For transport, a typical reaction contained 0.5 μg protein diluted 200-fold into buffer III containing 50 nM

[^{3}H]leucine (117 Ci/mmol). Nonspecific uptake into liposomes devoid of protein and subjected to the same experimental conditions was subtracted from the corresponding LeuT data points to determine specific uptake, and transport was terminated as described [76]. For both binding and transport screens, the entire experiment was performed twice, each time in triplicate, and the data normalized to that measured in the absence of competing amino acid.

Saturation binding

Binding was initiated by adding LeuT to a final concentration of 20 nM in 500 µL buffer III containing 1 mM DDM and 0.5-200 nM [^{3}H]leucine (23.4 Ci/mmol), 10-4000 nM [^{3}H]alanine (14.3 Ci/mmol), or 2-500 nM L-[^{3}H]methionine (41 Ci/mmol). Reactions were rotated at room temperature for 2 hours and then terminated as described [76] except that the filters for [^{3}H]alanine and [^{3}H]methionine were washed only once or twice, respectively. Nonspecific binding obtained in the presence of 1 mM alanine was subtracted from each data point. Experiments were performed at least three times, each time in duplicate, and the data were fit to a single-site rectangular hyperbola.

Competition binding

Binding inhibition assays were performed by equilibrating 20 nM solubilized LeuT in buffer III with 1 mM DDM and 20 nM [^{3}H]leucine (58.5 Ci/mmol) up to 15 hours at room temperature with competing cold L-amino acids at the following concentration ranges: 0-10 µM leucine, 0-100 µM methionine, 0-1 mM tyrosine, 0-1 mM L-4-F-Phe, 0-500 mM glycine, 0-10 mM alanine, and 0-10 mM tryptophan. Reactions were terminated, and the filters were washed as outlined [76]. The experiments were performed at least twice, each time in duplicate, and the data were normalized to that measured in the absence of competing amino acid and fit to a sigmoidal dose response equation. IC_{50}s were converted to K_is with the Cheng-Prusoff equation [131] using a leucine dissociation constant of 17 nM.

Steady-state kinetics

Transport was initiated at 20°C by diluting LeuT proteoliposomes (0.05 μg per assay for [^{3}H]leucine, [^{3}H]alanine, and [^{3}H]methionine or 0.5 μg per assay for [^{3}H]glycine and L-[^{3}H]tyrosine) 200-fold into buffer III containing varying concentrations of one of the five amino acids mentioned above: 0.5-800 nM [^{3}H]leucine (117 Ci/mmol), 25-5000 nM [^{3}H]alanine (17.9 Ci/mmol), 15-1600 nM [^{3}H]methionine (41 Ci/mmol), 100-30000 nM [^{3}H]glycine (14 Ci/mmol), or 100-20000 nM [^{3}H]tyrosine (20 Ci/mmol). For the lowest and highest concentrations of each amino acid, preliminary experiments established that flux remained linear for up to 10 min. Reactions were terminated after six minutes essentially as outlined [76], and each experiment was performed at least twice in triplicate, with data being fit to the Michaelis-Menten equation.

Tryptophan time course

LeuT-proteoliposomes (1.3 μg/mL in buffer III) were incubated at 20^{o}C with 1 μM [^{3}H]tryptophan (31 Ci/mmol) for up to 90 minutes. At the indicated time points, 200 μL-aliquots of the reaction mix was removed and quenched as described previously [76] For the positive control, LeuT-proteoliposomes were similarly incubated with 100 nM [^{3}H]alanine, with 200-ul aliquots removed at intervening time points up to 12 minutes. Non-specific flux was measured by repeating the time course using liposomes devoid of protein. The experiment was conducted twice in duplicate, and data were fit to a single exponential.

Binding versus transport time course

These experiments were performed as outlined for the tryptophan time course with two exceptions. First, the reaction buffer contained 70 nM [^{3}H]leucine (117 Ci/mmol), 290 nM [^{3}H]alanine (71.7 Ci/mmol), 145 nM [^{3}H]methionine (81 Ci/mmol), 955 nM [^{3}H]glycine (56 Ci/mmol), or 1415 nM [^{3}H]tyrosine (40 Ci/mmol), concentrations which are ~ 50% of the respective Michaelis constants. Second, two sets of LeuT liposomes were prepared, one loaded with buffer III to measure transport, the other loaded with buffer II to measure binding. The assay was performed twice, each time in duplicate, and the data were fit to a single exponential.

Inhibition kinetics

These experiments were conducted as delineated for [^{3}H]alanine steady-state kinetics except that a concentration range of 50-8000 nM [^{3}H]alanine (14.3 Ci/mmol) was used in the presence of three different tryptophan concentrations (0, 2, and 50 μM), and the assays were performed in the dark to minimize photooxidation of tryptophan [132]. The experiment was replicated once, each time in triplicate, and the data were fit to the Michaelis-Menten equation.

Preparation of LeuT-amino acid complex crystals

The LeuT-Ala complex was prepared as described [76]. LeuT-Met was prepared similarly except for the substitution of 10 mM methionine and 1 mM dithiothreitol (DTT) for alanine during the size exclusion chromatographic (SEC) and dialysis steps. LeuT-Leu and LeuT-SeMet were also prepared similarly except for the substitution during the SEC step of 30 mM leucine for the LeuT-Leu complex and 30 mM selenomethionine and 1 mM DTT for the LeuT-SeMet complex. LeuT-Gly was prepared with buffer containing 50 mM tryptophan during the solubilization step, 10 mM tryptophan during the NiNTA chromatographic step, and 200 mM glycine during the SEC step. LeuT-L-4-F-Phe was prepared similarly except that the pooled NiNTA fractions were applied to a series of two PD10 columns pre-equilibrated with buffer containing 20 mM TrisHCl (pH 7.0), 190 mM NaCl, 10 mM KCl, 1 mM DDM, and 8 mM D,L-4-F-Phe. Final dialysis subsequent to SEC was then performed against buffer containing 40 mM β-OG and 40 mM L-4-F-Phe. The presence of L-4-F-Phe in all samples was facilitated by monitoring a distinct, sharp absorbance peak at 262 nm that was easily distinguishable from the protein absorbance peak at 280 nm.

LeuT-Trp was prepared with the presence of 50 mM tryptophan in all buffers, and protein concentration was monitored with the Bradford assay. Some of the LeuT-Trp protein was applied to an analytical SEC column (Superose 6) to exchange the 40 mM n-octyl-β-D-glucopyranoside (β-OG) with 30 mM seleno-heptylglucoside. This would permit unambiguous placement of detergent molecules in the resulting crystal structures (see below). Selenomethionine-labeled protein (SeMet-LeuT) was expressed in C41 cells essentially as described [133] and purified as outlined for LeuT-Trp except for the addition of 1 mM β-mercaptoethanol (βME) in all buffers.

LeuT protein was concentrated to 3-6 mg/ml and subjected to crystallization trials via hanging drop vapor diffusion. Crystals for the most of the “occluded state” structures grew within 7-10 days at 20°C in the presence of 17-22% PEG 550 MME, 100 mM HEPES-NaOH (pH 7-7.5), and 200 mM NaCl. The best-diffracting crystals for the more "open" LeuT-Trp structure also grew under similar conditions except in the presence of 400 mM NaCl and in the dark. The best-diffracting crystals for the LeuT-Gly and –L-4-F-Phe complexes grew within a similar time frame and temperature except in the presence of 24-26% PEG 550 MME and 400 mM NaCl.

Structure determination

Native diffraction data were collected at 110K at NSLS beam line X29A or ALS beam line 8.2.2 at an X-ray wavelength of 1.0000 Å with the exception of data for LeuT-Ala, -Met, and -Trp crystals, which were collected at 1.1000 Å, 1.7712 Å, and 0.9796 Å, respectively. Diffraction data for all selenium-containing crystal complexes were collected at 0.9796 Å in 45° wedges (inverse beam strategy). All datasets were processed using HKL2000 [134]. Selenium sites were located with SOLVE [135] and confirmed with strong peaks ($>5\sigma$) in anomalous difference Fourier maps.

Phases for the LeuT-Gly, -Ala, Leu (30 mM), -Met, -SeMet, and –L-4-F-Phe, complexes were obtained via molecular replacement with MOLREP [136] or AMORE [137] using the LeuT-Leu structure (PDB ID 2A65) devoid of water, leucine, and sodium as the starting model. Initial phases for the LeuT-Trp complex were also calculated by molecular replacement (MOLREP) using a modified version of 2A65 in which portions of TM1, TM6, EL4a, and EL4b had been deleted. These phases were significantly improved by rigid-body refinement in REFMAC [138] and simulated annealing in CNS [139]. As independent verification of these phases, experimental phases obtained from a single-wavelength anomalous dispersion (SAD) experiment [140] on a selenomethionine-substituted LeuT-Trp cocrystal were calculated, and the SeMet-LeuT-Trp structure solved (data not shown). Refinement for all structures proceeded with iterative rounds of manual rebuilding in O [141] and COOT [142] with the assistance of sigmaA-weighted 2*F*o-*F*c and *F*o-*F*c maps as well as simulated-annealing *F*o-*F*c omit maps followed by maximum-likelihood based energy minimization and isotropic B-factor refinement in CNS [139] or REFMAC5 [138]. Ramachandran geometry is excellent for all structures, with greater than 93% of the residues in the most favored regions and none in disallowed regions. For each data set, 5% of the reflections were removed for cross-validation.

Conformational shift analysis

The conformational shifts observed between the LeuT-Trp and LeuT-Leu (PDB ID 2A65) complexes were analyzed (PDB ID 2A65) with DynDom [143]. The moving domain elements were manually assigned by first superposing the two structures using all Cα atoms in residue ranges 5-22, 55-203, 257-287, and 322-511 (RMSD = 0.41 Å). The definitions of the moving elements were subsequently modified by superposing the intervening regions of the structures and observing the RMSD fit. Two elements were identified that, when fit independently as rigid bodies, largely define the differences between the two structures. One element is composed of residues 23-54 and 241-257, which superposes with a Cα RMSD of 0.35 Å. The second element is composed of residues 304-320, which superposes with a Cα RMSD of 1.39 Å. These "moving domain" definitions were independently input into DynDom via web server access (http://fizz.cmp.uea.ac.uk/dyndom/) to calculate the degree of rotation and location of the axes.

Results and Discussion

Substrate screen of LeuT

To identify a competitive inhibitor of LeuT, we examined the ability of a spectrum of amino acids to displace [^{3}H]leucine binding from purified, detergent-solubilized LeuT and inhibit [^{3}H]leucine transport by LeuT reconstituted into lipid vesicles (**Figure 2.1A**). We found multiple aliphatic and aromatic amino acids of varying size inhibited [^{3}H]leucine binding and transport. We chose glycine, alanine, leucine, methionine, tyrosine, and tryptophan (**Table 2.1**) for further functional analysis. Competition binding of [^{3}H]leucine with unlabeled amino acids (**Figure 2.1B**; **Table 2.1**) revealed that after leucine, methionine binds the most tightly followed by alanine, tyrosine, tryptophan, and glycine. A similar trend of affinities for LeuT was observed in direct radioligand binding experiments with leucine (**Figure 2.2A**), alanine (**Figure 2.2B**), and methionine (**Figure 2.2C; Table 2.1**).

For a compound to be a competitive inhibitor, it must not only displace the substrate but cannot itself be transported. We previously demonstrated [59, 76] and replicated here that leucine and alanine are substrates (**Figure 2.3A and B**). Compared to leucine, alanine is transported with a 5-fold higher turnover rate (k_{cat}) and a 27% higher catalytic efficiency ($k_{\mathrm{cat}}/K_{\mathrm{m}}$; **Figure 2.4A and B; Table 2.1**). We show that LeuT also catalyzes the uptake of methionine, tyrosine and glycine (**Figure 2.3C-E**) with catalytic efficiencies roughly correlated to the inverse of substrate volume (**Figure 2.4C-E; Table 2.1**).

Tryptophan is not a substrate of LeuT (**Figure 2.5A**) but rather is an inhibitor. To determine the kinetic mechanism of tryptophan inhibition, we performed steady-state kinetic experiments. With [^{3}H]alanine as the substrate, increasing concentrations of tryptophan increased the Michaelis constant (K_m) of LeuT for [^{3}H]alanine without changing the maximum velocity (V_{max}) (**Figure 2.5B; Table 2.1**). The corresponding Eadie-Hofstee plot (**Figure 2.5C**) exhibited nonparallel lines intersecting on the y-axis, hallmarks of competitive inhibition.

LeuT-substrate crystal structures reveal an occluded state

To probe the atomic basis of ligand specificity, we cocrystallized LeuT with each of the six amino acids, measured x-ray diffraction data to high resolution, and solved the structures by molecular replacement. The readily-soluble, isosteric tyrosine analog, L-4-fluorophenylalanine (4-F-Phe), was used in place of tyrosine because tyrosine's low solubility limit precluded successful cocrystallization. All cocrystals diffracted to 1.8–2.3 Å resolution (**Table 2.2**) and the resulting structures refined well (**Table 2.3**).

The structures of LeuT in complex with each of the substrates (glycine, alanine, leucine, methionine, 4-F-Phe) are similar, with overall Cα RMSDs ranging from 0.2 to 0.3 Å (**Figure 2.1C**) despite the 132 Å^3 variation in substrate volume. All five structures adopt the same outward facing occluded state as originally seen in the LeuT-Leu complex in which access to the substrate binding pocket from both the extracellular and cytoplasmic sides of the membrane is obstructed, with access from the extracellular side being blocked by just a few residues and access from the intracellular side being blocked by ~25 Å of tightly packed protein [59, 76] (**Figure**

2.1D-E). Simulated-annealing F_o-F_c omit maps (**Figure 2.6A-D**) confirm the position of the substrates in the occluded binding pocket located in the center of the transporter, halfway across the lipid bilayer. Residues F253 and Y108 reside on "top" of the substrate, with electrostatic interactions formed by D404 and R30 layered directly above F253 and Y108. The hydroxyl of Y108 retains its two critical hydrogen bonds: one with the substrate carboxylate that helps anchor the substrate in place and the second with the amide nitrogen of L25 that stabilizes the unwound region of TM1 and bridges TM1 with TM3 (**Figure 2.1E; Figure 2.7A-E**).

Despite overall congruence among the structures, there are differences in comparison to the Leu complex, localized primarily to F259 and I359. For the glycine and alanine complexes, the "R" groups of these ligands induce a ~30° torsion of F259's phenyl ring and ~15° torsion of I359's *sec*-butyl moiety into the substrate binding cavity, compensating for the poor fit of the substrate to the binding pocket (**Figure 2.1E, Figure 2.7A and B**) and consistent with the weak affinity of LeuT for these two amino acids. The LeuT-Met and –Leu complexes superimpose within experimental error (**Figure 2.1E, Figure 2.7C and D**), a finding in accord with their similar binding and transport parameters. Substituents larger than those of leucine or methionine begin to sterically hinder binding and formation of the occluded state. The structure of the 4-F-Phe complex exhibits the most pronounced differences: a ~180° rotation of I359's *sec*-butyl group as well as a ~0.5 Å outward shift in the backbone of the unwound region in TM6 (G258-A261) (**Figure 2.1E; Figure 2.7E**). The displacement of the backbone is suggestive of a strained occluded state, perhaps one that is less likely to isomerize to the open-to-in state. While speculative, this hypothesis is consistent with tyrosine's reduced turnover rate.

LeuT-Trp complex adopts an open-to-out conformation

What are the structural principles by which tryptophan acts as a competitive inhibitor of LeuT? The LeuT-Trp complex exhibits an open-to-out conformation characterized by a widening of the extracellular vestibule and solvent accessibility to the substrate binding pocket (**Figure 2.8A and B**). Relative to the occluded state, in the LeuT-Trp complex there is a 9° outward rotation of a structural element comprised of TMs 1b (residues 23-38), 2a (40-54), and 6a (241-257) about an axis oriented nearly parallel to the membrane and located near the unwound regions of TMs 1 and 6 (**Figure 2.8C; Movie 2.1**). To accommodate movement of these helices, the highly conserved glycine-rich loop between TMs 1b and 2a slides under EL3 (233-240), the latter of which also undergoes a concerted translation along its helical axis, approximately parallel to the membrane. The EL4a helix (307-318) also undergoes an outward rotation of nearly 13° about an axis running approximately perpendicular to the plane formed by the EL4 loop (**Figure 2.8C; Movie 2.1**). Together, these movements widen the extracellular vestibule at the base by 3 Å, as defined by measurements between residues Y108 and F253 (**Figure 2.8A, B, and E**).

TM11 also undergoes a substantial displacement in the LeuT-Trp complex. Concomitant with the outward rotation of neighboring TM6a, TM11 shifts inward by ~2 Å in the region around W467, while the indole side-chain of W467 on the interior face of the helix rotates 90° about $\chi 2$ relative to that in the occluded state structures. The space vacated by rotation of this indole ring and the outward movement of TM6a is partly occupied by the alkyl chain of a β-octylglucoside molecule (**Figure 2.9**).

Like substrates, the amino group of Trp601 forms hydrogen bonds with oxygen atoms in TMs 1b and 6a (**Figure 2.7F; Figure 2.8D**). Similar coordination exists between the carboxylate of Trp601 and the backbone amide nitrogens of TM1b (L25 and G26) as well as Na1 (**Figure 2.7F; Figure 2.8D**); Na2 is also present in the Trp complex and is coordinated in a similar manner as the occluded state complexes. The indole ring is accommodated in the binding pocket and, with only minor adjustments to the sidechain geometry of I359 and a slight rotation of Y108, engages in nonpolar interactions with these residues (**Figure 2.8E**). Furthermore, the indole ring nitrogen of Trp601 is within ~3.2 Å of the phenyl ring face of F259, forming an edge-to-face aromatic interaction (**Figure 2.7F; Figure 2.8D**).

Unlike the substrate-bound complexes, the LeuT-Trp structure reveals significant differences that define the molecular basis of competitive inhibition. The α-amino and α-carboxylate substituents of Trp601 are shifted by ~2 Å relative to the corresponding positions of these atoms in the substrate-bound, occluded-state complexes (**Figure 2.8E**). Trp601's rigid indole ring acts like a strut that braces the binding pocket open, with the α-amino and carboxylate groups maintaining their conserved interactions with TMs 1 and 6 (**Figure 2.8D**) and the distal edge of the indole ring lodged against TMs 3 and 8. This mode of binding prevents the extracellular vestibule from closing and adopting the occluded state (**Figure 2.8A and B**). Specifically, the hydrogen bond observed in the occluded state between the substrate and Y108 hydroxyl does not form with Trp601 (**Figure 2.7F; Figure 2.8D-E**), and the extracellular gate residue F253 on TM6a is ~3.0 Å farther away from Y108, resulting in a solvent-accessible channel to the binding pocket (**Figure 2.8B**).

Second ligand binding site is unique to the open-to-out conformation

Electron density maps revealed unanticipated density for a second Trp molecule (Trp602) at the base of the extracellular vestibule. Trp602 contacts TM10 and its α-substituents form an ionic bridge between residues D404 and R30 of the extracellular gate (**Figure 2.10A**). The amino group also makes a hydrogen bond with the side chain hydroxyl of T409, while the indole nitrogen hydrogen bonds with the carbonyl oxygen of G408, located in a stretch of π-helix between M403 and V412 (**Figure 2.10A**).

We suggest that Trp602, located ~4 Å above Trp601, represents a low affinity, transiently occupied site for amino acids as they move from the extracellular vestibule to the substrate binding pocket, perhaps with R30 and D404 serving to dehydrate the incoming amino acid. Although molecular dynamics studies [95, 106] and binding assays [95] suggest that the substrate leucine can bind to a site similar to the Trp602 site when LeuT is in an occluded-like state, the LeuT-Trp crystal structure demonstrates that occupancy of the Trp602 site requires an open-to-out state, with the guanidinium group of R30 and the side chain carboxylate of D404 separated by ~7-8 Å. To determine if substrates can bind to the Trp602 site in the occluded state, we solved the crystal structure of LeuT with 30 mM leucine and did not observe any amino acid density in the extracellular vestibule (**Figure 2.11**).

We also measured diffraction data on a LeuT-selenomethionine complex. Anomalous difference Fourier maps show a large anomalous peak (25σ) in the primary binding site but no significant peaks elsewhere (**Figure 2.10B**).

In addition to Trp601 and 602, we observed two additional tryptophans (603 and 604) at the cytoplasmic and extracellular faces of LeuT, respectively (**Figure 2.8C**). Trp603 is located in the cleft between EL2 and EL4, while Trp604 is situated at the cytoplasmic-face of LeuT and forms a salt bridge with R11. At present we believe these tryptophan molecules are not relevant to the function of LeuT, in large part because they are removed from mechanistically crucial regions of the transporter.

A model for transport and inhibition

How do inhibitors prevent substrate translocation? For LeuT we postulate that inhibition of transport occurs by preventing distinct steps of the transport cycle (**Figure 2.12D and E**). Here we show that a competitive inhibitor displaces substrate and traps the transporter in an open-to-out conformation, thereby preventing progression to the occluded state (**Figure 2.12A and D**). The LeuT-Trp complex demonstrates how the extracellular-facing TMs 1b, 2a (residues 40-54), and 6a are involved in the binding of a competitive inhibitor and in the ensuing conformational changes, showing that TMs 1b, 2a and 6a move independently of their respective intracellular-facing counterparts, TMs 1a, 2b (residues 55-70), and 6b and that the TM1, 2, 6 and 7 helix bundle does not move as rigid body, in contrast to a recent proposal by Forrest and colleagues [72]. The notion that TMs 1b and 6a undergo conformational changes upon substrate or inhibitor binding is further supported by chemical modification experiments on single cysteine mutants of the eukaryotic GABA and serotonin transporters [144-146].

What are the molecular principles associated with binding, i.e. formation of the occluded state? We suggest that substrates permeate from extracellular solution to the primary substrate site, located halfway across the membrane, by transiently binding to the extracellular gate residues R30 and D404. We argue that this binding event is only possible when the transporter is in the open-to-out conformation, typified by the LeuT-Trp complex. The substrate then moves to the primary binding site and the open-to-out state 'collapses' to the occluded state (**Figure 2.12A and B**) before isomerizing to the open-to-in state and permitting release of substrate to the cytoplasm (**Figure 2.12B and C**) . The transporter can then cycle to the open-to-out state, perhaps through an apo yet occluded-like conformation. Optimal substrate binding and formation of the occluded state requires complementary shape and charge and is best satisfied by leucine and methionine. The apparent paradox posed by these two amino acids, which exhibit the highest binding affinities but the lowest turnover rates and catalytic efficiencies, is reconciled by the notion that transport is a balance between affinities for different intermediates in the transport cycle. Accordingly, the slow turnover rates of leucine and methionine are due to the fact that their occluded state complexes are very stable and the energy barriers associated with isomerization to open-to-in (**Figure 2.12B and C**) or -out conformations are relatively high. By contrast, the reduced affinity but higher turnover rate and catalytic efficiency of the smaller alanine is likely a reflection of the limited degree to which it can stabilize the occluded state compared to leucine or methionine.

The distinction between a substrate and a competitive inhibitor is provided by the ability of the ligand to promote formation of the occluded state. For LeuT, this distinction is highlighted by the differences between tyrosine and tryptophan. Because tyrosine is a substrate and tryptophan is not, there is an apparent size "boundary" for transport between 197 and 228 Å^3, the volumes of tyrosine and tryptophan, respectively. In GAT1, the existence of a size boundary between transport and inhibition has been shown, where the addition of an aromatic moiety transforms the substrate nipecotic acid into the non-transportable competitive inhibitor SKF89976A [147]. In the SLC5 family, this size boundary has also been demonstrated with a series of glycoside derivatives in experiments on the human glucose transporter (hSGLT1) [147]. Whereas galactose is a substrate, 1-naphtylgalactose is a non-transportable, competitive inhibitor. But the boundary between a substrate and competitive inhibitor does not solely reside with the ligand. More generally, the definition of this boundary depends on the size, shape, and rigidity of the ligand relative to the constraints imposed by the binding pocket. Thus, amino acid substitutions in the binding pocket that alter these constraints, i.e. increase volume, should also alter this boundary. An example of this second case is TnaT, a prokaryotic SLC6 tryptophan transporter [56]. Comparison of the amino acids lining the substrate-binding pocket in LeuT and TnaT [69] reveals that a prominent difference is substitution of the larger Phe at position 259 of LeuT with the smaller Val in TnaT. These substitutions would increase the volume of the binding pocket in TnaT to permit accommodation of Trp in an occluded state. These molecular principles are not only relevant to our understanding of LeuT and its SLC6-orthologs but are also germane to the structurally related glucose and nucleobase transporters [25, 148].

Table 2.1. Binding and kinetic constants. Unless otherwise noted, the errors represent the s.e.m. from two or three independent experiments, each performed in duplicate or triplicate. n.d., not determined.

Binding & Displacement Constants

L-amino acid (Å^3)*	K_d (nM)†	B_{max} (pmol)‡	K_i (nM)§
Gly (65)	n.d.	n.d.	322,000 ± 36,900
Ala (90)	512 ± 131	1.1 ± 0.5	3320 ± 810
Leu (164)	20 ± 2	0.6 ± 0.1	16 ± 1
Met (167)	69 ± 8	0.8 ± 0.04	232 ± 21
Tyr (197)	n.d.	n.d.	9040 ± 550
L-4-F-Phe	n.d.	n.d.	950 ± 100
Trp (228)	n.d.	n.d.	64800 ± 4670

Steady-State Kinetics

L-amino acid (Å^3)*	K_m (nM)	V_{max} (pmol/min/mg)	k_{cat} (hr^{-1})	k_{cat}/K_m ($nM^{-1}hr^{-1}$)
Gly (65)	1910 ± 30	444 ± 57	1.58 ± 0.20	0.0008
Ala (90)	583 ± 28	1730 ± 94	6.06 ± 0.30	0.0104
Leu (164)	146 ± 25	343 ± 46	1.20 ± 0.20	0.0082
Met (167)	289 ± 27	523 ± 12	1.86 ± 0.04	0.0064
Tyr (197)	2830 ± 150	209 ± 15	0.74 ± 0.05	0.0003
Trp (228)		not transported		

Competitive Inhibition of L-alanine Transport by L-tryptophan

[Trp] μM	K_m (nM)	V_{max} (pmol/min/mg)	K_i (μM)◊
0	665 ± 78	1530 ± 50	
20	1020 ± 230	1550 ± 110	24 ± 3
50	1880 ± 330	1610 ± 110	

*Volume in Å^3 of amino acid as defined in (*38*). K_d is dissociation constant. ‡B_{max} is number of binding sites. §K_i refers to inhibition of [^{3}H]Leu binding. ◊K_i refers to inhibition of [^{3}H] Ala transport.

Table 2.2. LeuT Substrate/Inhibitor Data Collection Statistics

	Glycine	**Alanine**	**Leucine**[a]	**Methionine**	**SelenoMet**	**L-4-F-Phe**[b]	**Tryptophan**
Beamline	ALS 8.2.2	NSLS X29A	ALS 8.2.2	ALS 8.2.2	ALS 8.2.2	ALS 8.2.2	ALS 8.2.2
Wavelength (Å)	1.0000	1.1000	1.0000	1.7712	0.9794	1.0000	0.9796
Space Group	C2	C2	C2	C2	C2	C2	C2
Cell Dimensions							
a, b, c (Å)	90.1, 86.6, 81.5	89.4, 87.2, 81.2	89.4, 86.7, 81.4	88.3, 86.6, 81.2	89.8, 86.7, 81.7	90.1, 86.3, 81.6	88.6, 85.2, 82.3
α, β, γ (°)	90.0, 95.3, 90.0	90.0, 95.9, 90.0	90.0, 95.9, 90.0	90.0, 95.6, 90.0	90.0, 95.9, 90.0	90.0, 95.2, 90.0	90.0, 93.3, 90.0
Resolution (Å)	50.00-2.15	50.00 - 1.90	80.85-1.80	47.51-2.30	81.38-1.95	62.3-2.10	50.00-2.00
R_{merge} (%)[c, d]	7.7 (76.3)	6.3 (52.2)	5.0 (75.0)	8.0 (32.1)	7.0 (76.8)	7.8 (52.7)	8.4 (73.4)
$I/\sigma I$ [c]	30.0 (1.9)	39.2 (2.4)	34.7 (2.7)	22.2 (1.6)	28.0 (2.6)	15.9 (1.7)	11.1 (1.1)
Completeness (%)[c]	98.6 (90.3)	99.9 (99.9)	99.0 (98.1)	87.7 (53.4)	99.5 (98.2)	92.3 (64.3)	97.4 (90.4)
Redundancy[c]	6.7 (5.4)	4.6 (2.8)	7.3 (6.8)	6.3 (2.5)	7.4 (6.7)	3.5 (2.6)	2.6 (2.3)

[a] Structure determined in the presence of 30 mM Leu.

[b] Abbreviation for the tyrosine analogue, L-4-fluorophenylalanine.

[c] Number in parentheses represents statistics for data in the highest resolution shell, 2.23-2.15 Å, 1.97-1.90 Å, 1.86-1.80 Å, 2.38-2.30 Å, 2.02-1.95 Å, 2.18-2.10 Å, and 2.07-2.00 Å for the LeuT-Gly, -Ala, -Leu, -Met, -SeMet, -L-4-F-Phe, and -Trp, data sets, respectively.

[d] $R_{\text{merge}} = \sum_{hkl}\sum_i |I_i(hkl)_i - <I(hkl)>| / \sum_{hkl}\sum_i I_i(hkl)$.

Table 2.3. LeuT Substrate/Inhibitor Refinement Statistics

	Glycine	Alanine	Leucine[a]	Methionine	SelenoMet	L-4-F-Phe[b]	Tryptophan
Resolution (Å)	50.00-2.15	50.00 - 1.90	50.00-1.80	50.0-2.30	50.00-1.95	62.30-2.10	50.00-2.00
No. reflections	33,833	48,834	57,474	26,640	45,397	31,935	41,152
R_{work}[c]/R_{free}[d] (%)	19.6/22.8	21.1/22.9	18.0/20.5	19.7/22.4	19.2/21.8	19.6/23.7	19.8 /23.0
No. atoms	4190	4298	4343	4211	4116	4280	4327
Protein [e]	4045	4074	4045	4045	4268	4077	4010
Substrate/Inhibitor	10	6	9	9	9	13	60
Na^+	2	2	2	2	2	2	2
β-OG	60	120	134	100	60	100	160
Water	73	96	153	55	112	88	95
B-factors ($Å^2$)							
Overall	50.6	41.3	37.5	47.2	39.4	40.2	42.0
Protein	49.6	40.1	36.2	47.4	39.0	39.4	38.1
Substrate/Inhibitor	38.0	26.6	22.1	38.6	26.8	29.6	26.8
Inhibitor 2	n/a [f]	n/a [f]	n/a [f]	n/a [f]	n/a [f]	n/a [f]	55.7 [g]
Na^+	38.0	27.1	22.6	33.6	24.9	27.6	11.9
β-OG	87.5	79.5	67.7	86.2	55.4	74.8	67.2
Water	53.5	47.3	46.3	50.7	46.3	40.6	39.3
RMSD [h]							
Bond lengths (Å)	0.006	0.006	0.011	0.007	0.003	0.006	0.008
Bond angles (°)	0.889	1.095	1.244	0.970	0.729	0.989	1.050
Ramachandran Plot [i]	93.6, 6.2, 0.2, 0.0	94.1, 5.7, 0.2, 0.0	94.7, 5.3, 0.0, 0.0	95.0, 5.0, 0.0, 0.0	94.5, 5.5, 0.0, 0.0	94.7, 5.3, 0.0, 0.0	93.3, 6.7, 0.0, 0.0

[a] Structure determined in the presence of 30 mM Leu.

[b] Abbreviation for the tyrosine analogue, L-4-fluorophenylalanine.

[c] $R_{work} = \sum||F_o| - |F_c||/\sum|F_o|$, where F_o and F_c are the observed and calculated structure factor amplitudes, respectively.

[d] R_{free} is the R-value for r a 5% subset of reflections excluded from refinement.

[e] Number includes protein atoms with alternate conformations.

[f] n/a, not applicable

[g] Average value for the three Trps bound outside of the substrate binding pocket (Trp602, Trp603, and Trp604)

[h] RMSD, root mean square deviation.

[i] Percentage of amino acids in the most favored, allowed, generous, and disallowed regions of the Ramachandran plot, respectively.

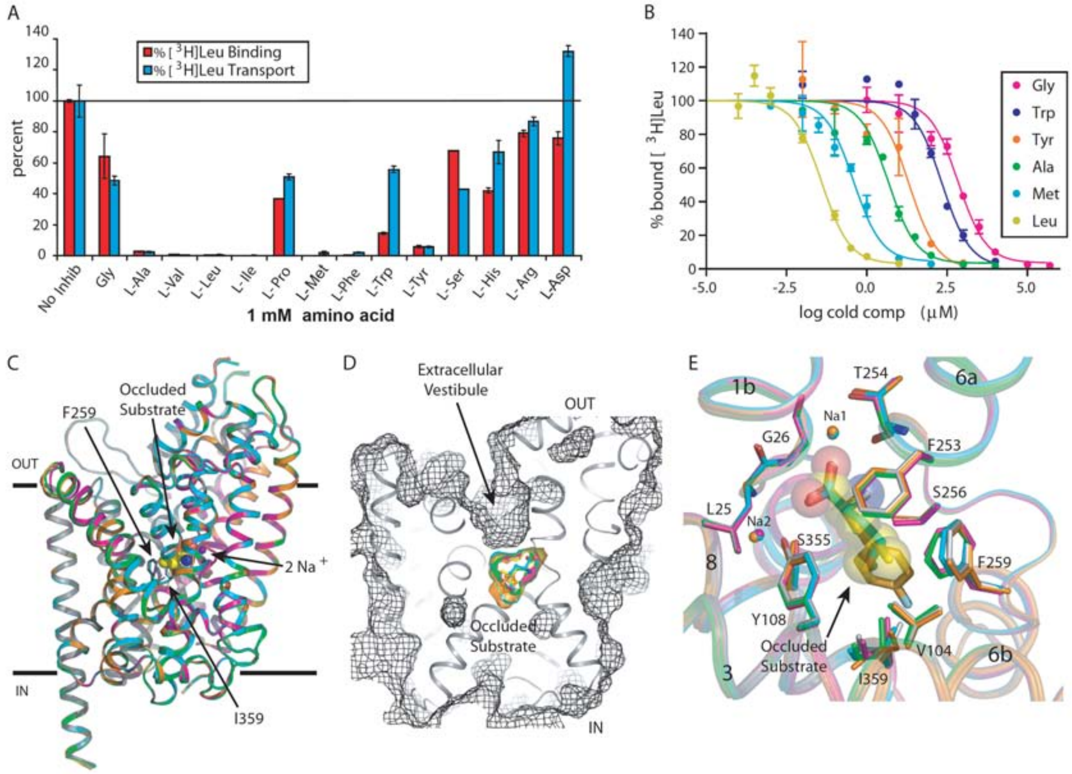

Figure 2.1. LeuT substrate screen and occluded state structures. (**A**) Inhibition of [^{3}H]leucine binding (red bars) and transport (cyan bars) by L-amino acids. (**B**) Displacement of [^{3}H]leucine binding by leucine (yellow), methionine (cyan), alanine (green), tyrosine (orange), tryptophan (blue), and glycine (magenta). Errors bars represent s.e.m. of triplicate (A) or duplicate (B) measurements. (**C**) Superposition of the LeuT-Leu (gray), -Ala (green), -Gly (magenta), -Met (cyan), and L-4-F-Phe (orange) complexes using α-carbon positions. Shown in CPK are leucine and the two Na$^+$ ions from the LeuT-Leu complex. Membrane boundaries are demarcated by the two solid black lines. (**D**) Solvent-accessible surface (depicted in mesh) illustrating the occluded state of the LeuT-substrate complexes. (**E**) Close-up of the substrate binding pocket, with substrates depicted as sticks. Leucine is shown in semi-transparent CPK representation. Coloring is the same as in (C).

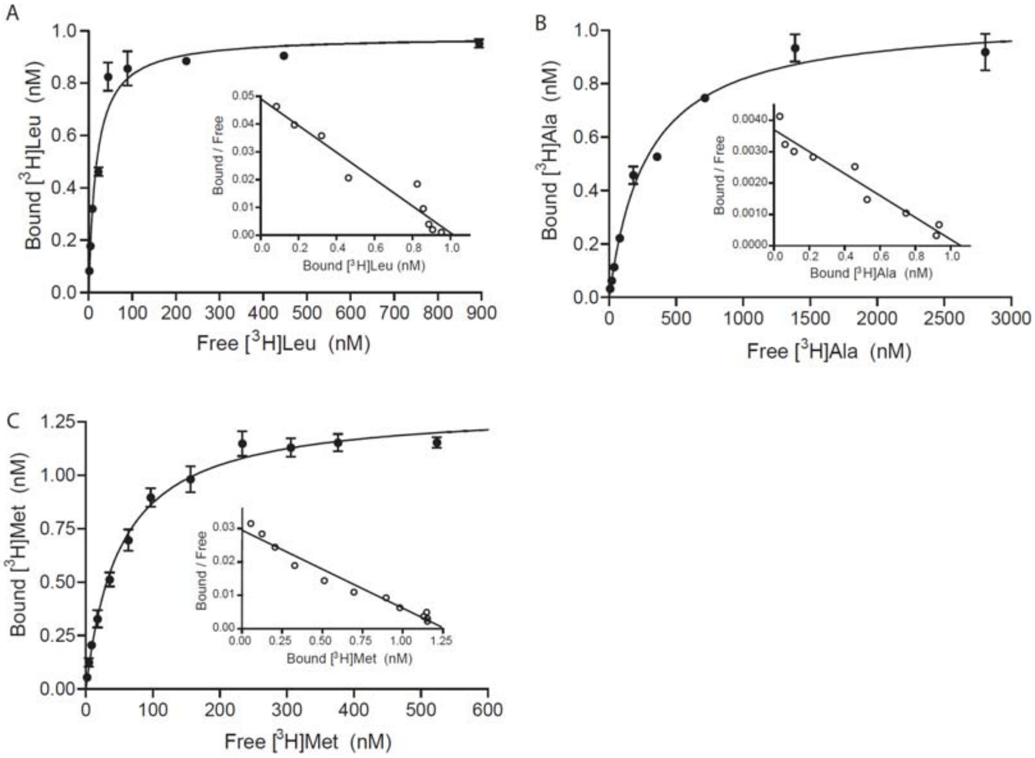

Figure 2.2. Radioligand binding data. Saturation binding plots for (**A**) [^{3}H]leucine, (**B**) [^{3}H]alanine, and (**C**) [^{3}H]methionine with Scatchard insets. Data are shown as mean +/- s.e.m. (vertical bars, *N* = 3).

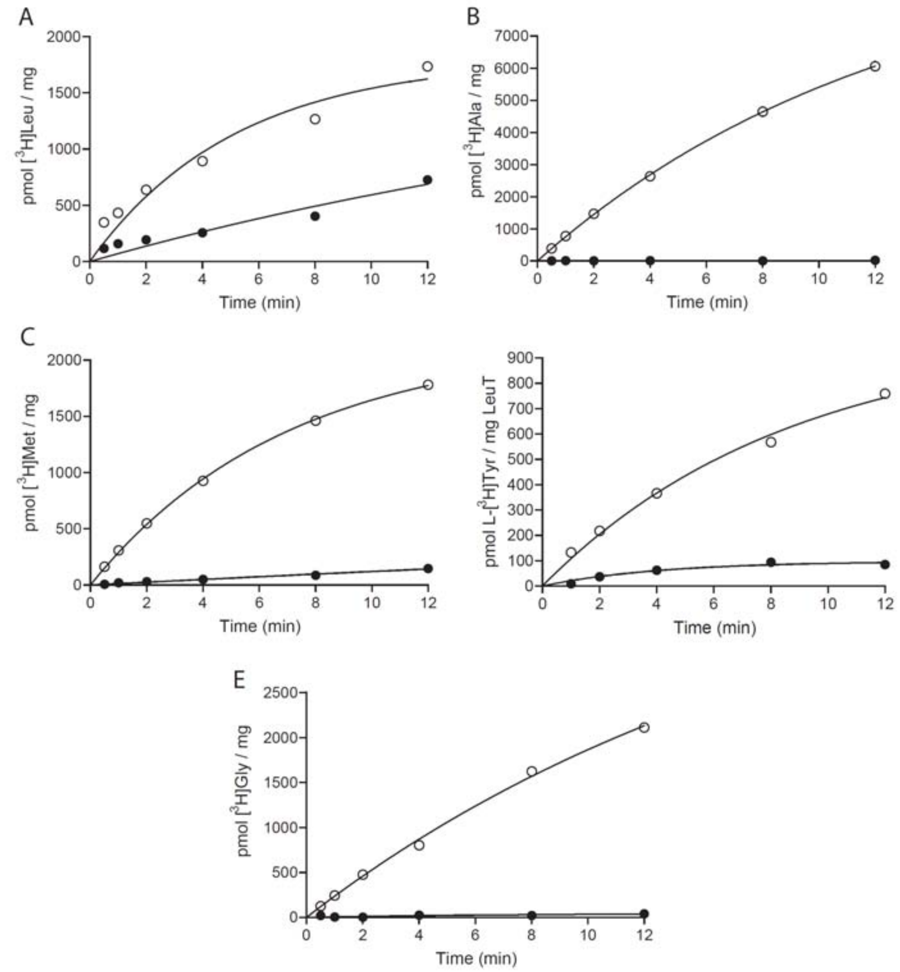

Figure 2.3. Transport versus binding control experiments for the five amino acid substrates examined. Transport by (open circles) and binding to (filled circles) for (**A**) [^{3}H]leucine, (**B**) [^{3}H]alanine, (**C**) [^{3}H]methionine, (**D**) [^{3}H]tyrosine, and (**E**) [^{3}H]glycine. Data shown are mean values (*N* = 2).

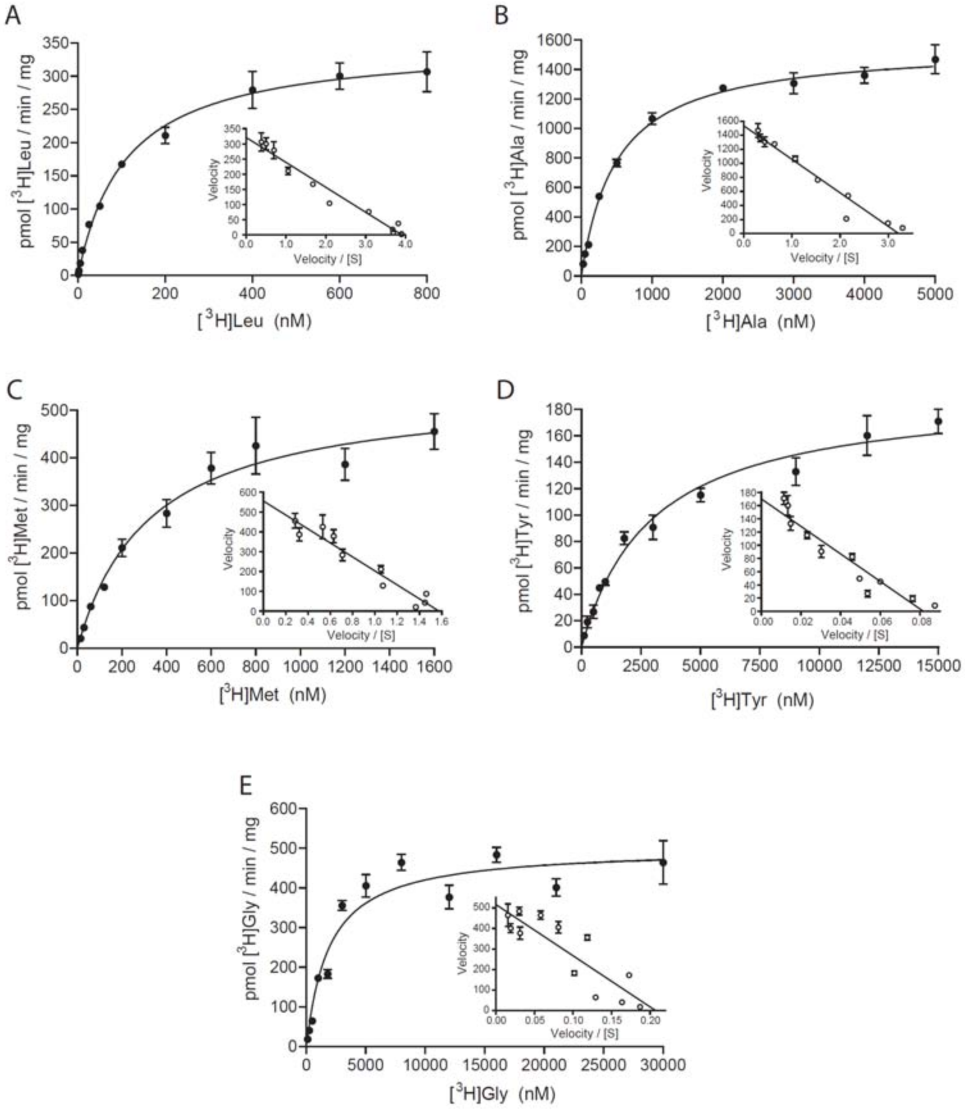

Figure 2.4. Steady-state kinetics. Michaelis-Menten plots for (**A**) [^{3}H]leucine, (**B**) [^{3}H]alanine, (**C**) [^{3}H]methionine, (**D**) [^{3}H]tyrosine, and (**E**) [^{3}H]glycine with Eadie-Hofstee insets. Data shown are mean +/- s.e.m. (vertical bars, *N* = 3).

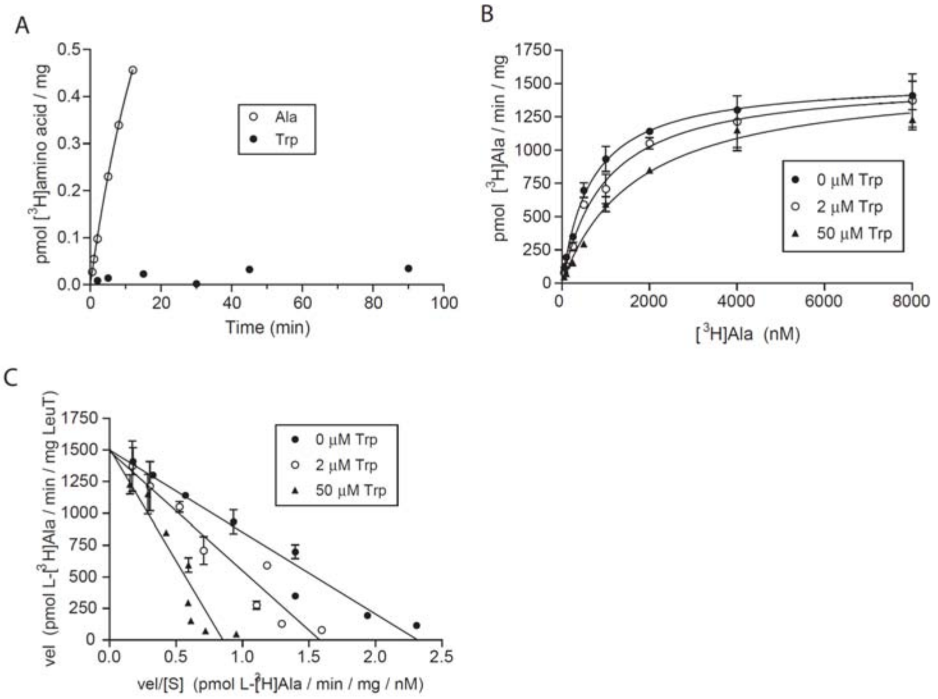

Figure 2.5. L-tryptophan is a nontransportable, competitive inhibitor of LeuT. (**A**) Time course of 100 nM [^{3}H]alanine (open circles) versus 1 μM [^{3}H]tryptophan transport demonstrating that tryptophan is not a substrate. (**B**) Steady-state kinetics (Michaelis-Menten plot) of inhibition of [^{3}H]alanine transport by 1, 2, and 50 μM tryptophan. (**C**) Eadie-Hofstee plot of the same data shown in (B). Data are shown as mean values in A (*N* = 2) or mean +/- s.e.m. (vertical bars, *N* = 3) in B and C.

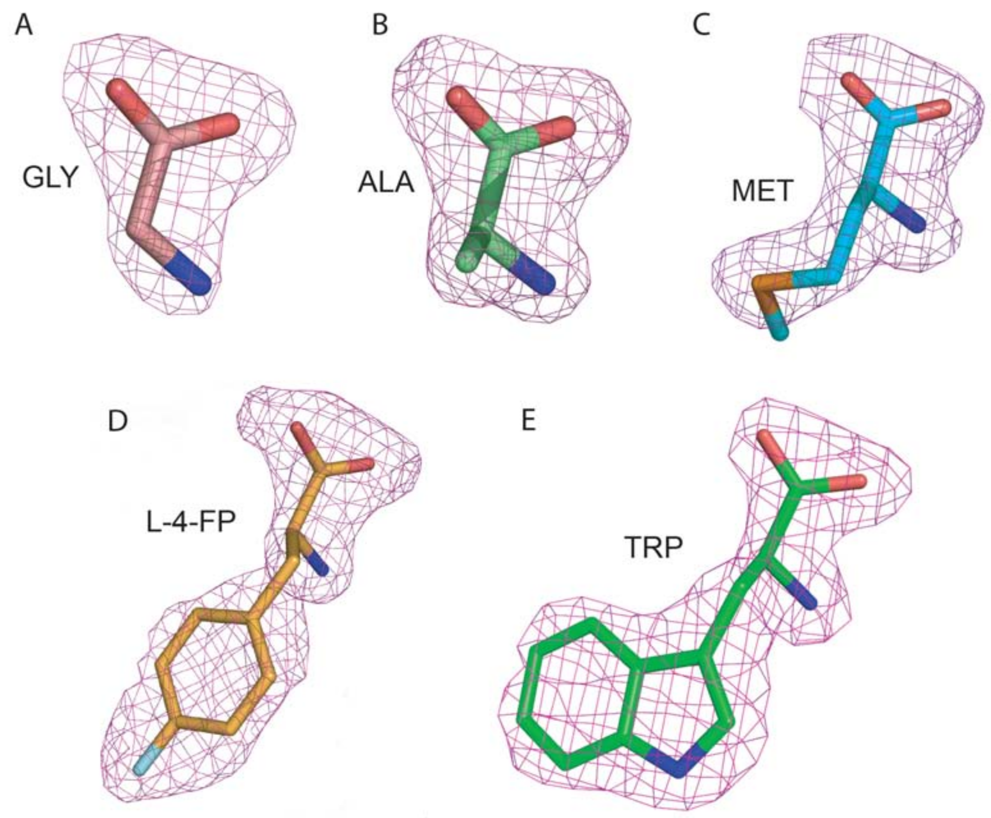

Figure 2.6. Simulated-annealing omit electron density maps (contoured at 3σ) of amino acids bound in the substrate binding pocket of LeuT (the "601" site). (**A**) Glycine, (**B**) alanine, (**C**) methionine, (**D**) L-4-fluorophenylalanine, and (**E**) tryptophan. In each case, the respective amino acid was omitted from the simulated annealing run and subsequent phase calculation.

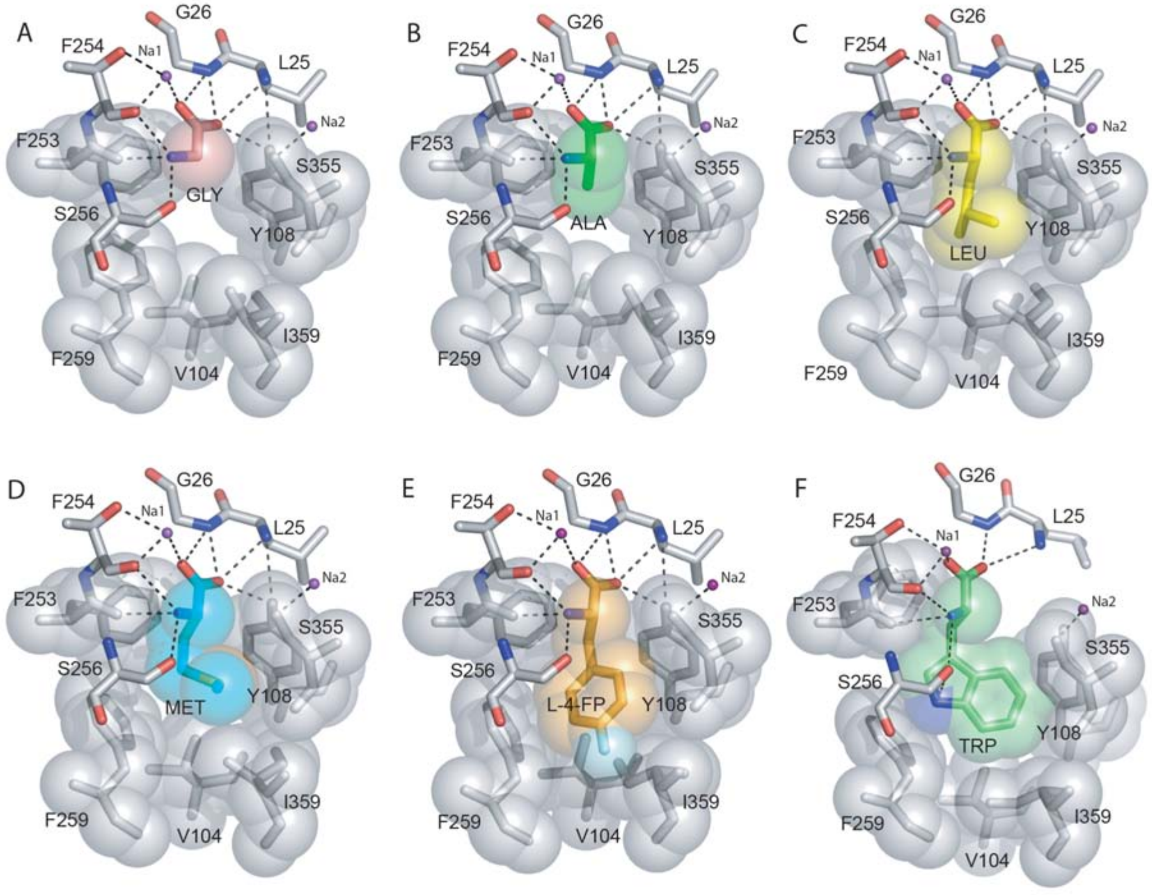

Figure 2.7. Substrate binding pocket - substrate and inhibitor interactions. Substrate binding pockets of the (**A**) LeuT-Gly, (**B**) -Ala, (**C**) -Leu,(**D**) -Met, (**E**) -L-4-F-Phe, and (**F**) -Trp complexes. Hydrogen bonds and polar interactions are illustrated by black dotted lines.

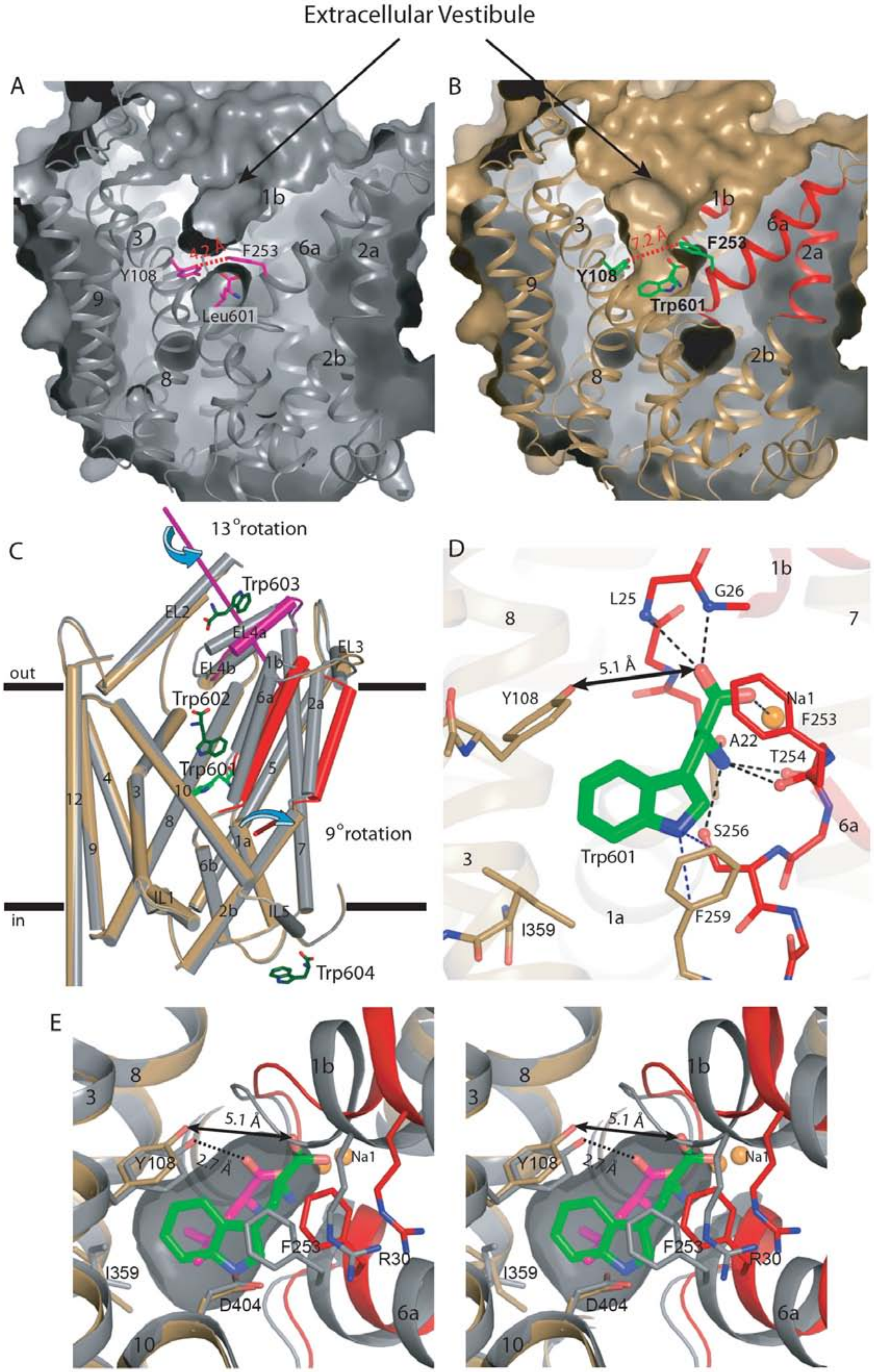
Extracellular Vestibule
A
1b
3
4.2 Å
F253
6a
2a
Y108
9
Leu601
8
2b
B
1b
3
7.2 Å
F253
6a
2a
Y108
9
Trp601
8
2b
C
13°rotation
Trp603
EL2
EL4a
out
EL4b
1b
EL3
Trp602
6a
2a
Trp601
5
12
4
3
10
8
9
1a
9°rotation
7
6b
in
IL1
2b
IL5
Trp604
D
L25
G26
1b
8
7
5.1 Å
Y108
Na1
F253
A22
T254
Trp601
S256
6a
3
1a
I359
F259
E
8
3
1b
5.1 Å
Y108
2.7 Å
Na1
F253
R30
I359
D404
6a
10

Figure 2.8. Tryptophan is a competitive inhibitor that stabilizes an open-to-outside conformation**.** Solvent-accessible surface of the (**A**) LeuT-Leu (gray) and (**B**) LeuT-Trp complexes (sand/red/magenta). Leucine, tryptophan, Y108, and F253 are depicted in both panels. Distances between Y108 (Cδ1) and F253 (Cζ) in each panel are shown. Helices involved in the domain shift (TM1b, 2a, and 6b) are colored red. (**C**) Cα superposition (depicted as cylinders) of the LeuT- Leu and LeuT–Trp complexes. Colors are the same as in (A) and (B). EL4a, an additional element involved in the domain shift, is magenta. The rotation axes of the two domains are depicted in their respective colors. The bound tryptophans are shown as stick models, with Trp601 colored bright green and the other three colored dark green. TM11 is omitted from the figure for clarity.

(**D**) Close-up of the Cα superposition depicting the hydrogen bonding network in the substrate binding pocket of the LeuT-Trp complex. Note disruption of the critical hydrogen bond between Y108 and the carboxylate of tryptophan, indicated by a double-headed arrow. (**E**) Overlay (in stereoview) of the leucine and tryptophan binding sites to illustrate displacement of the ligand α-amino carboxylate group and concomitant shift in protein and sodium positions. Leucine and tryptophan are colored in magenta and green, respectively.

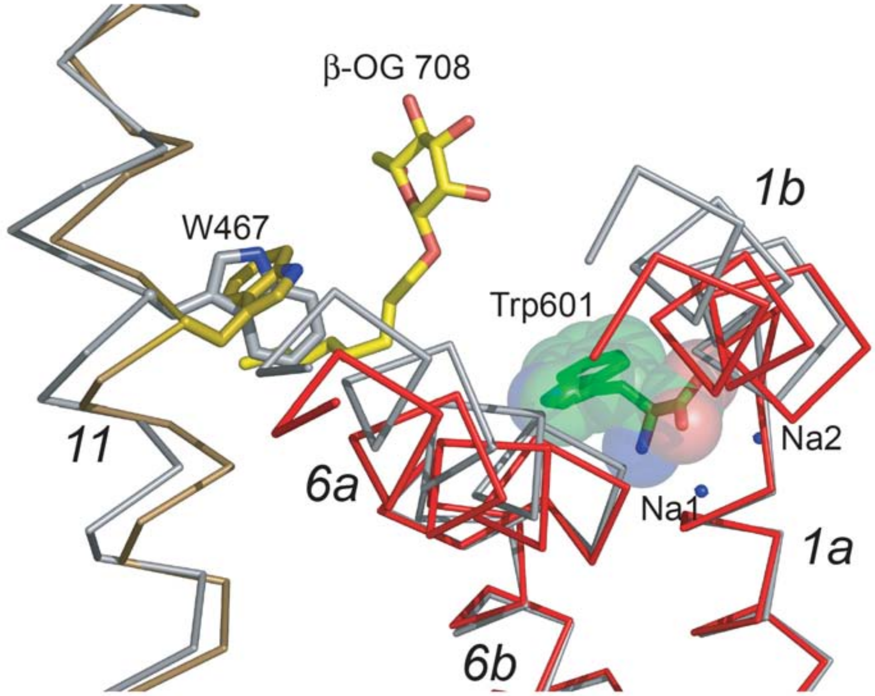

Figure 2.9. Overlay of the LeuT-Trp and -Leu complexes at TM11. Cα traces of TMs1b, 6a, and 11 for the LeuT-Trp (sand and red) and -Leu (gray) complexes. W467 from each structure is also depicted in the same colors. The carbon and oxygen atoms of β-OG 708 from the LeuT-Trp structure are colored yellow and red, respectively.

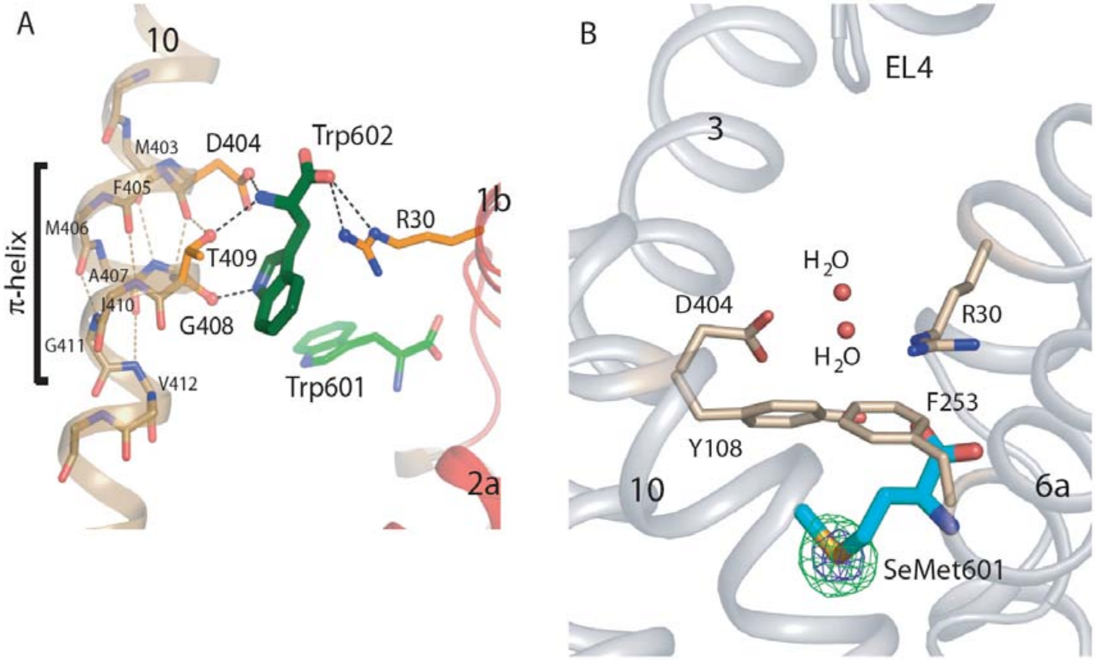

Figure 2.10. A second Trp molecule is bound between R30 and D404 of the extracellular gate only in the open-to-outside conformation. (**A**) Trp602 bound in the extracellular vestibule of LeuT, residing between D404 and R30, flanked by the π-helix in TM10. (**B**) Extracellular vestibule of the LeuT-SeMet complex. Anomalous difference Fourier map (contoured at 5σ and 15σ and depicted in green and blue mesh, respectively) showing no significant density peaks in the extracellular vestibule.

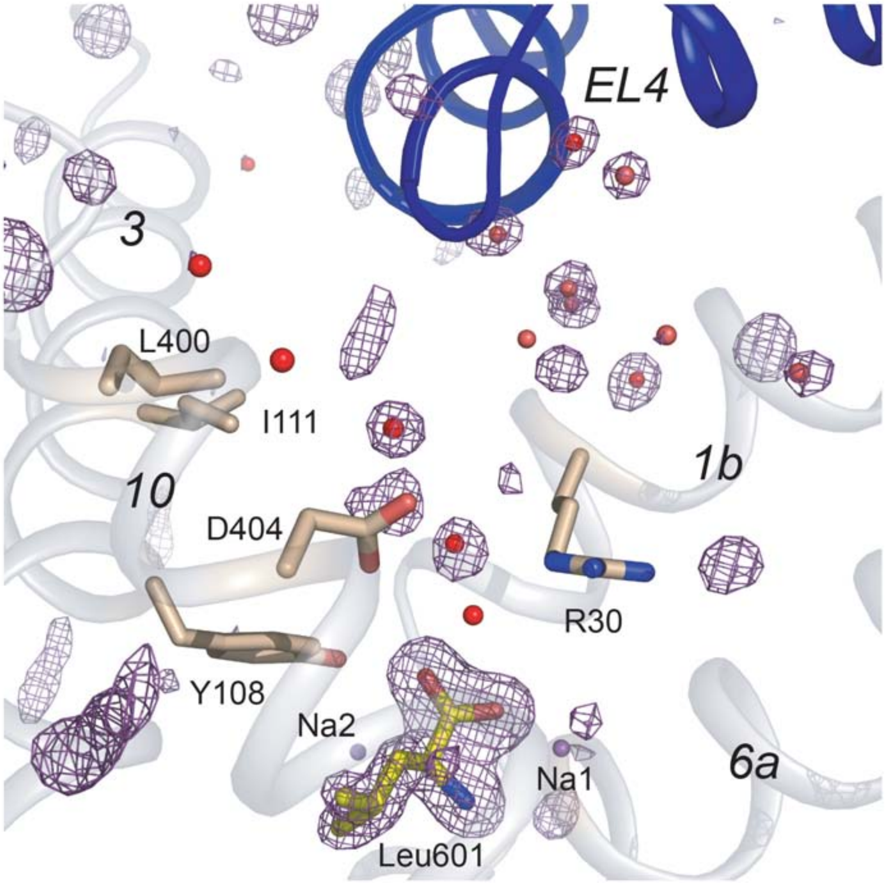

Figure 2.11. View of the LeuT-Leu complex (crystallized in the presence of 30 mM leucine). The extracellular vestibule is shown, along with EL4 (blue), TMs 1b, 3, 6a, and 10 (transparent gray), and residues R30, Y108, I111, L400, and D404. Also depicted are Leu601 (yellow) and water molecules (red spheres) in the vestibule. Simulated annealing F_o-F_c omit map, contoured at 4σ, in which Leu601 and solvent molecules were omitted from the F_c calculation. There is clear density for leucine in the primary substrate binding pocket but not in the vestibule.

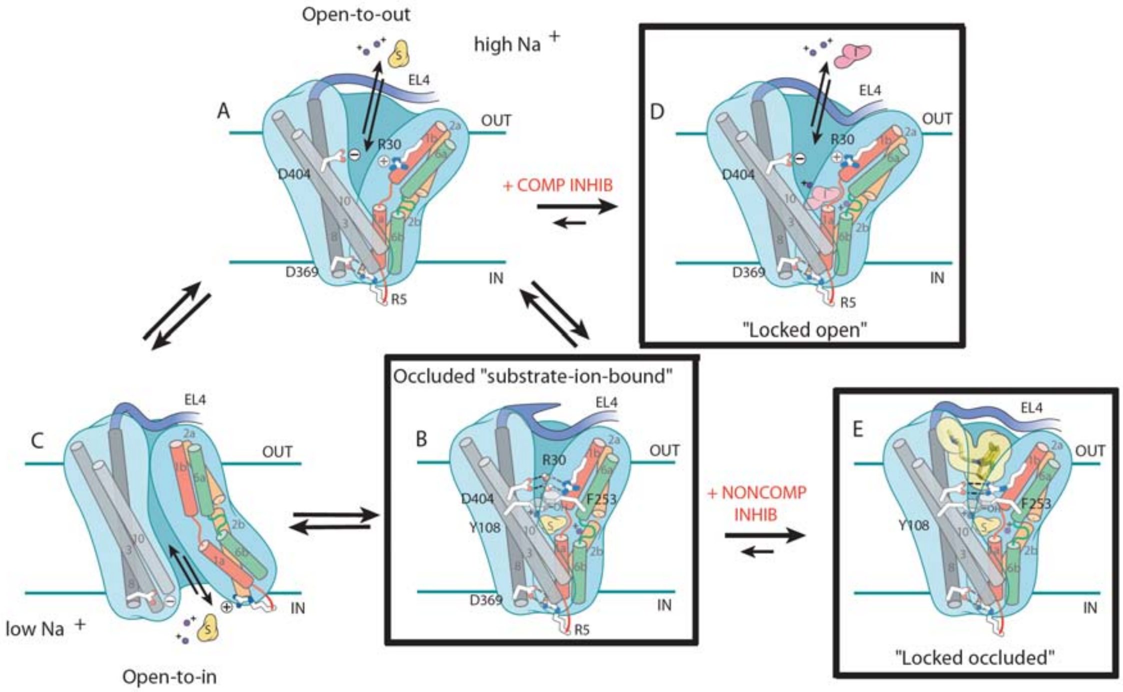

Figure 2.12. Schematic of transport and inhibition in LeuT. Postulated conformational changes associated with isomerization from the open-to-out (**A**) to the outward facing occluded state (**B**) upon binding of substrate and ions, from the occluded (**B**) to open-to-in state (**C**) and dissociation of transported substrate and ions, and from the open-to-in (**C**) back to the open-to-out state (**A**). (**D**) Effect of a competitive inhibitor on transport: stabilizing the open-to-out conformation. (**E**) TCAs are noncompetitive inhibitors that stabilize the occluded state. The boxed conformations represent actual crystal structures, while the unboxed conformations are hypothetical.

URL to access Movie 2.1:
http://www.sciencemag.org/cgi/content/full/322/5908/1655/DC1

Movie 2.1. Structural conformational changes depicted for isomerization of LeuT between the substrate-bound occluded and the competitive inhibitor-bound open-to-out states. The beginning and end states are the crystal structures of the LeuT-Leu and LeuT-Trp complexes, respectively. The structure is viewed parallel to the membrane plane, initially with all helices shown. In the second part, portions of TM10 and TM11 have been removed (residues 407-419 and 450-477) for clarity and residues that comprise part of the extracellular gate (R30, D404, Y108, and F253) are shown as sticks. Coloring is the same as that in Figure 2.3C of the main text. Intermediate states were calculated by linear interpolation between the two sets of crystallographic coordinates as implemented by the CNS morphing script from the Yale Morph Server (http://molmovdb.org) [149, 150].

Chapter 3

Stoichiometry of Substrate Binding to LeuT

The contents of this chapter are published in modified form:

Piscitelli, C.L.*, Krishnamurthy, H.*, Gouaux, E. (2010) Neurotransmitter sodium symporter ortholog LeuT has a single high affinity substrate site. *Nature* 468(7327) 1129-1132

*These authors contributed equally to the work described in this chapter.

Author contributions: CLP, HK, and EG designed all experiments. CLP and HK conjointly carried out the expression and purification of LeuT, performed ITC, equilibrium dialysis, and SPA measurements. CLP performed transport kinetics measurements. CLP, HK, and EG analyzed all data and prepared the manuscript.

Introduction

Neurotransmitter sodium-coupled symporters (NSSs) couple the uptake of neurotransmitter with one or more sodium ions [151-153], removing transmitter from the synaptic cleft. NSSs are essential to the function of chemical synapses, are associated with multiple neurological diseases and disorders [117], and are the targets of therapeutic and illicit drugs [126]. LeuT, a prokaryotic ortholog of the NSS family, is a paradigm transporter for understanding the relationships between molecular mechanism and atomic structure in a broad range of sodium-dependent and sodium-independent secondary transporters [25, 97, 106, 145, 148, 154-156]. At present there is a controversy over whether there are one or two high affinity substrate binding sites in LeuT. The initial crystal structure of LeuT, together with subsequent functional and structural studies, provided direct evidence for a single, high affinity, centrally located substrate binding site, defined as the S1 site [59, 75]. Recent binding, flux, and molecular simulation studies, however, have been interpreted in terms of a model where there are two high affinity binding sites: the central S1 site, and a second site, S2, located within the extracellular vestibule [95] (**Figure 3.1**). Furthermore, it was proposed that the S1 and S2 sites are allosterically coupled such that occupancy of the S2 site is required for the cytoplasmic release of substrate from the S1 site [95]. Here we address this controversy by performing direct measurement of substrate binding to wild-type LeuT and to S2 site mutants using isothermal titration calorimetry, equilibrium dialysis and scintillation proximity assays. In addition, we perform uptake experiments to determine if the proposed allosteric coupling between the putative S2 site and the S1 site manifests itself in the kinetics of substrate flux. We conclude that LeuT harbors a single, centrally located, high affinity substrate binding site and that transport is well described by a simple, single-substrate kinetic mechanism.

Materials and Methods

Mutagenesis and protein purification

Site-directed mutants of LeuT were prepared using the QuickChange kit (Stratagene, Inc.). The Y108F mutant of LeuT was made in the background of the K288A mutation (Y108F-LeuT^K). Wild-type LeuT and mutants bearing a C-terminal His$_8$ tag were expressed in C41 cells and purified as previously described [59] with the exception that cell membranes were washed three times with 50 mM Tris-HCl (pH 8.0) supplemented with 10 mM 1,4,7,10,13-pentaoxacyclopentadecane (15-crown-5) [157] to facilitate the removal of bound leucine and augment the generation of apo-LeuT. Purified protein destined for equilibrium dialysis and ITC assays was concentrated to 5-30 μM using a 50-kDa cutoff concentrator, and dialyzed at 4 °C for 24 hours against buffer I (20 mM Tris-citrate [pH 7.0], 200 mM NaCl, and 1 mM dodecyl maltoside), with three buffer changes. Protein for scintillation proximity assays was purified in buffer II (150 mM Tris-MES pH 7.5, 50 mM NaCl, 1 mM dodecyl maltoside, 20% glycerol) [95]. Equilibrium dialysis assays on wild-type LeuT demonstrate no notable differences using either buffer I or buffer II. Reducing conditions were maintained for preparations of the L400C mutant using 2 mM tris(2-carboxyethyl)phosphine (TCEP). The concentration of protein and ligand used in the ITC measurements was directly determined by quantitative amino acid analysis (qAAA) on material that was subjected to overnight acid hydrolysis in 0.02 *N* HCl. The extent to which the purified LeuT starting material was contaminated by residual leucine was determined by qAAA of non-hydrolyzed material to measure the free amino acid content. All qAAA measurements were performed at the Keck Biotechnology Resource Laboratory (Yale University, New Haven, CT). All other protein concentration measurements were estimated by absorbance spectroscopy using a molar extinction coefficient of 136,459 cm^{-1} M^{-1} at λ = 280 nm for the His-tagged protein, derived from the extinction coefficient predicted from primary sequence (ProtParam, http://expasy.org/tools/protparam.html) and empirically corrected by quantitative amino acid analysis measurements of LeuT (A_{280} of unity = 0.43 mg/ml). Sample purity was assessed by SDS-PAGE under reducing conditions using 12.5% Tris-glycine gels (**Figure 3.2A**) Protein dispersity was monitored by fluorescence-detection size-exclusion chromatography [158] measuring intrinsic tryptophan fluorescence (**Figure 3.2B**).

Isothermal titration calorimetry

A solution of wild-type LeuT or Y108F-$LeuT^K$ (at 20 or 30 μM, respectively, in buffer I) was loaded into the sample cell of an ITC_{200} calorimeter (MicroCal). L-leucine at 200 or 500 μM for titrations with wild-type LeuT or Y108F-$LeuT^K$, respectively, was dissolved in buffer I and loaded into the injection syringe. Prior to data collection, the system was equilibrated to 25 °C with the stirring speed set to 1000 rpm. Titration curves for $Y108F^K$ LeuT binding leucine was generated by five successive 1.5-μl injections followed by fourteen 2.0 μl injections at 180 second intervals. Titration curves for wild-type LeuT binding leucine were generated with nineteen 2.0 μL injections at 180 second intervals. Control injections of ligand into buffer I without protein were done to determine background corrections. The integrated heats from each injection, normalized to the moles of ligand per injection were fit to a single-site binding isotherm [159] using Origin v. 7. Final values of K_D, stoichiometry (N), ΔH, and -TΔS were determined from the average of 2 to 4 ITC runs.

Equilibrium dialysis

For each replicate, 100 μl of either 60 nM wild-type LeuT, 94 nM L400A, or 5.7 μM Y108F-$LeuT^K$ protein in buffer I was placed in the sample chamber, and 300 μl of [^{3}H]leucine at 0.3 to 30 μM (0.27 Ci/mmol) in buffer I was placed in the buffer chamber of a Rapid Equilibrium Device (RED) plate (Thermo Scientific). The unit was covered with sealing tape and incubated at room temperature on a shaker for 6 hours. To determine the concentration of the total and free ligand, 10 μl aliquots were removed from the sample and buffer chambers, respectively, and added to 6 ml of Ultima Gold scintillation fluid. The concentrations of free and total leucine were calculated from the tSIE (transformed spectral index of an external standard) corrected dpm (disintegration per minute) values measured using a liquid scintillation counter. Data were analyzed as a single-site binding function. K_D, B_{max}, and N values were determined from the average of two independent experiments, 2 to 4 replicates each.

Scintillation proximity assays

For saturation binding analysis, 10 nM LeuT was incubated with 2 mg/mL Cu^+-YSi SPA beads in buffer II in the presence of 0.3 to 600 nM [^{3}H]leucine (10.8 Ci/mmol). The reactions were mixed on an orbital microplate shaker at room temperature. Plate readings were taken at 2, 20, 40 and 60 hours using a Wallac Microbeta plate counter, though for each experiment no significant change was observed after 20 hours incubation. SPA experiments to quantify the binding site concentration in each sample were performed as described above, but using 400 nM LeuT and 25 to 1200 nM [^{3}H]leucine (10.8 Ci/mmol). For all assays, specific binding was calculated by subtracting the background radioligand binding assessed by duplicate binding measurements in the presence of 5 mM L-alanine.

Transport time course

LeuT was reconstituted into lipid vesicles as previously described [59] using internal buffer appropriate for the experiment (20 mM HEPES-Tris pH 7, 200 mM KCl or 20 mM citrate-Tris pH 6, pH 5, or pH 4, 200 mM KCl). Transport reactions were assembled by diluting LeuT proteoliposomes to a final protein concentration of 10 μg/mL into external buffer (20 mM HEPES-Tris pH 7.0, 200 mM NaCl or 20 mM citrate-Tris pH 6.0, pH 5.0, or pH 4.0, 200 mM NaCl) at 27 ^{o}C with 500 nM [^{3}H]alanine (83 Ci/mmol). Uptake was followed by removing and quenching 100 μL aliquots of the reaction into ice-cold internal buffer at various time points up to 40 minutes. Reactions were filtered and analyzed as previously described [59]. Non-specific uptake was assessed by repeating the time course for the same liposome preparation under identical conditions except for the replacement of external NaCl by KCl. Non-specific uptake was then subtracted from the total uptake measured to calculate the specific uptake. Each experiment was performed in duplicate.

Steady-state kinetics

LeuT proteoliposomes at 10 μg/ mL were incubated with 0.050 – 8.0 μM [^{3}H]alanine (8.3 Ci/mmol) at 27 ^{o}C for 2 minutes in external buffer (20 mM citrate-Tris pH 5.0, 200 mM NaCl) with or without 50 nM valinomycin. Preliminary time course experiments done at 0.050, 0.40, 1.0 and 8.0 μM [^{3}H]alanine established that transport remained linear through the 2 minute time point. Data from 2 to 4 experiments, each repeated in duplicate, were fit to the Michaelis-Menten equation and analyzed by linear regression to an Eadie-Hofstee transformation.

To test for multi-site cooperative kinetics, data were modeled according to the Hill equation: $v= (V_{max}[S]^n)/(K'+[S]^n)$ allowing the variables, n, K', and V_{max} to float. Alternatively, data were also modeled by a two-site ordered binding equation: $v= (V_{max}(([S]^2)/(\alpha K_s^2)))/(1+([S]/K_s)+(([S]^2)/(\alpha K_s^2)))$ allowing the variables α, K_s, and V_{max} to float. To compare the Michaelis-Menten model to the ordered binding model the F test statistic was calculated according to the GraphPad Prism manual using the following equation: $F= ((SS_{null}-SS_{alt})/(DF_{null}-DF_{alt}))/(SS_{alt}/DF_{alt})$, where *null* and *alt* refer to the Michaelis-Menten and ordered binding models, respectively, and SS is the absolute sum of squares of the variance for each model, and DF is the degrees of freedom for each model. For the Michaelis-Menten model, SS and DF were 3.564×10^7 and 68, respectively. For the ordered binding model, SS and DF were 3.579×10^7 and 67, respectively.

Results and Discussion

LeuT:substrate stoichiometry is 1:1

We first measured the thermodynamic response and stoichiometry of L-leucine binding to LeuT using isothermal titration calorimetry (ITC). To minimize the potential for artifacts in our binding assays arising from endogenously bound leucine co-purifying with LeuT, we extensively washed cell membranes with Na^+-free buffer containing the Na^+ chelator 15-crown-5 [157]. For the wild-type LeuT-leucine interaction, ITC binding isotherms were best fit by a single site model with a substrate to LeuT stoichiometry, N, of 0.70 ± 0.01 and a dissociation constant, K_D, of 54.7 ± 1.8 nM (**Figure 3.3A; Table 3.1**). Binding of leucine to LeuT is driven by enthalpic and entropic factors with a ΔH of -3.93 ± 0.02 kcal mol^{-1} and a $-T\Delta S$ of -6.01 ± 0.13 kcal mol^{-1}. Thermodynamic binding models of higher complexity describing two-site random or two-site sequential binding modes yielded poorer fits to the data, with either high χ^2 values or non-converging parameters.

The measured stoichiometry of 0.70 suggests that approximately 30% of LeuT in the ITC cell is unable to bind titrated substrate. This could be due to incomplete removal of endogenously bound substrate despite extensive 'washing' of the membranes. To weaken substrate binding and thus diminish the relative proportion of leucine-bound LeuT, as well as to specifically probe the interaction of substrate with LeuT, we mutated Tyr108 to Phe (Y108F), thereby disrupting the hydrogen bond between the hydroxyl group of Tyr108 and a carboxylate oxygen of substrate bound to the S1 site [59]. We hypothesized that by ablating the hydrogen bond between Tyr108 and leucine, the Y108F mutation would reduce the enthalpy of leucine binding to the S1 site, thus allowing us to more readily isolate apo-LeuT.

Similar to wild-type LeuT, the binding isotherm for leucine binding to the Y108F mutant was best fit by a single-site model (**Figure 3.3B**). Reflecting the predicted binding site perturbation, the dissociation constant, K_D, increased to 1.4 ± 0.1 μM, and the stoichiometry parameter also increased (N=0.79 ± 0.01) relative to the wild-type transporter (**Table 3.1**). Notably, the ΔH value decreased to -1.92 ± 0.03 kcal mol^{-1}, a difference of 2.01 kcal mol^{-1} from wild-type LeuT and consistent with the loss of a single hydrogen bond between LeuT and a single substrate molecule bound at the S1 site.

Because the stoichiometry values from the ITC experiments ranged from 0.7 - 0.8, we were compelled to determine how much residual substrate remained bound to LeuT. To measure the amount of 'free' amino acid present in our LeuT samples, we employed quantitative amino acid analysis (qAAA). The qAAA results (**Tables 3.2-3.7**) show that the molar ratio of free leucine to LeuT is approximately 6% for Y108F but is negligible for the wildtype preparations. The presence of more free leucine in the Y108F preparations was unexpected and may be due to variations in individual membrane preparations as well as variability in qAAA determinations. Even if all of the free leucine is bound to LeuT, however, the fraction of LeuT bound with substrate does not fully account for the sub-stoichiometric values obtained from ITC. Possible explanations for the sub-stoichiometric binding of substrate are that the LeuT samples used in the experiments contain trace amounts of contaminating proteins, that there is a small amount of protein aggregation as judged by SDS PAGE and fluorescence-detection size-exclusion chromatography, respectively [158] (**Figure 3.2**), or that a fraction of LeuT is not competent to bind substrate.

To corroborate the binding parameters obtained by ITC we used equilibrium dialysis to measure [^{3}H]leucine binding to LeuT. Data for wild-type LeuT and the Y108F mutant were well fit by a single site binding equation (**Figure 3.3C and D**) with respective stoichiometries of 0.73 ± 0.03 and 0.72 ± 0.02 (**Table 3.1**). Taken together, both the ITC and equilibrium dialysis data are consistent with a single substrate binding site. Importantly, the observed differences between wildtype and Y108F demonstrate that we can use the LeuT crystal structure to specifically and predictably perturb binding of substrate to the S1 site.

L400 mutants bind leucine equivalent to wildtype

We next probed the presence of the S2 site by asking if mutations in this proposed site would also measurably perturb binding of substrate to LeuT. In fact, Shi et al. assert that mutation of Leu400 to Cys (L400C) ablates leucine binding to the S2 site, reducing overall binding to LeuT by approximately half [95]. We therefore measured [^{3}H]leucine binding to mutants L400A and L400C. With equilibrium dialysis, we observed that the extent of leucine binding to L400A was comparable to the wild-type transporter (**Figure 3.3C; Table 3.1**). This conclusion was reinforced using the scintillation proximity assay (SPA) method [160] to compare [^{3}H]leucine binding to wildtype, L400A, and L400C (**Figure 3.4A**). In our hands, neither the L400A nor L400C mutant shows any significant change in leucine binding, as measured by maximum binding capacity or dissociation constant, relative to wild-type LeuT (**Table 3.1**).

A limitation of the SPA method is the unreliable determination of the scintillant counting efficiency which, in turn, complicates an accurate conversion of measured radioactivity in counts per minute to moles of radioligand. To circumvent the need for this transformation, we quantified the binding site stoichiometry by titrating transporter protein at 20-fold excess over K_D with 0.06 to 3.0 molar equivalents of [^{3}H]leucine [161]. The resulting response is initially first-order with respect to leucine concentration as binding sites are in excess over ligand. When binding reaches saturation, binding is zero order with respect to leucine concentration. The intersection abscissa of the first-order and zero-order linear regressions provides the ligand concentration equivalent to the binding site concentration, thus defining a stoichiometric value that is independent of ordinate radioactivity conversions. Using this method, we measured [^{3}H]leucine binding to wild-type LeuT and to the L400A and L400C mutants (**Figure 3.4B**). For each of these transporters, binding site saturation occurs at a nearly identical ligand concentration, each corresponding to a substrate to transporter stoichiometry of about 0.8, confirming that mutations at the L400 position do not decrease the binding capacity of LeuT for leucine (**Table 3.1**).

Clomipramine does not inhibit leucine binding

We performed a final saturation binding analysis to assess the effect of clomipramine, an inhibitor of LeuT transport [76, 77] which was proposed to displace leucine binding from the S2 site [95]. In the presence of 10 nM LeuT and 1 mM clomipramine we saw no change in the binding of leucine to wild-type LeuT thus indicating that leucine and clomipramine binding sites do not overlap (**Figure 3.4C; Table 3.1**), consistent with previous data that clomipramine is a noncompetitive inhibitor of LeuT transport [76].

Transport activity is consistent with single-site kinetics

To augment our assessment of binding site stoichiometry, we next asked if LeuT-catalyzed transport is better modeled by a single-site or a two-substrate bound kinetic model. Previously reported flux measurements for several substrates showed that LeuT steady-state kinetics is well described by single-site Michaelis-Menten parameters. The overall slow turnover rate of LeuT under those conditions, however, may have obscured the detection of more complex kinetic behavior. Here, we sought to re-evaluate the kinetics of alanine transport under conditions tailored to promote higher turnover to determine if transport kinetics are better fit by a one- or a two-site model. We first determined that uptake is more robust at acidic pH values with a maximum at pH 5, and that mutation of Lys288, a residue protruding into the hydrophobic portion of the membrane bilayer [59], to Ala (LeuT^K) further enhanced substrate flux (**Figure 3.5**). Steady-state kinetics for alanine uptake by LeuT^K under optimized conditions was measured in the presence of a 200 mM inward Na$^+$ gradient. The data fit well to the Michaelis-Menten rectangular hyperbola with a K_M of 0.79 ± 0.06 μM and V_{max} of 11006 ± 281 pmol min^{-1} mg^{-1} (**Figure 3.6A**). The corresponding turnover number, k_{cat}, is 0.65 min^{-1}, about 6-fold higher than measured for wild-type LeuT at pH 7 with a 100 mM Na$^+$ gradient [75] (**Table 3.8**).

We reasoned that transport would be further stimulated by including valinomycin. Addition of this K^+-selective ionophore will induce a negative-inside membrane potential and prevent the buildup of positive charge inside the liposomes during transport. With valinomycin present, k_{cat} increased to 2.3 min^{-1} yet K_M remained nearly unchanged at 0.75 ± 0.06 μM (**Figure 3.6B; Table 3.8**). Similar to transport under membrane-neutral conditions, valinomycin-stimulated transport is well-fit by a single-site Michaelis-Menten kinetic model.

In conjunction with the Michaelis-Menten modeling, the steady-state kinetic data were fit with alternative kinetic models that describe two-binding site kinetic mechanisms: the Hill equation [162] for a random-order cooperative binding response; and an ordered-binding two-site kinetic model [68]. Data fit to the Hill equation converged with a Hill slope, n_H, of 0.96 +/- 0.03, indicating that there are not multiple, interacting substrate sites underlying the kinetic behavior of LeuT. A two-site ordered binding reaction scheme, which provides explicit treatment for both single and double-occupied transporter-complexes [68], was fit to the flux data. While the value for V_{max} was calculated to be 10965 +/- 308 pmol min^{-1} mg^{-1}, nearly identical to the Michaelis-Menten model, the parameters K_S and the coefficient α converged to 6.8 +/- 22 nM and 114 +/- 360, respectively indicating that the parameters are not well fit by the data.

In conclusion, we have examined the stoichiometry of substrate binding to LeuT using multiple methods and find consistent evidence for a single, high affinity substrate binding site. We find no evidence to support the notion that mutation of Leu400 to Ala or Cys, or the presence of clomipramine, perturbs the stoichiometry of substrate binding. Furthermore, the kinetics of substrate flux is best fit by a single substrate kinetic model. Taken together, these data refute the two substrate binding model for LeuT [95] and is consistent with previously determined crystallographic and functional data [59, 75, 76]. The mechanistic implications of our work are that transport of substrate by LeuT occurs through a singly-occupied intermediate where substrate is bound to a central high affinity site (the S1 site; **Figure 3.1**). We maintain, however, that substrate may indeed transiently bind to weak, low affinity sites as it transits from the extracellular solution to the S1 site and from the S1 site to the intracellular solution, as suggested by previous structural and computational studies [75, 106].

Table 3.1. Binding parameters for leucine binding by LeuT using three methods

	Stoichiometry (mol/mol LeuT)	**B_{max} (cpm/pmol LeuT)**	**K_D (nM)**
ITC			
wildtype	0.70 ± 0.01	-	54.7 ± 1.8
Y108F^K	0.79 ± 0.01	-	1400 ± 100
Eq. dialysis			
wildtype	0.73 ± 0.03	-	122 ± 17
Y108F^K	0.72 ± 0.02	-	2250 ± 138
L400A	0.76 ± 0.12	-	162 ± 2
SPA†			
wildtype	0.80 ± 0.06	5682 ± 310	39.0 ± 3.7
wildtype + CMI	-	5662 ± 197 (99.6%)‡	26.8 ± 4.0
L400A	0.81 ± 0.05	5259 ± 67 (92.6%)‡	20.3 ± 1.2
L400C	0.79 ± 0.04	5147 ± 75 (90.6%)‡	33.5 ± 2.1

† SPA-derived stoichiometry determined from experiments shown in Fig 2b; SPA-derived B_{max} and K_D values from experiments shown in Fig 2a and c.

‡ Values in parentheses indicate B_{max} expressed as percent binding relative to wildtype LeuT.

Table 3.2. Quantitative amino acid analysis (qAAA) of a wildtype LeuT sample used for ITC. Material was subject to acid hydrolysis prior to analysis. Shown below are the values from four well-measured amino acid peaks used to calculate the protein concentration.

Amino Acid	nmoles amino acid from qAAA†	# residues per LeuT molecule	Calculated nmoles LeuT	LeuT conc. (μM)	Mean LeuT conc. (μM)
leucine	2.643	61	0.04333	17.32	19.45
alanine	2.610	54	0.04833	19.33	
tyrosine	0.820	17	0.04823	19.29	
lysine	1.039	19	0.05468	21.87	

† analyte volume = 2.5 μL

Table 3.3. qAAA of wildtype LeuT sample (analyzed in Table 3.2) to determine free amino acid content. Sample was not subjected to hydrolysis prior to analysis**.** Results are shown for the four aliphatic amino acids that bind LeuT with low nanomolar affinity. None were present in detectable quantities. b.d.l. – below detection limit.

Amino Acid	nmoles amino acid from qAAA[†]	concentration (μM)
leucine	b.d.l.	-
isoleucine	b.d.l.	-
valine	b.d.l.	-
methionine	b.d.l.	-

[†] analyte volume = 2.5 μL

Table 3.4. qAAA of titrant solution used for ITC analyses of wildtype LeuT binding leucine. Empirical determination of ligand concentration and the extent of competing amino acids. b.d.l. – below detection limit.

Amino Acid	nmoles amino acid from qAAA[†]	concentration (µM)
leucine	0.4830	193.0
isoleucine	b.d.l.	-
valine	b.d.l.	-
methionine	b.d.l.	-

[†] analyte volume = 2.5 µL

Table 3.5. Quantitative amino acid analysis (qAAA) of a Y108F^K LeuT sample used for ITC. Material was subject to acid hydrolysis prior to analysis. Shown below are the values from four well-measured amino acid peaks used to calculate the protein concentration.

Amino Acid	nmoles amino acid from qAAA†	# residues per LeuT molecule	Calculated nmoles LeuT	LeuT conc. (μM)	Mean LeuT conc. (μM)
leucine	1.841	61	0.03018	30.18	29.94
alanine	1.522	55	0.02767	27.67	
tyrosine	0.491	16	0.03069	30.69	
lysine	0.562	18	0.03122	31.22	

† analyte volume = 1.0 μL

Table 3.6. qAAA of Y108F^K LeuT sample (analyzed in Table 3.5) to determine free amino acid content. Sample was not subjected to hydrolysis prior to analysis**.** Results are shown for the four aliphatic amino acids that bind wildtype LeuT with low nanomolar affinity. Free leucine was measured to be equivalent to 6.2% of the total protein concentration. b.d.l. – below detection limit.

Amino Acid	nmoles amino acid from qAAA[†]	concentration (μM)
leucine	0.118	1.844
isoleucine	b.d.l.	-
valine	b.d.l.	-
methionine	b.d.l.	-

[†] analyte volume = 64 μL

Table 3.7. qAAA of titrant solution used for ITC analyses of Y108F^{K} LeuT binding leucine. Empirical determination of ligand concentration and the extent of competing amino acids. b.d.l. – below detection limit.

Amino Acid	nmoles amino acid from qAAA[†]	concentration (µM)
leucine	1.111	555.5
isoleucine	0.028	14.00
valine	0.020	10.00
methionine	b.d.l.	-

[†] analyte volume = 2.0 µL

Table 3.8. Kinetic constants for alanine uptake by LeuT

	K_M (nM)	V_{max} (pmol/min/mg)	k_{cat} (min^{-1})
LeuT^K pH 5 †	788 ± 59	11006 ± 281	0.65
LeuT^K pH 5 † + valinomycin	747 ± 63	38233 ± 1071	2.3
LeuT pH 7 ‡	583 ± 28	1730 ± 94	0.1

† this study. Values are mean ± s.e.m. from 2 - 4 experiments.
‡ previous study, determined for wildtype [75]. Values are mean ± s.e.m. from 3 experiments.

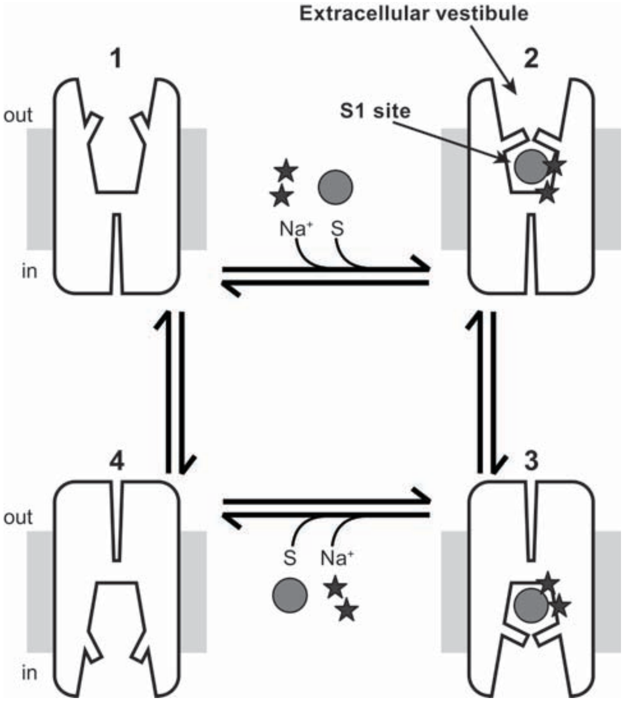

Figure 3.1. LeuT mechanism. Starting from the apo transporter in an open-to-outside conformation (**1**), substrate and sodium ions bind, forming the outward-facing occluded conformation (**2**) characterized by closure of a "thin gate" over the S1 substrate binding site [152]. Clomipramine, which inhibits transport, binds in the extracellular vestibule [76, 77] directly above the thin gate, near the putative S2 site of Shi et al. [95]. The substrate and ion bound transporter undergoes structural isomerization to form the inward-facing conformation (**3**), allowing release of substrate and ions to the intracellular solution, thereby generating an apo transporter, open-to-inside (**4**) which isomerizes to the open-to-outside conformation (**1**).

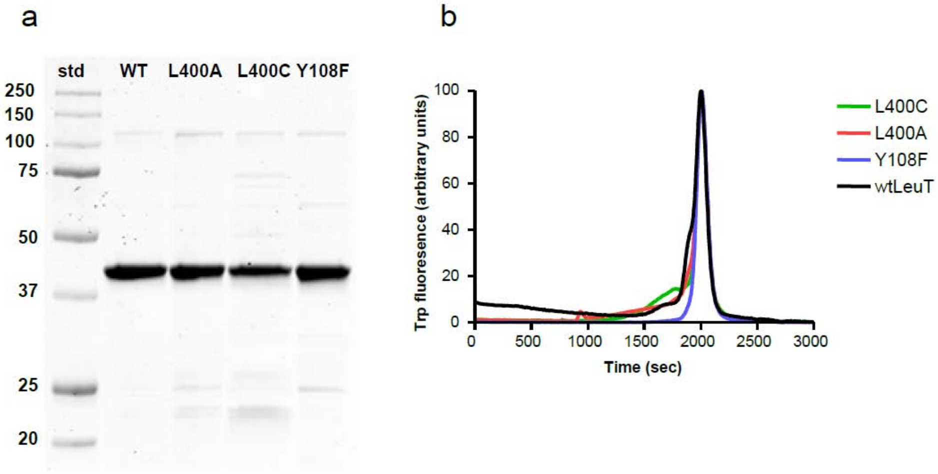

Figure 3.2. Characterization of LeuT. a) SDS-PAGE analysis of purified protein samples used for binding studies. **b)** Assessment of protein monodispersity using fluorescence-detection size exclusion chromatography (FSEC) [158].

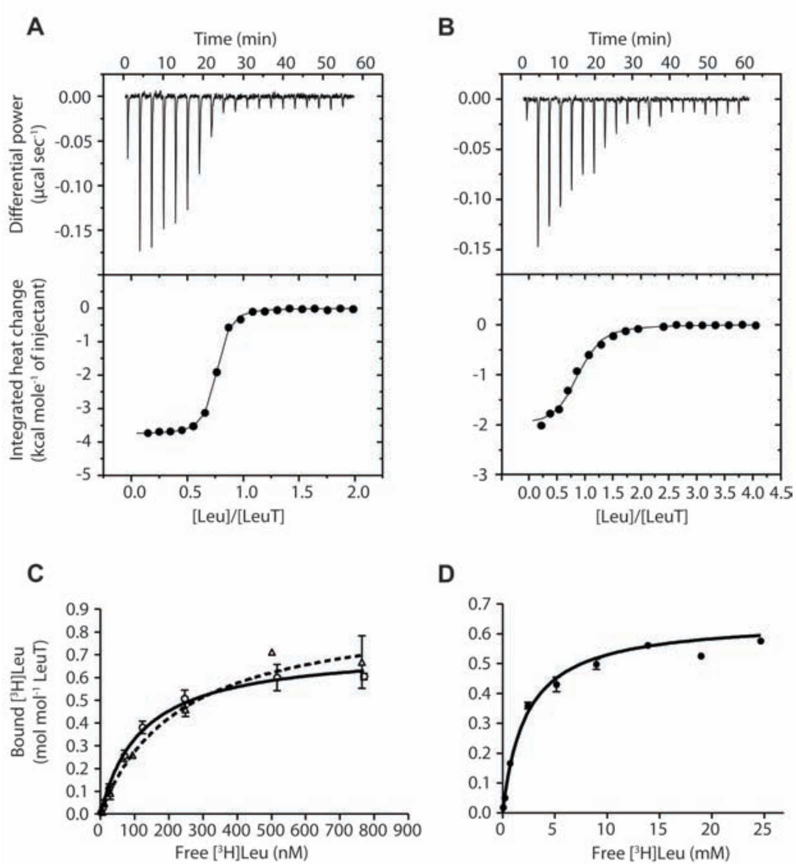

Figure 3.3. Leucine binding measured by ITC and equilibrium dialysis. a) and b) ITC data for **a)** leucine binding to wild-type LeuT and **b)** leucine binding to mutant Y108F-LeuT^K. Raw injection heats (top panel) and the corresponding specific binding isotherms (lower panel) determined at 25 °C and pH 7.0. **c) and d)** Quantitation of [^{3}H]leucine binding stoichiometry by equilibrium dialysis for the **c)** wild-type (open circle, solid line) or the L400A mutant (open triangle, dashed line) or **d)** Y108F-LeuT^K. Errors bars indicate s.e.m., n=2.

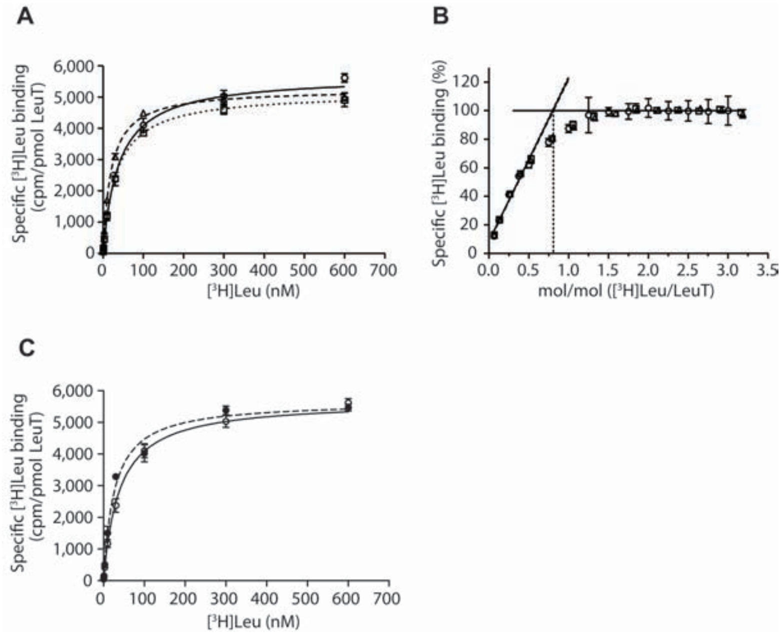

Figure 3.4. Leucine binding measured by scintillation proximity assays. a) Saturation binding isotherms and nonlinear regression analysis for wild-type (open circle, solid line), L400A (open triangle, dashed line), and L400C (open square, dotted line). **b)** Saturation binding at high LeuT concentration (approx. 20 x K_D) to quantify substrate binding stoichiometry. Symbols and lines are as in panel **a**. **c)** Saturation binding for wild-type LeuT in the absence (same data shown in panel **a**) or presence of 1 mM clomipramine (closed circle, dashed line). Error bars indicate s.e.m., n=2.

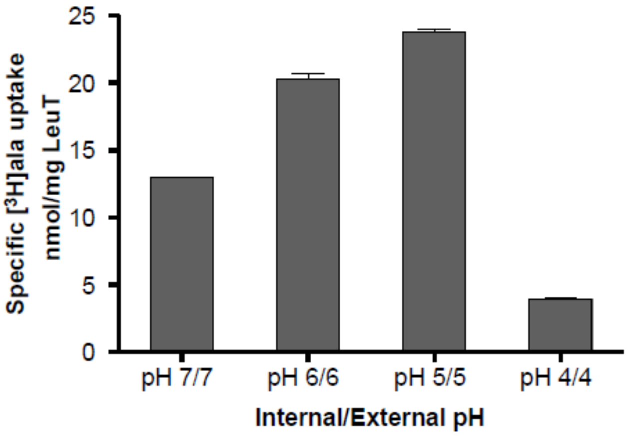

Figure 3.5. pH dependence of [^{3}H]alanine transport. Alanine uptake into LeuT^K proteoliposomes after 10 minutes at specified pH values. Errors bars are s.e.m. (n=2).

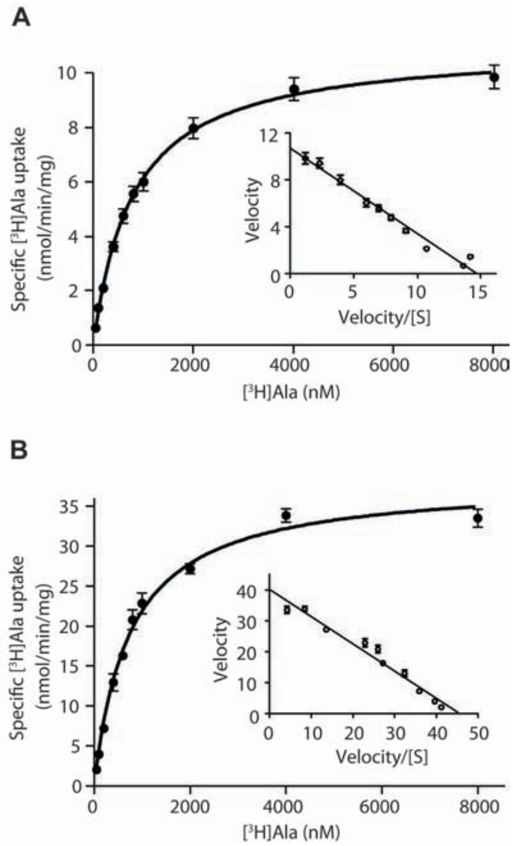

Figure 3.6. Transport kinetics of [^{3}H]alanine uptake. **a)** Steady-state alanine uptake as a function of alanine concentration at pH 5. Shown in the inset is the corresponding Eadie-Hofstee plot with linear regression ($r^2 = 0.93$). Error bars indicate s.e.m., n=4. **b)** Steady-state alanine uptake at pH 5 in the presence of valinomycin to induce a membrane potential. Shown in the inset is the corresponding Eadie-Hofstee plot with linear regression ($r^2 = 0.96$). Error bars indicate s.e.m., n=2.

Chapter 4

Engineering Tryptophan Transport Activity into LeuT

The contents of this chapter are pending submission as:

Piscitelli, C.L., and Gouaux, E. Insights into transport mechanism from LeuT engineered to transport tryptophan

Author contributions: CLP and EG designed all experiments, analyzed the data, and prepared the manuscript. CLP performed all experiments.

Abstract

Neurotransmitter/Sodium Symporters (NSS) are a family of transporters that catalyze the reuptake of neurotransmitters from neural synapses. To date, the bacterial ortholog LeuT, an aliphatic amino acid transporter that is inhibited by tryptophan, is the only member of the NSS family to have been structurally characterized by X-ray crystallography. Because of this, the crystallographic and functional analysis of LeuT has yielded fundamental insights into the mechanism of the NSS family at large. In this work we harness the analytical combination of crystallography with radioligand binding and transport assays to characterize variants of LeuT that have been mutated to “engineer” altered substrate transport specificity. While wildtype LeuT is inhibited by tryptophan, which locks in the transporter in an open-to-out conformation, we show that simple substitutions, derived from sequence alignment with the related tryptophan transporter TnaT, introduced into the binding site of LeuT allows tryptophan to bind such that LeuT adopts the occluded state and results in a gain of tryptophan transport function. The conformational shift from open-to-out to the occluded state with tryptophan bound abolishes the second extracellular vestibule tryptophan binding site, indicating that the existence of this second site is conformationally dependent. Altogether, these data demonstrate the link between the functional and structural states of the transporter and show that a necessary step in the transport cycle is the formation of the occluded state, which is determined by the protein:ligand binding complementarity in the central binding site. The ability to easily transfer function

between NSS family members suggest these mechanistic insights into LeuT structure and function can be generalized to other NSS members.

Introduction

Rapid transport of polar solute molecules across biological membranes is accomplished by a diverse array of transporter proteins specialized for different physiological functions. The Neurotransmitter/Sodium Symporter (NSS) family of transporters (TC# 2.A.22 [11]) function at neuronal synapses in the reuptake of biogenic amine and amino acid neurotransmitters from the synaptic cleft into surrounding cells [37, 46, 163]. The central role of NSS members in neural physiology and disease is reflected in the large number of therapeutic and illicit drugs that target these transporters [61, 164]. Because of this, the mechanism of these transporters has been under study for decades. Recently, structural studies of a prokaryotic homolog of the NSS family, LeuT, have produced high-resolution crystallographic snapshots of the transporter showing the three-dimensional organization of functional elements conserved across the NSS family and providing insight into how substrates and inhibitors interact with the transporter [59, 75-78]. Correlating structure and function through crystallographic and biophysical measurements in LeuT is thus a potent means to understand mechanistic principles of the NSS family [75, 165].

Previous studies have shown that LeuT functions in the sodium-dependent binding and transport of aliphatic and aromatic amino acids [59, 75, 76]. Amino acid transport is limited by the size of the ligand, and it was shown that while tyrosine can be transported, tryptophan is not and is in fact a competitive inhibitor of LeuT

[75]. Crystal structures of LeuT in complex with transportable ligands and with tryptophan showed that while all transportable ligands, including the isosteric tyrosine analog 4-fluoro phenylalanine (4-F-Phe), adopt the same occluded conformation, the non-transportable tryptophan molecule binds LeuT in an open-to-out conformation with tryptophan bound not only in the central binding site (Trp 601) but also at a new site (Trp 602) between conserved residues R30 and D404, formed by the more open extracellular vestibule [75]. We reasoned that the change in ligand size and electrostatics between tyrosine (or 4-F-Phe) and tryptophan represented a fundamental limit in the substrate specificity profile of LeuT which is structurally correlated to the ability of LeuT to form the occluded state upon substrate binding. If the occluded state is blocked, then the transporter is prevented from progressing through the transport cycle [75, 152]. Accordingly, we hypothesized that tryptophan is an inhibitor because it prevents the formation of the occluded state and locks the transporter open. Thus, the occluded state is a necessary transport intermediate and that transport specificity is a result of the complementarity between the transporter and ligand bound in the central binding site which determines the ability of the complex to form the occluded state. The change in complementarity that occurs between tyrosine and tryptophan therefore defines a mechanistic boundary between substrate and inhibitor.

In this work, we undertake experiments that demonstrate how the ligand-protein complementarity determines transport specificity and the functional link to the structural state of the transporter. We show that a single mutation in the binding site is sufficient to shift the substrate specificity profile of LeuT to transport tryptophan. We further show that this change in functional specificity is accompanied by a structural change whereby LeuT adopts the occluded conformational state when bound to tryptophan, thus demonstrating a link between functional activity and structural state. Finally, we observe that the vestibule R30-D404 tryptophan binding site that exists in the open-to-out state is absent in the tryptophan-bound occluded state. This shows that the wild-type transporter is locked in the open-to-out state by the tryptophan bound in the primary site and the occupancy of the Trp 602 site is a consequence of this trapping effect. This suggests that the Trp 602 site in the open-to-out state is a transient binding site for substrates that defines part of the permeation path through the transporter and its occupancy is strictly dependent on the overall conformational state.

Materials and Methods

Homology modeling of TnaT

Pairwise alignment of the TnaT sequence from *Symbiobacterium thermophilum* (GenBank accession BAA24689.2) with LeuT was performed using ClustalW (http://www.ebi.ac.uk/Tools/clustalw2/index.html). A three-dimensional model of TnaT was constructed using the Swiss-Model [166] web interface from the ClustalW-generated sequence alignment and the coordinates of the occluded-state LeuT structure (PDB ID 2A65). Similar results were achieved using Modeller 9v5 [167] both with and without explicit modeling of the bound sodium ions. Tryptophan and sodium was modeled manually into the resulting homology model of TnaT guided by the locations of the ions and the α-amino and -carboxylate position of bound leucine in the template LeuT structure. The model of TnaT bound with sodium and tryptophan was subjected to a round of geometrical energy minimization to alleviate clashes using Refmac5 [138, 168, 169].

Expression and purification

LeuT was expressed and purified as previously described [59, 75]. Mutations were introduced by polymerase chain reaction using the QuikChange method (Stratagene, Inc.). All binding and transport assays were conducted with LeuT constructs containing the K288A background mutation (LeuT^{K}) [91]. To displace endogenously bound high-affinity ligands, protein was solubilized from membranes in the presence of 100 mM L-alanine followed by purification either without added ligand (for binding and transport assays) or with 50 mM L-tryptophan (for crystallization of LeuT-Trp complexes).

Preparation of LeuT proteoliposomes

LeuT was reconstituted into proteoliposomes at a protein:lipid ratio of 1:100 (w:w) as previously described [76]. Reconstitution was carried out in the presence of 20 mM HEPES-Tris pH 7, 100 mM KCl. Proteoliposomes were concentrated by centrifugation at 300,000 x *g* for 30 minutes and resuspended in reconstitution buffer to a protein concentration of 0.5 mg/mL, determined by the modified amido black assay method [170]. Proteoliposomes were flash-frozen in liquid N_2 and stored at -80 °C. Prior to each assay, proteoliposome stock suspension was thawed then diluted 25-fold into internal buffer (20 mM HEPES-Tris pH 7, 500 mM KCl), subjected to two freeze/thaw cycles in liquid nitrogen and room temperature water and reconcentrated by centrifugation at 300,000 x g for 30 minutes. The pelleted proteoliposomes were resuspended back to the original volume using internal buffer. The resuspended liposomes were then extruded using an Avestin Mini-extruder coupled to two 1 mL Hamilton syringes with a 400 nm polycarbonate filter, passing the suspension through the filter 15-21 times.

Transport assays

For time course assays, reactions were initiated by adding proteoliposomes into external buffer (20 mM HEPES-Tris pH 7, 500 mM NaCl) at 27 ^{o}C with 1.2 μM [^{3}H]tryptophan (20 Ci/mmol) or 1 μM [^{3}H]tyrosine (40 Ci/mmol). Final LeuT concentration was 8 μg/mL. At time points, 100 μL of reaction mix was removed and quenched in a glass test-tube containing 1.8 mL of ice-cold internal buffer.

For the steady-state kinetic measurements, proteoliposomes were diluted into external buffer at 27 ^{o}C with 0.3 – 400 μM [^{3}H]tryptophan (0.2 Ci/mmol). Final LeuT concentration was 16 μg/mL. Reactions were incubated for 2 minutes, then 100 μL from each was quenched in a glass test-tube containing 1.8 mL of ice-cold internal buffer. For both time-course and steady-state assays, nonspecific uptake was assessed by control reactions in the absence of sodium. After each time or concentration series was collected, quenched reactions were filtered through GSWP02500 nitrocellulose filters, pre-wetted with ice-cold internal buffer, followed by three 2 mL washes with ice-cold internal buffer. Filters were placed in glass scintillation vials, 6 mL of Ultima Gold scintillation fluid was added and filters were allowed to dissolve for ~5 hours before measuring tSIE-corrected dpm values using the Packard TriCarb LSC. Data was analyzed using GraphPad Prism version 4.0. Steady-state measurements were fitted with a Michaelis-Menten equation or subjected to an Eadie-Hofstee transformation and analyzed by linear regression.

Binding assays

For saturation binding analysis, 70 nM LeuT with C-terminal His_8 tag was incubated with 2 mg/mL Cu^+-YSi SPA beads (GE Healthcare) in binding buffer [20 mM HEPES-Tris pH 7, 100 mM NaCl, 1 mM $C_{12}M$] in the presence of 0.3 to 600 μM [^{3}H]tryptophan (0.2 Ci/mmol) in a white-walled clear bottom 96-well Isoplate (Perkin Elmer). The reactions were mixed on an orbital microplate shaker at room temperature. Prior to reading, each plate was allowed to rest for at least one hour to allow the beads to settle. Readings were taken at 2, 20, 40 and 60 hours, though for each case no significant change was observed after 20 hours incubation. Radioactivity from each well was read using a Wallac Microbeta plate reader specifying sample type as SPA and measuring detector-normalized counts per minute. Nonspecific radioligand binding was assessed by parallel binding measurements with 5 mM unlabeled leucine added. Specific binding was determined for each experiment by the difference between the mean of duplicate measurements of total and nonspecific binding. Data was analyzed using GraphPad Prism version 4.0.

Crystallization, data collection, model refinement

LeuT constructs with the binding site mutations F259V, I359Q, and F259V+I359Q, fractioned by size-exclusion chromatography in the presence of 40 mM β-octyl glucoside and 50 mM L-tryptophan as described [75], were concentrated to 3 - 4 mg/mL and dialyzed overnight against crystallization buffer [20 mM HEPES pH 7, 200 mM NaCl, 40 mM β-octyl glucoside, 50 mM L-tryptophan] using a 25,000 kDa MWCO membrane. Hanging-drop crystallization screens were set up in 24-well plates with 100 mM HEPES pH 7 or pH 7.5, 200 or 400 mM NaCl and 16 - 26 % PEG 550-MME at protein:reservoir ratio of 1:1, 2:1, and 1:2 (v:v). Plates were incubated at 20 °C and in the dark to minimize photo-oxidation of tryptophan [132, 171]. Crystals of a rod-like morphology grew to 20 – 100 μm in the smallest dimension within 7-10 days and were harvested and cryoprotected as described previously [59]. Diffraction screening was carried out using synchrotron radiation at the Advanced Light Source, beamlines 8.2.1, and 5.0.2 (Lawerence Berkeley National Lab, Berkeley, CA) and at the Advanced Photon Source, beamline NE-CAT 24-ID E (Argonne National Lab, Chicago, IL). The best-diffracting crystals typically grew at 20-24 % PEG 550-MME at both 200 mM and 400 mM NaCl.

Datasets from cryogenically cooled crystals were collected with $\lambda = 1.000$ Å, $\Delta\varphi = 0.5 - 1.0^{\circ}$ per frame, with a minimum of 180° total crystal rotation. Data was indexed, integrated, and scaled using HKL2000 [134]. Molecular replacement was carried out with data from each crystallization experiment using MolRep [172] with either the occluded state structure of LeuT (PDB ID 2A65) or the open-to-out structure (PDB ID 3F3A) with all ligands removed as the search model. The highest scoring solution was then subjected to an initial round of rigid-body refinement followed by simulated annealing and iterative rounds of positional and B-factor refinement with manual model rebuilding using Phenix [173] and Coot [142] with geometrical validation using Molprobity [174]. Complete data collection and refinement statistics are reported in **Table 4.1**.

Results and Discussion

LeuT-TnaT sequence alignment suggests altered binding site within a conserved structure

To gain insight into the nature of transport vs. inhibition, we began by comparing the sequences of LeuT with TnaT, a related bacterial NSS homolog that transports tryptophan [56]. The sequence alignment shows that while the overall conservation is about 29%, the regions that are involved with substrate and ion binding and permeation are highly conserved with approximately 50% conservation of TM1 and TM6 and strict conservation of isolated elements implicated in transporter function [69]. This pattern of conservation is similar to that observed in sequence alignments of LeuT with eukaryotic NSS transporters. Because we were interested in determinants of substrate specificity, in particular how TnaT provides extended specificity for larger amino acids, we looked more closely at the residues of TnaT that align with the residues that form the binding site of LeuT (**Figure 4.1A**). We found that most of the binding site residues with side chains that contact bound substrate in LeuT have shared identity between LeuT and TnaT with two exceptions, F259 and I359. In TnaT these residues are substituted by valine and glutamine, respectively (**Figure 4.1A**).

TnaT homology model suggests binding site substitutions are specificity-altering

A homology model of TnaT helps to illustrate these substitutions in the three-dimensional context of the binding site (**Figure 4.1B**). In LeuT, F259 and I359 sidechains participate in van der Waals interactions with the sidechain of bound substrate such as leucine. In the tryptophan-bound structure of LeuT in the open-to-out conformation, the tip of the indole ring of bound tryptophan is braced against I359 and Y108, while the ring N-H group contacts the aromatic face of F259 forming a π-electron mediated interaction. The substitutions in TnaT significantly alter the environment of the binding pocket. The substitution of the I359 *sec*-butyl group, a branched non-polar sidechain, with the glutamine propylamide, an unbranched polar sidechain, presents a drastic chemical change in terms of both sterics and electrostatics. The other substitution of the F259 phenyl group with the smaller isopropyl group of valine removes the π-electron face from the binding site and also changes the shape of the binding pocket.

These observations suggest that the extended specificity of TnaT for tryptophan relative to LeuT is founded, at least in part, on altered complementarity of the binding site. Previously we observed that steric and electrostatic complementarity of ligand:binding site interactions contribute to the uptake specificity of the transporter [75]. We hypothesize that correct complementarity allows the transporter to adopt the occluded state upon substrate binding which we believe is a necessary intermediate in the transport cycle. Poor complementarity that inhibits formation of the occluded state causes competitive transport inhibition, which is observed with tryptophan binding LeuT. Thus, the fundamental difference between LeuT and TnaT is the altered complementarity in the binding site for tryptophan. Accordingly, we surmise that TnaT transports tryptophan because the ligand is accommodated in an occluded state. Extending this idea to LeuT - binding site mutations in LeuT that confer tryptophan transport should also confer adoption of the occluded state for the tryptophan-bound transporter. We sought to test this hypothesis by constructing LeuT mutants that contain the TnaT binding site substitutions F259V and I359Q to see if we can, in fact, observe a correlation between a gain of tryptophan transport function and a change in the conformational state that tryptophan binding stabilizes.

I359Q substitution in LeuT confers tryptophan transport activity to LeuT

LeuT variants incorporating either both substitutions (LeuT$^{F259V+I359Q}$) or each individually (LeuT^{F259V} and LeuT^{I359Q}) were purified and reconstituted into liposomes for transport analysis. The ability of each variant to transport [^{3}H]tyrosine and [^{3}H]tryptophan was measured in a time course assay. Tyrosine was chosen as an assay ligand because it is the largest amino acid that wildtype LeuT can transport [75] and therefore we reasoned that it would present a more sensitive functional readout of substitutions in the binding pocket that interact with the substrate amino acid sidechain. As expected from previous work [75], wildtype LeuT does not transport tryptophan under these conditions but does demonstrate measureable tyrosine transport (**Figure 4.2A and Figure 4.3**). The single substitution LeuT^{F259V} also does not transport tryptophan which suggests that the F259V substitution alone is insufficient to extend the substrate specificity of LeuT. The F259V variant, however, also displayed reduced tyrosine transport suggesting that the F259V substitution induces changes in the transporter that are sub-optimal in the context of LeuT.

Conversely, the single I359Q substitution demonstrated a significant gain of tryptophan transport function (**Figure 4.2A**). When I359Q is incorporated together with F259V, the double variant also shows measurable tryptophan transport activity, though it is significantly reduced compared to the single I359Q variant. This is consistent with the idea that F259V alters LeuT negatively, opposing the I359Q gain of function, and likely requires additional substitutions within the surrounding environment to bolster tryptophan transport activity.

F259V does not inhibit binding of trp to LeuT

To determine if the F259V substitution opposes transport by inhibiting tryptophan binding, we measured binding of [^{3}H]tryptophan to LeuT and the three variants. We found that none of the substitutions dramatically affect equilibrium binding of tryptophan, each binding tryptophan with an apparent K_d of ~ 20 μM (**Figure 4.2B**), which rules out the possibility that F259V reduces transport activity by inhibiting tryptophan binding.

Steady-state kinetics of trp transport by LeuT^{I359Q}

The activity of LeuT^{I359Q} was further characterized by measuring the steady-state kinetics of [^{3}H]tryptophan transport. The data were well-fitted by a single-site Michaelis-Menten model ($R^2 = 0.991$) with kinetic parameters of $K_M = 78.9 \pm 8.8$ μM and $V_{max} = 7504 \pm 340$ pmol min^{-1} mg^{-1} (**Figure 4.2C**). The corresponding turnover rate k_{cat} is approximately 0.6 min^{-1}, which is within the range of turnover rates previously reported for transport activity by wildtype LeuT [75, 76]. Altogether, these uptake and binding data demonstrate that the single substitution, I359Q, derived from TnaT, is sufficient to alter the substrate specificity profile of LeuT, introducing a gain-of-function activity to the transporter.

Trp transport active LeuT mutants bind trp in the occluded state

In order to understand the structural basis for the I359Q gain of function phenotype, we co-crystallized each of the three LeuT binding site variants with tryptophan and determined the crystal structures by X-ray diffraction (see **Table 4.1** for data collection and refinement statistics). The structure of the tryptophan transport negative variant LeuT^{F259V} in complex with tryptophan is nearly identical to the wildtype LeuT-Trp structure previously described [75] (**Figure 4.4A and C; Figure 4.5**). LeuT^{F259V}-Trp adopts an open-to-out conformation marked by a solvent accessible pathway through the extracellular vestibule into the central substrate binding site (**Figure 4.4B**) with a second tryptophan molecule (Trp 602) bound in the extracellular vestibule between the extracellular gate residues R30 and D404 (**Figure 4.5B**). We previously proposed that this open-to-out conformation signifies a competitively inhibited state where the transporter is locked open and prevented from progressing through the transport cycle due to steric hindrances from the tryptophan bound in the central site. Because the F259V variant also does not transport tryptophan, it is therefore consistent with the wildtype transporter structure that the LeuT^{F259V}-Trp structure similarly yields a competitively inhibited state in the same conformation.

The structures of LeuT^{I359Q} and LeuT$^{F259V+I359Q}$ bound with tryptophan, both of which demonstrated a gain of tryptophan transport activity, by contrast adopt the occluded state conformation in complex with tryptophan (**Figure 4.4B and D**). From the structure of LeuT^{I359Q}-Trp we see that the glutamine introduces both steric and electrostatic changes that cause the indole ring of the bound tryptophan to rotate downward towards the intracellular side of the transporter (**Figure 4.4D**). When we compare the tryptophan bound LeuT^{I359Q} occluded state structure with the wildtype open-to-out structure (**Figure 4.4E and F**) we find that, in the wildtype transporter, the indole ring of tryptophan is nestled into a cleft between the hydroxyphenyl ring of Y108, which contributes an edge-face aromatic interaction, and the *sec*-butyl sidechain of I359 (**Figure 4.4C**). The conformational isomer of tryptophan that binds the open-to-out state is therefore stabilized in this more elongated state spanning the open binding site and preventing the inward "collapse" of the binding site to form the occluded state.

In the I359Q substitution the glutamine sidechain is extended toward Y108 where the amide head group instead interacts with the aromatic face of the Y108 sidechain (**Figure 4.4D**). The indole moiety of tryptophan is therefore precluded from binding with Y108, thus the ligand adopts a more compact conformation where the indole ring is rotated by ~30° about the χ2 torsion. This rotation situates the indole ring such that the aromatic face interacts with the Nε of the glutamine amide group as well as putative C-H interactions with the Cγ methylene. The cytoplasmically-oriented indole ring now interacts directly with N21, resulting in about a 90° rotation of the asparagine amide sidechain, engaging it with the aromatic face of the conserved Y265 residue, forming part of a putative intracellular gate network (**Figure 4.6**). Thus, the I359Q substitution alters the LeuT binding site interaction network, enabling tryptophan to bind with complementarity that allows the transporter to isomerize to the occluded state.

The Trp602 site is absent in the Trp-bound occluded state

The LeuT^{I359Q} and LeuT$^{F259V+I359Q}$ complexes with tryptophan demonstrate that a single tryptophan molecule binds in the central, S1 binding site. Furthermore there is no evidence for a second tryptophan bound within the extracellular vestibule. Similar to the wild type occluded state structures, in the engineered tryptophan transporter structures, extracellular gate residues R30 and D404 are engaged in a water-mediated ionic bridge (**Figures 4.7 and 4.8**), ablating the binding of Trp602. This illustrates that the Trp602 site is strictly dependent upon the conformation of the transporter and that in the open-to-out facing structures its presence is not simply an artifact of co-crystallization.

A structural description of the transport cycle

Our crystal structures of LeuT bound to tryptophan in two functional states, together with previous structure-function data provide evidence that the transport cycle of LeuT begins with an open-to-out state in which the conserved extracellular gate residues are open [92], forming an electrostatically polarized pathway between conserved residues R30 and D404 to recruit ligands into the extracellular vestibule (**Figure 4.6A**). This polarized pathway might transiently bind substrates as they permeate through the transporter into the central substrate binding site (**Figure 4.6B**) which could aid in orienting the substrate and possibly providing first-pass substrate selection. Indeed, TM10 residues that interact with Trp602, including D404, break from the normal α-helix structure to form a π-helix which are energetically costly to maintain in protein structures and generally indicate regions of functional importance [175, 176]. After passing through the extracellular gate, substrate binds into the central site (**Figure 4.6C**) whereupon, given the correct complementarity, the transporter closes the extracellular gate, forming an occluded state (**Figure 4.6C**). The transporter can then isomerize to open the conserved intracellular gate [71] (**Figure 4.6D**), allowing substrate and/or ions to dissociate (**Figure 4.6E**). The opening of the intracellular gate has not been observed crystallographically, but is postulated to involve outward movements of TM1a and TM6b based upon the 2-fold pseudosymmetry of TMs 1-5 and 6-10 [59, 72], single molecule FRET studies [93], substituted cysteine accessibility assays [71, 72] and molecular modeling [72, 93, 100].

Table 4.1. Crystallographic data collection and model refinement statistics

Data collection	LeuT(F259V)-Trp	LeuT(I359Q)-Trp	LeuT(F259V)(I359Q)-Trp
Space group	C2	C2	C2
Unit cell dimensions (Å)	a = 90.2 b = 86.6 c = 82.1	a = 90.9 b = 87.1 c = 81.9	a = 91.8 b = 87.1 c = 82.2
	α = 90.0 β = 93.6 γ = 90.0	α = 90.0 β = 94.8 γ = 90.0	α = 90.0 β = 94.7 γ = 90.0
Resolution	50.0 – 2.63 (2.74 – 2.63)	50.0 – 2.60 (2.69 – 2.60)	50.0 – 2.80 (2.90 – 2.80)
Total observations	68853	49524	57879
Unique reflections	18602 (1840)	19270 (1905)	15756 (1556)
Rsym (%)	4.4 (41.8)	5.6 (42.4)	8.0 (80.3)
Completeness (%)	99.6 (99.2)	97.8 (98.1)	98.3 (98.6)
Redundancy	3.7 (3.7)	2.6 (2.6)	3.7 (3.5)
I/σ	16.1 (2.00)	12.2 (1.84)	15.3 (1.50)
Wilson B-factor (Å2)	51.28	46.55	49.15
Refinement			
Refinement range	45.0 – 2.63 (2.80-2.63)	31.4 – 2.60 (2.76 – 2.60)	33.5 – 2.80 (3.02 – 2.80)
Total atoms	4146	4134	4130
Waters	33	12	12
Rcryst (%)	21.4 (28.1)	20.1 (24.3)	20.0 (24.3)
Rfree (%)	22.8 (30.2)	24.1 (30.8)	23.7 (31.4)
Bond length deviation (Å)	0.002	0.004	0.002
Bond angle deviation (o)	0.559	0.656	0.563
Average B value (Å^2)	68.66	58.98	57.67
Ramachandran plot, favored (%)	96.00	98.42	97.62
Ramachandran plot, disallowed (%)	0	0	0

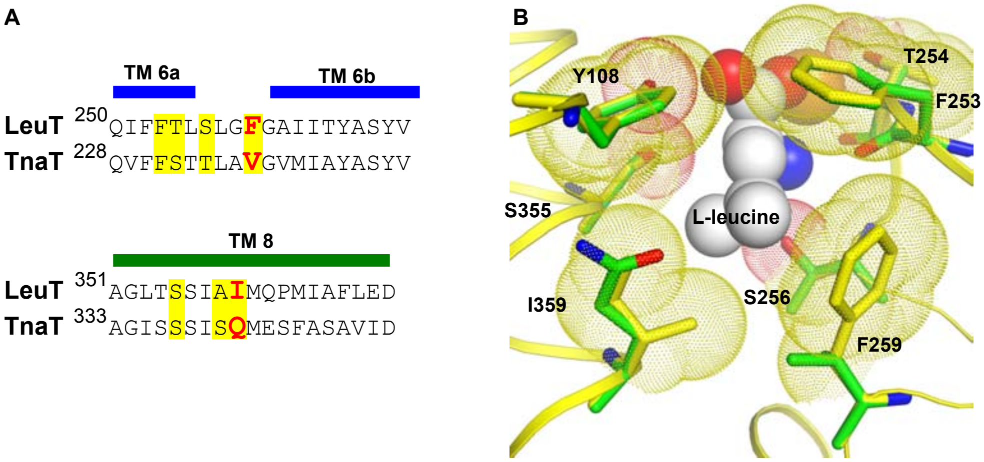

Figure 4.1. (**A**) Sequence alignment of LeuT and TnaT, showing the regions of TM6 and TM8 that contribute to the binding site in LeuT. Yellow highlights indicate residues which contribute sidechain interactions to the substrate in LeuT crystal structures. Shown in red lettering are the residues F259 and I359 in LeuT that are substituted by V and Q, respectively, in TnaT. (**B**) Overlay of the LeuT-leucine crystal structure (yellow; PDB id 2A65), and a homology model of TnaT (green). The substrate leucine is shown in spheres, the Van der Waals radii of the residues sidechains that contact the bound leucine (highlighted in yellow in panel **A**) are rendered as a dotted surface.

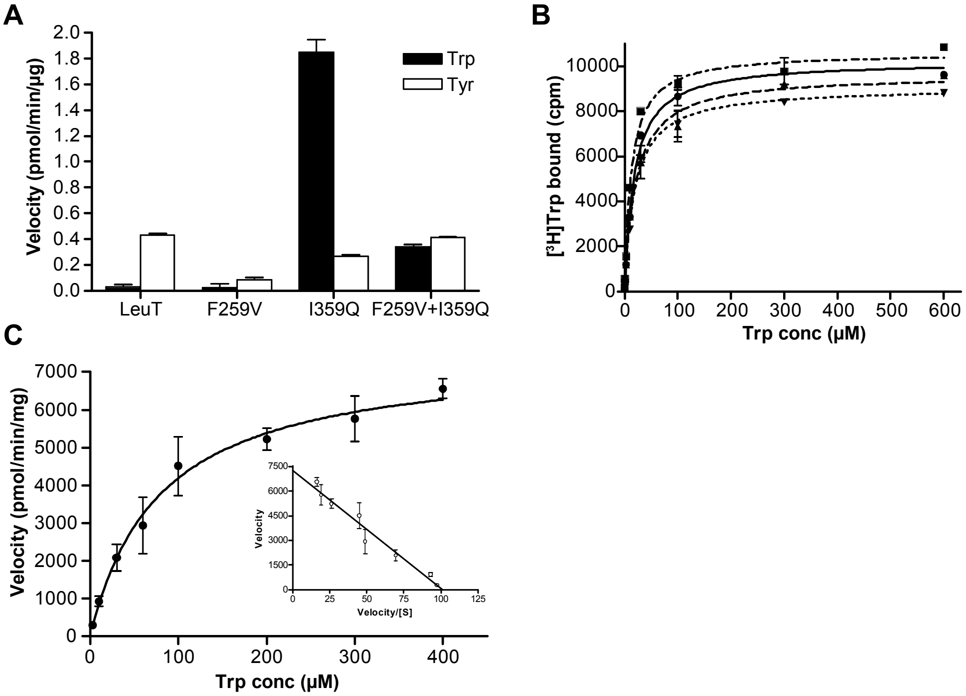

Figure 4.2. (**A**) Initial rate of [3H]Tyr or [3H]Trp uptake by LeuT and binding site variants. Error bars indicate s.e.m., n=2-5. (**B**) Saturation binding of [3H]Trp to LeuT and variants measured by scintillation proximity assay. LeuT: circles with solid line, F259V: triangles with dashed line, I359Q: inverted triangles with dotted line, F259V+I359Q: squares with dash-dot line. Error bars indicate s.e.m., n=2. (**C**) Steady-state kinetic measurement of [3H]Trp uptake by LeuT^{I359Q} fitted with Michaelis-Menten rectangular hyperbola. Inset is the Eadie-Hofstee transformation with linear regression. Error bars represent s.e.m., n=3.

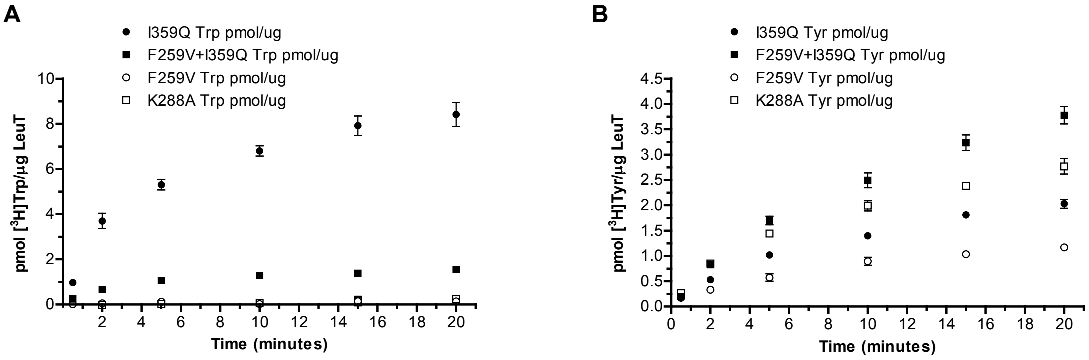

Figure 4.3. Time course of uptake for (**A**) [^{3}H]tryptophan and (**B**) [^{3}H]tyrosine.

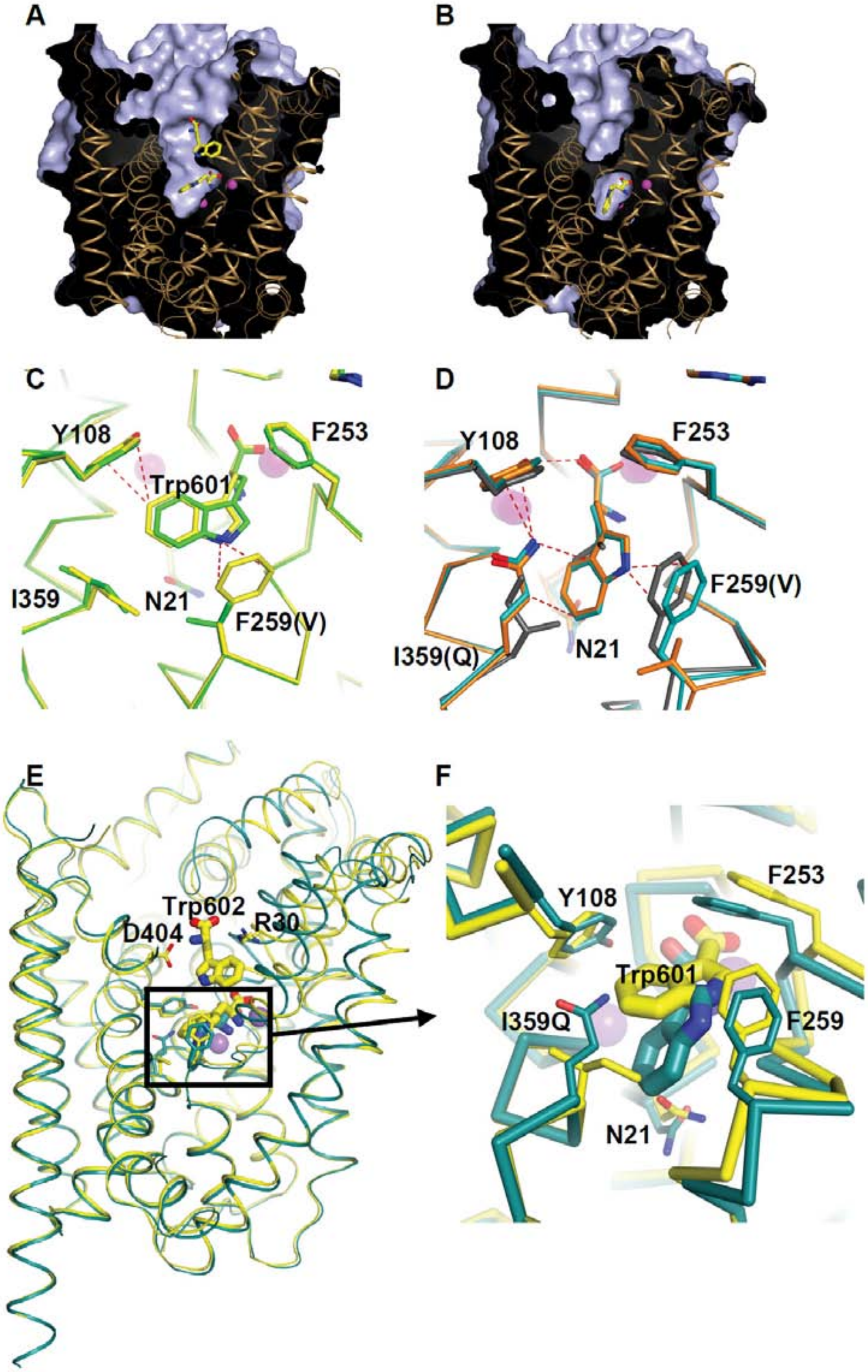
A
B
C
Y108
F253
Trp601
I359
N21
F259(V)
D
Y108
F253
F259(V)
I359(Q)
N21
E
Trp602
D404
R30
F
Y108
F253
Trp601
I359Q
F259
N21

Figure 4.4. (**A**) and (**B**) Cross-sections of the crystal structures of (**A**) LeuT^{F259V}-Trp in the open-to-out conformation and (**B**) LeuT^{I359Q}-Trp in the occluded conformation, showing solvent accessible surface area (blue). Bound tryptophan molecules are shown as yellow sticks, sodium ions are depicted as magenta spheres. (**C**) Overlay of the LeuT^{F259V}-Trp (green) and the wildtype LeuT-Trp (PDB id 3F3A, yellow) crystal structures showing details of tryptophan bound in the central binding site. (**D**) Overlay of LeuT^{I359Q}-Trp (teal), LeuT$^{F259V+I359Q}$-Trp (orange), and wildtype LeuT-Leu (PDB id 2A65, gray) crystal structures, showing details of the substrate binding site. (**E**) and (**F**) Overlay of the LeuT^{I359Q}-Trp (teal) and wildtype LeuT-Trp (yellow) crystal structures. Panel **E** shows a zoomed-out view of the transporters, parallel to the membrane plane. Panel **F** is a close-up view of the central binding sites showing the details of how tryptophan is differently accommodated in the wildtype and I359Q mutant LeuT structures.

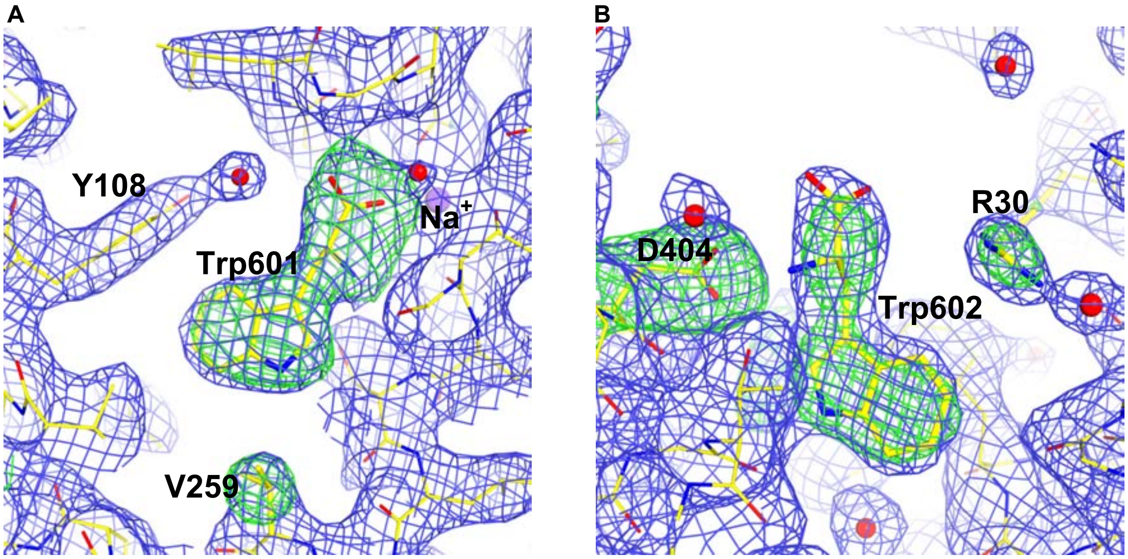

Figure 4.5. LeuT^{F259V}-Trp electron density kicked omit maps, omitting Trp601, Trp602, R30, D404, and V259 from the map calculations. 2mFo-DFc map, contoured at 1σ shown as blue mesh. mFo-DFc map, contoured at 3σ shown as green mesh. Red spheres indicate explicitly modeled water oxygen atoms. (**A**) Density in the primary binding site region. (**B**) Density in the extracellular gate region, showing the Trp602 binding site.

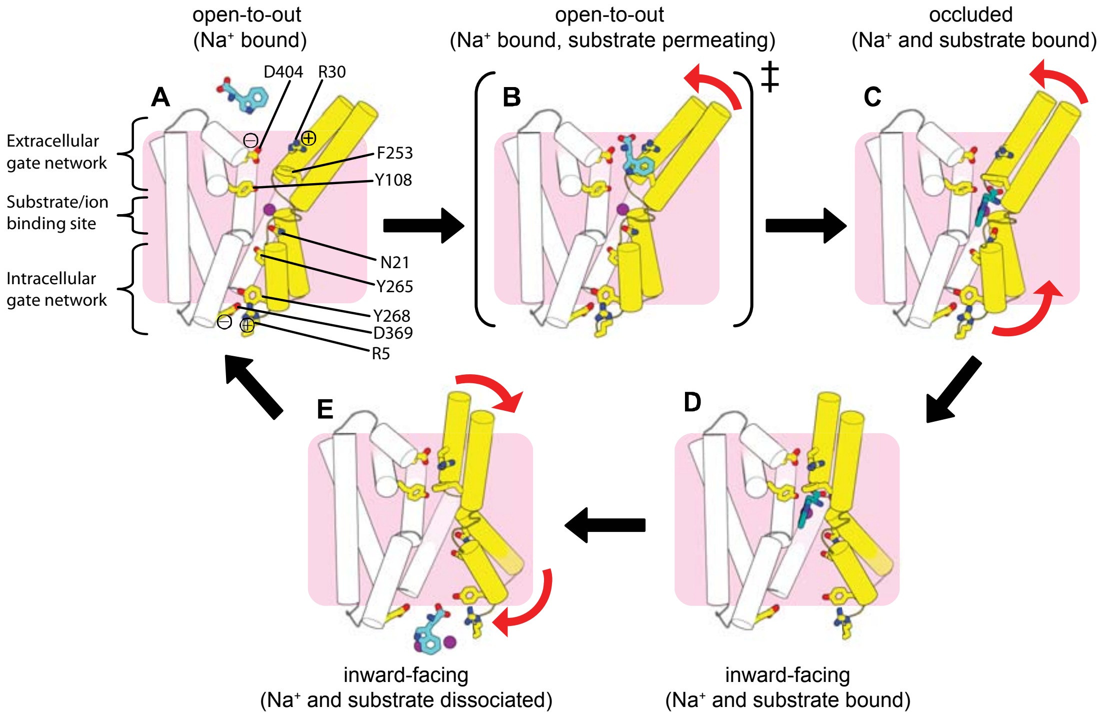

Figure 4.6. Mechanism of substrate permeation and conformational changes of the LeuT transport cycle. Core helices of LeuT are shown with TMs 3 and 10 truncated for clarity. TMs 1 and 6 are colored yellow. Select residues that are observed to interact with substrate during permeation and/or are known conserved functional elements are labeled and shown as sticks. Tryptophan, colored cyan, is shown as the permeating substrate, with Na$^+$ indicated by purple spheres. Red arrows indicate the direction of TM helix movement required to progress to the succeeding state. (**A**) Na$^+$-bound open-to-out state, modeled on the open-to-out conformation of the wildtype LeuT-tryptophan structure (PDB id 3F3A). (**B**) Na$^+$-bound open-to-out state with substrate bound between extracellular gate residues R30 and D404, proposed to be a transient state (indicated by double-dagger symbol) along the transport cycle. (**C**) Na$^+$ and tryptophan bound occluded intermediate state, based on the LeuT^{I359Q}-Trp structure. (**D**) and (**E**) Putative inward-facing conformation to illustrate opening of the intracellular gate preceding inward Na$^+$ and substrate release. (**D**) Na$^+$ and tryptophan bound inward-facing state. (**E**) Inward-facing state with Na$^+$ and substrate dissociated (apo state).

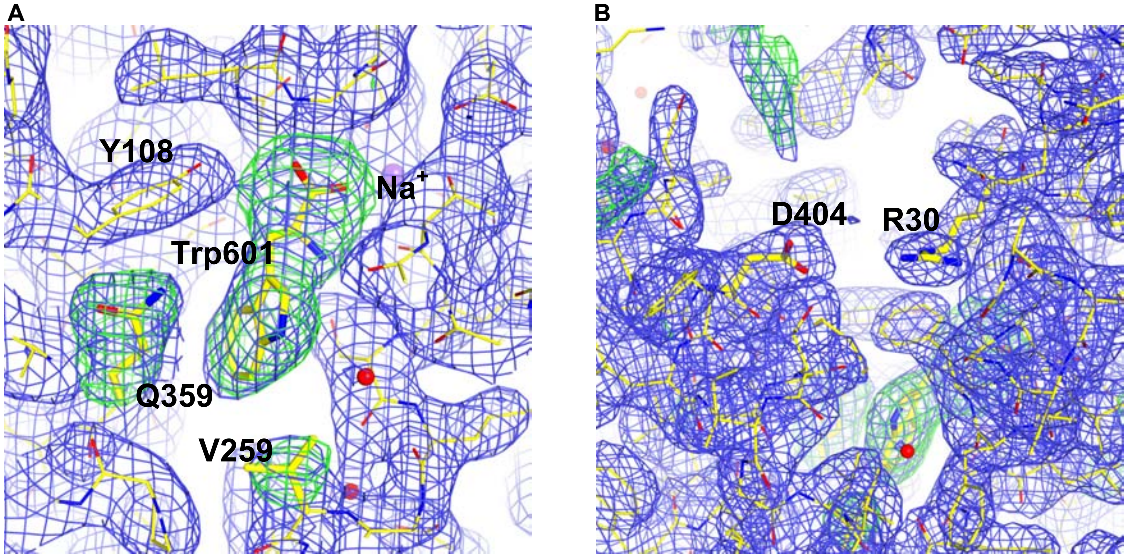

Figure 4.7. LeuT^{F259VI359Q}-Trp electron density kicked omit maps, omitting Trp601, V259 and Q359 from the map calculations. 2mFo-DFc map, contoured at 1σ shown as blue mesh. mFo-DFc map, contoured at 3σ shown as green mesh. Red spheres indicate explicitly modeled water oxygen atoms. (**A**) Density in the primary binding site region. (**B**) Density in the extracellular gate region.

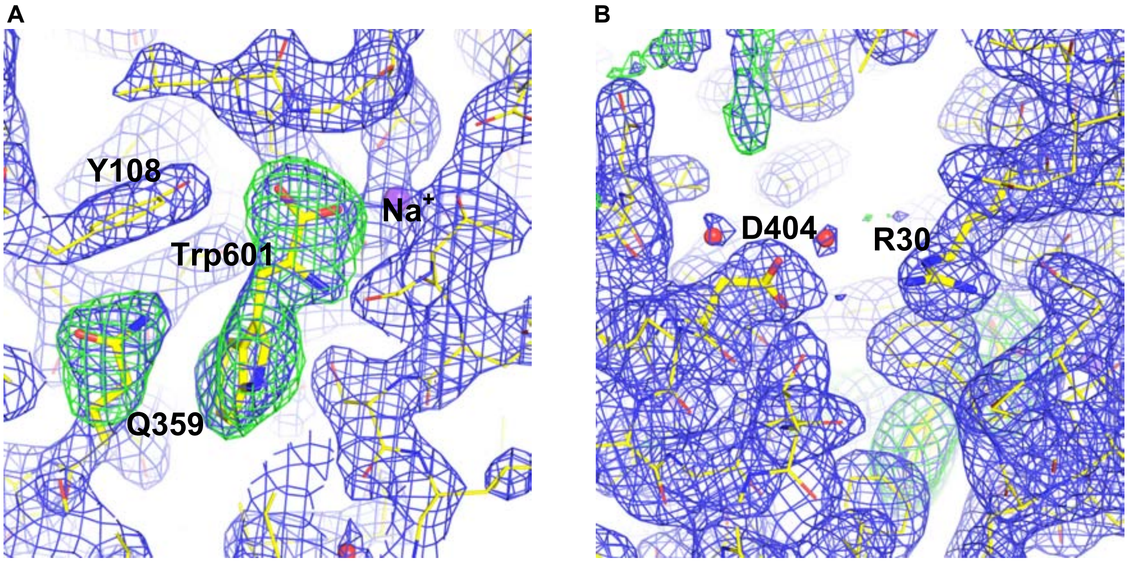

Figure 4.8. LeuT^{I359Q}-Trp electron density kicked omit maps, omitting Trp601 and Q359 from the map calculations. 2mFo-DFc map, contoured at 2σ in (**A**) or 1σ in (**B**), shown as blue mesh. mFo-DFc map, contoured at 4σ in (**A**) or 3σ in (**B**), shown as green mesh. Red spheres indicate explicitly modeled water oxygen atoms. (**A**) Density in the primary binding site region. (**B**) Density in the extracellular gate region.

Chapter 5

Architectures and Archetypes of Sodium-Coupled Neurotransmitter Transporters: A Review of the Structural Principles of Transport

The contents of this chapter are published in modified form:

Krishnamurthy, H., Piscitelli, C.L., Gouaux, E. (2009) Unlocking the molecular secrets of sodium-coupled transporters. *Nature* 459(7254) 347-355

Author contributions: All authors contributed equally to the preparation of the manuscript.

Abstract

Transmembrane sodium ion gradients provide energy that can be harnessed by so-called ‘secondary transporters’ to drive the translocation of solute molecules into a cell. Decades of intense study has proven the central role that sodium-coupled transporters play in many physiological processes, making them vital targets to treat many serious diseases. Within the last year, several sodium-coupled transporter crystal structures have been reported from different families, showing a remarkable structural conservation between functionally unrelated transporters. In this review we discuss these atomic resolution structures and how they illuminate the mechanistic principles of sodium-coupled transport of solutes across cellular membranes.

Introduction

Nature has evolved a multitude of greasy, transmembrane transporter proteins to catalyze the movement of polar or charged small molecules across the ~30 Å thick hydrophobic barrier of the membrane bilayer [177]. A large class of these proteins, deemed secondary transporters, can couple the selective discharge of an ionic gradient to power the "uphill" translocation of solute molecules across membranes. By coupling solute movement to ion co-transport, secondary transporters can concentrate solutes across a membrane by as much as 10^6-fold [111], and can accelerate solute flux by as much as 10^5-fold [178, 179] over simple passive diffusion.

Secondary transporters are present in all species throughout the kingdoms of life [153]. In humans, secondary transporters participate in diverse physiological processes, from the uptake of nutrients in the intestine [24], to the transport of Na^+ and Cl^- in the kidney [180], and the removal of neurotransmitters from the synaptic cleft [181]. Consequently, secondary transporters are the target of multiple therapeutic agents that include thiazide diuretics that inhibit a Na^+/Cl^- symporter in the distal convoluted tubule of the kidney [182] and selective serotonin reuptake inhibitors (antidepressants) that block activity of the serotonin transporter [183].

At the level of primary structure, amino acid sequence analysis suggests that there are over 100 distinct families of secondary transporters [Transport Commission (TC) system] [184], with over 40 families identified in humans alone [Solute Carrier (SLC) system]. With respect to biological function, these amino acid sequences encode uniporters, symporters, and antiporters that act on a myriad of substrates ranging from elemental cations and anions to aromatic neurotransmitters, nutrients, or even di- and tri-peptides [10, 11]. Transport is most commonly driven by proton or sodium transmembrane gradients, but other ionic gradients such as potassium, calcium, or chloride can also be utilized [10, 185].

In this review, we focus on transporters that are coupled to the sodium ion for their function. Our discussion employs the recent crystallographic advances in sodium coupled transporters to address questions pertaining to substrate-ion coupling, conformational states of the transport cycle, mechanisms of inhibition, and how the permeation pathway is alternately gated to maintain a tightly coupled transport mechanism.

Alternating access mechanism and internal symmetry

The mechanism by which secondary transporters couple the chemical potential of an ionic gradient to the translocation of solute has been considered for decades. Peter Mitchell provided early insights into the mechanism of secondary transporters by suggesting that they occupy two alternating structural states: one where the substrate binding pocket is accessible to extracellular solution (open-to-out) and another where the binding pocket is accessible to the cytoplasm (open-to-in) [5]. In this simple model, the concept of coupled transport (e.g. symport) could be understood by the positive coupling in the binding of substrate and ion to the open-to-out state, followed by isomerization of the transporter to the open-to-in state, allowing release of substrate and ion to the cytoplasm [6]. Through the late 1950s and the 1960s the basic idea of a two state alternating access mechanism was recast in a number of forms, from the 'gate type non-carrier' mechanism of Patlak

[7], to the two state 'allosteric model' of Vidaver [8],and the 'alternating access' model of Jardetzky [4].

Molecular mechanisms of secondary transporters based on atomic structures did not emerge until almost 40 years later, largely due to the fact that these transporters are hydrophobic and dynamic proteins that are difficult to crystallize. In 2002, the first crystal structure of a secondary transporter, the proton-driven multi-drug efflux pump AcrB of the resistance nodulation cell division (RND) family from *Escherichia coli* was reported [186]. Shortly thereafter, in 2003, the crystal structures of two major facilitator superfamily (MFS) transporters were solved: the glycerol-3-phosphate/phosphate antiporter GlpT [187] and the proton-coupled lactose symporter LacY [188]. Despite the markedly different fold of AcrB compared to the MFS transporters, each of these structures revealed internal 2-fold structural pseudo-symmetry that relates the N-terminal half of the transporter to the C-terminal half by an axis running through the center of the transporter, approximately perpendicular to the membrane. Furthermore, the inward-facing conformations adopted by GlpT and LacY suggested a mechanism of transport that involves a 'rocker-switch type' motion of the two symmetry-related halves, alternately opening and closing 'gates' to the extracellular and intracellular solutions.

The first atomic resolution structural insights into the mechanisms of sodium-coupled secondary transporters were reported in 2004 and 2005 with the structures of the aspartate transporter $\mathrm{Glt}_{\mathrm{Ph}}$ [109] (Dicarboxylate/Amino Acid:Cation Symporter; DAACS family), followed by the Na^+/H^+ antiporter NhaA from *E. coli.* [189] and the bacterial leucine transporter LeuT [59] (Neurotransmitter:Sodium Symporter; NSS family). The structures of GltPh, NhaA, and LeuT not only revealed unique membrane protein folds, but they also underscored the theme of internal 2-fold structural symmetry and discontinuous transmembrane helices [70].

$\mathrm{Glt_{Ph}}$, which assembles as a homotrimer, displays a pseudo 2-fold symmetrical relationship between crucial elements of the protomer architecture that includes 2 re-entrant hairpin loops (HP1, HP2), together with TM7a and the first half of TM8 [109]. The relevance of the 2-fold axis to transporter mechanism is particularly striking and it immediately suggests that HP1 and HP2 may undergo alternating, symmetry-related motions that open and close access to the substrate and ion binding sites (**Figure 5.1**) [109] .

In LeuT, which has a different fold from $\mathrm{Glt_{Ph}}$, an internal 2-fold pseudo-symmetry axis, running parallel to the membrane plane through the center of the transporter relates the first 5 transmembrane helices (TMs 1-5) to the second 5 helices (TMs 6-10) by ~180^{o} rotation [59] (**Figure 5.2**). Surprisingly, the same fold as LeuT was observed in the subsequently reported structure of the galactose transporter, vSGLT (Solute:Sodium Symporter; SSS family) [25], and in the benzyl-hydantoin transporter Mhp1 (Nucleobase:Cation Symporter; NCS1 family) [148], transporters that are unrelated in amino acid sequence to LeuT. Both vSGLT [25] and Mhp1 [148] contain the 5+5 inverted structural symmetry motif defined by TMs 1-10 of LeuT even though these three transporters share neither significant amino acid sequence identity nor the same number of TM segments. In vSGLT, with 14 TM helices compared to the 12 for LeuT and Mph1, there is an amino terminal TM helix preceding the 5+5 helix repeat and 3 additional helices following the repeat. That different transporters have the same common helix core yet have additional TM segments on the periphery supports the idea that the 2-fold-related 5+5 TM repeat defines the fundamental machinery of these transporters.

Not only have the structure determinations of vSGLT, LeuT, and Mhp1 effectively 'collapsed' the SSS [24], NSS [113] and NCS1 transporter families into one structural group (**Box 5.1**), they also foreshadow the likelihood that other secondary transporters, previously believed to belong to distinct families, may also have LeuT-like folds. The similarity in architecture between LeuT, vSGLT, and Mhp1 further implies commonalities in mechanism, ranging from principles of substrate and ion binding and specificity to conformational changes associated with transport. Atomic models of these functionally disparate yet structurally related transporter families has provided insight into the principles of sodium-coupled transport, and is beginning to clarify an alternating access mechanism that is distinctly different from the MFS family. **Box 5.1** outlines the three known structural folds of sodium-coupled transporters and the members from each family whose crystal structures have been solved. Each fold is named based upon the first transporter structure solved for that fold. Representative homologs in each family are also listed for reference. As highlighted in this review, despite being structurally unrelated, the concept of 'gates' and how they might function in the alternate access mechanism has many similarities for transporters with LeuT- and $\mathrm{Glt_{Ph}}$-folds.

Central pathway inside a scaffold

Inspection of LeuT, vSGLT, and Mhp1 structures show that the 5+5 TM motif consists of two interior pairs of symmetry-related helices, TMs 1, 6, and 3, 8, which are nested within an outer ring of helices, TMs 2, 4, 5, 7, 9, and 10 (LeuT numbering). Consistent with mutagenesis and functional studies [190-193], these interior pairs largely define the central translocation pathway that contains the binding sites for substrate and ions. The three transporter structures show that the substrate binding site lies in the center of these interior pairs, and is coincident with the internal 2-fold symmetry axis (**Figures 5.1, 5.2, and 5.3**).

Among the outer ring of helices, symmetry-related TMs 4, 5 and 9, 10 form inverted V-shaped 'pincers' that cradle the interior TM 3, 8 pair, whereas TMs 2 and 7, also related by the 2-fold axis of symmetry, link TMs 1 and 6 with the intracellular and extracellular helix-loop-helix structures, IL1 and EL4. We suggest that the outer ring of helices, which nestle the interior pairs, provides a framework to stabilize the transporter within the lipid membrane and couples conformational changes occurring on one side of the membrane to movements on the other side.

The notion of a central translocation pathway that is surrounded by a protein scaffold is also observed in the Glt$_{Ph}$-fold (**Figure 5.1**). In Glt$_{Ph}$, the transport machinery of HP1, HP2, TM7 and TM8, forming a C-terminal domain, is enveloped by a ring of 6 TM helices from the N-terminal domain of the transporter. In this case, the crucial role of the C-terminal domain in defining the transport pathway was suggested by studies showing that functionally important residues were localized to the C-terminus and that the C-terminal domain was more highly conserved than the N-terminal domain [194-196]. For Glt$_{Ph}$ and its orthologs, the scaffold of TMs 1-6 not only supports elements of the transport pathway, but it also mediates essential intersubunit contacts in the trimer.

Substrate and ion binding sites

A single substrate binding site was identified in LeuT, at the center of the transporter, surrounded by the interior helices, TMs 1, 3, 6, and 8 [59]. The binding sites for galactose in vSGLT [25] and benzyl-hydantoin in Mhp1 [148] are also similarly located (**Figure 5.3A**). Directly adjacent to the primary binding site, TMs 1 and 6 (LeuT and Mhp1) or TMs 2 and 7 (vSGLT) have interruptions in their helical conformations, a structural feature encountered in other membrane proteins of ion-transport function [189, 197, 198]. The interruption in the α-helical structures in the proximity of the binding site exposes main-chain hydrogen-bonding partners and orients the helical dipoles to create a polar environment for coordinating substrate and ions within the lipid bilayer [59]. These electrostatic elements combined with specific side chains that alter the volume and shape of the binding pocket provide selectivity of these transporters for a substrate based on its size, polarity, and charge [75].

Recent experimental ligand binding experiments and steered molecular dynamics simulations (SMD) of LeuT have suggested that there is an additional 'secondary' binding site between the primary site and bulk extracellular solution located near R30 and D404 [95, 106]. Shi and colleagues [95] proposed that the simultaneous occupancy of this secondary site triggers the intracellular release of substrate and sodium from the primary site. X-ray diffraction studies of LeuT, by contrast, do not show binding of either the substrate leucine or the substrate analog selenomethionine anywhere other than the primary binding site [75]. However, LeuT complexed with tryptophan, which locks the transporter in an open-to-out conformation, does bind a second tryptophan molecule (Trp 602) between R30 and D404 [75] (**Figure 5.3B**). Because binding at this site is observed when the transporter is trapped in an open-to-out state, we suggest that this site serves as a transiently occupied site as substrates move from the extracellular vestibule to the primary binding site.

The high resolution structure of LeuT also identified the presence of two Na^+ ions, Na1 and Na2 [59]. The Na1 ion is octahedrally coordinated by five protein ligands and the carboxylate of the substrate leucine (**Figure 5.3C**), demonstrating that ion and substrate binding are directly coupled. By contrast, the Na2 ion is located ~6 Å away from the substrate in LeuT and is bound via a trigonal bipyramidal coordination geometry (**Figure 5.3D**). Intriguingly, by structural comparison, a sodium-ion binding site similar to the site occupied by the Na2 ion in LeuT was identified in both vSGLT and Mhp1, positioned about 10 Å away from the substrates [25, 148]. Although the resolutions of the vSGLT and Mhp1 structures are not sufficient to unambiguously assign a sodium ion to the site occupied by the Na2 ion, a sodium ion at this position in vSGLT is supported by biochemical and mutagenesis studies on vSGLT and other SSS family members, including the sodium/iodide symporter [25, 199, 200]. These observations indicate a role for a Na2-like ion not only in substrate binding but also in conformational changes associated with substrate transport. Studies on GAT-1 [201] as well as molecular dynamic and free-energy simulations of LeuT [105] implicates the site occupied by the Na2 ion as a low affinity site that can readily give up its ion to the bulk phase, thus promoting release of the substrate [104].

Sodium-to-substrate stoichiometry not only varies between sodium-coupled transporters but also amongst members of the same family, depending on the thermodynamic driving force required for substrate uptake [179]. The requirement for transport varies from 1 to 3 sodium ions per substrate in the NSS [111, 202-204] and SSS families [200, 205-207] (**Box 5.1**). Because vSGLT and Mhp1 probably have a sodium ion binding site similar to that occupied by the LeuT Na2 ion, we suggest that it is a common ion site for divergent transporters and is essential for coupled substrate binding and symport. Though the ion site for Na1 is less conserved among these transporters from different families, for members of the NSS family the Na1 ion not only enhances substrate binding, but it also provides favorable interactions with the co-transported chloride ion [73, 74]. Even though some LeuT orthologs couple substrate transport to 3 sodium ions, there is no direct experimental determination of a third sodium ion binding site [179].

Conformational states

Crystal structures of LeuT [59, 75, 76], Mhp1 [148], vSGLT [25], and $\mathrm{Glt_{Ph}}$ [108, 109] provide evidence for the conformations sampled by sodium coupled secondary transporters as they proceed through the transport cycle. These structures support a mechanism of transport (**Figure 5.4A**) where an outward-facing conformation of the transporter ($\mathbf{T^{out}}$) binds substrate and ions and subsequently isomerizes to an inward-facing conformation ($\mathbf{T^{in}}$) via substrate-and-ion bound Michaelis-like intermediates ($\mathbf{T^{M}S^{in}}$ and $\mathbf{T^{M}S^{out}}$). After the release of substrate and ion(s), the $\mathbf{T^{in}}$ state recycles 'back' to the $\mathbf{T^{out}}$ state either in the apo form, or through a potassium bound state (as is the case for glutamate [208] and serotonin transporters [209]), or back through a $\mathbf{T^{M}S}$ state, i.e. substrate exchange.

A common and striking observation from the crystallographic studies reviewed here is the presence of a stable occluded state for the substrate-ion bound ternary complex of each of the four transporters (**Figure 5.4A**). This state is characterized by the bound substrate residing in a closed or partially occluded binding pocket, where dissociation from the pocket would require a conformational change. Despite the common steric occlusion of substrate, the degree to which the four transporters block solvent accessibility to the binding pocket from the extracellular and cytoplasmic sides varies (**Figure 5.4A**).

In the substrate-bound state of Mhp1 and LeuT (**Figure 5.4A**), the occluded state occupies an outward-facing conformation ($\mathbf{T^{M}S^{out}}$), where the extracellular pathway is kept open to solvent. In LeuT, the extracellular solvent-exposed region is formed by a large hydrophobic vestibule. At the base of this vestibule are two highly conserved residues, Y108 and F253, that close the top of the binding pocket, forming the occluded substrate binding pocket. In Mhp1, the structural elements that occlude the substrate benzyl-hydantoin are different from LeuT and involve the N-terminal half of TM10. Glt$_{Ph}$ also displays an outward-facing occluded conformation (**Figure 5.4A**). Aspartate is bound between the tips of the HP1 and HP2 loops, which are closed over the binding site like lids, preventing the dissociation of substrate to either side of the transporter.

In contrast to LeuT and Mhp1, the occluded state of vSGLT adopts an inward-facing conformation (**T^MS^{in}**), exposing a region to intracellular solution (**Figure 5.4A**) that is consistent with accessibility studies carried out on PutP [199] and SERT [72, 210-212], vSGLT and LeuT orthologs, respectively. Akin to leucine binding in LeuT, galactose is bound to vSGLT in a central binding pocket located above the intracellular vestibule, and is occluded from the vestibule by a conserved aromatic residue, Y263. Even though the inward-facing, occluded conformation of galactose-bound vSGLT is fundamentally different from that observed for substrate-bound LeuT or Mhp1, there is a simple relationship between the two distinct states: the outward- and inward-facing states are related by the common 2-fold axis of internal symmetry that relates the 5+5 TM repeats, thus suggesting a symmetrical relationship between the **T^MS^{in}** and **T^MS^{out}** states.

The crystal structure of Mhp1 in the unliganded form shows an open-to-out conformation representing the **T^{out}** state of the transport cycle (**Figure 5.4A**). Comparison of the ligand-bound occluded form of Mhp1 with the apo open-to-out state shows that the N-terminal half of TM10 bends inward in response to ligand binding to form the occluded state. Further insight into the conformation of the **T^{out}** state is provided by crystal structures of LeuT and Glt_{Ph} bound to competitive inhibitors that trap open-to-out conformations of the transporters [75, 108] (**Figure 5.4B**).

Mechanisms of inhibition

Crystal structures of LeuT bound to both competitive and non-competitive inhibitors have afforded us a glimpse into the mechanisms of inhibition for NSS family transporters. In 2007, crystal structures of LeuT bound to the tricyclic antidepressants (TCAs) clomipramine, desipramine, and imipramine were reported [76, 77]. Therapeutically, these molecules are competitive inhibitors of the human serotonin transporter [128] and block re-uptake of serotonin from synapses, thereby prolonging activation of the serotonin receptor. For LeuT, however, the mechanism of inhibition by TCAs is purely non-competitive [76]. The structures of the LeuT-TCA complexes reveal that the TCA molecule binds in the outward-facing vestibule, a partially hydrophobic cavity that binds other non polar molecules, including *n*-octyl-β-D-glucopyranoside [75]. The TCA is situated directly above the R30-D404 salt bridge, where the guanidinium head group of the arginine has flipped to form a direct salt bridge with the aspartate, stabilizing the occluded state of LeuT (**T^{M}SI**) (**Figure 5.4B**), and preventing further conformational changes necessary to progress around the transport cycle. The identification of this inhibitory allosteric site is consistent with a general mechanism of non-competitive inhibition, where the substrate binding site and inhibitor site do not overlap, and thereby trap the transporter in an inactive state. Though the non-competitive mechanism for TCA inhibition of LeuT is different from the competitive mechanism for TCA inhibition of SERT [128], the structural principles revealed by the LeuT-TCA complexes define a paradigm for allosteric inhibition of NSS family transporters and, by extension, for other transporters with the LeuT-fold.

The structural basis for competitive inhibition was recently revealed by the crystal structure of LeuT bound to tryptophan [75]. Tryptophan acts like a strut between TMs 1/6 and TMs 3/8/10 where the bulky indole ring is wedged into the binding pocket and, in so doing, displaces the α-amino and α-carboxylate moieties outward by ~2 Å compared to their positions in the leucine-bound occluded state. With insufficient space to fully accommodate the indole ring in the substrate binding pocket, the transporter is effectively propped open through interactions of the inhibitor's α -substituents with TMs 1b and 6a and the indole ring with TMs 3, 8, and 10. The transporter is thus locked open (**T^{out}I, Figure 5.4B**) and thereby blocked from progressing to the occluded **$T^{M}S^{out}$** state of the transport cycle.

The crystal structure of $\mathrm{Glt_{Ph}}$ bound to the competitive inhibitor TBOA, a bulky aspartate analog, underscores a similar principle of competitive inhibition for transporters with the $\mathrm{Glt_{Ph}}$-fold (**Figure 5.4B**) [108]. In this structure the aspartate group of TBOA binds similarly to the substrate L-aspartate, lodged between TM7, TM8 and HP1. The large benzyl moiety of TBOA, however, sticks out toward HP2, propping HP2 in an open conformation (**Figure 5.4B**), disrupting sodium site 2 and precluding the formation of the occluded state.

The observation of bulky substrate analogs as competitive inhibitors of transport that stabilize an opening of the extracellular side of the transporter is also supported by SCAM assays for the eukaryotic SLC6 homolog GAT-1, as well as the human glucose transporter hSGLT of the SLC5 family [147]. The consistency of these results with the LeuT-Trp crystal structure suggests that the mechanism of inhibition is likely to be similar for other sodium-coupled transporters that share the LeuT-fold, and that a comparable principle seems to be found in other families of structurally disparate transporters, such as those adopting the $\mathrm{Glt_{Ph}}$-fold.

Permeation pathways and gating mechanisms

In transporters with Glt$_{\mathrm{Ph}}$-fold (Glt$_{\mathrm{Ph}}$) and LeuT-fold (LeuT, vSGLT, and Mhp1), the primary substrate and ion binding sites are flanked by two gates, one controlling access to the outside of the cell and the other controlling access to the inside. To allow substrates and ions to reach the primary binding sites yet not open up a continuous transmembrane pore, only one gate can open at a time. Thus, understanding how secondary transporters 'work' is fundamentally a question of how the gates work, i.e. what are the principles governing the coordinated alternate opening and closing of extracellular and intracellular gates upon substrate binding from the outside and unbinding from the inside. To answer this question, we consider the conformational changes that occur during transport and the likely pathways that substrates and ions take upon binding and unbinding from their central primary sites.

Inspection of the small group of sodium-coupled transporter structures suggests that for a given transporter trapped in a specific state, the gates that control access to and from the primary binding site are often asymmetric, i.e. the extracellular gate is less substantial or 'thinner' and the cytoplasmic gate is more substantial or 'thicker', and *vice versa* (**Figure 5.4A**). This is observed for transporters with the Glt$_{\mathrm{Ph}}$- as well as the LeuT-fold. For example, in the outward-facing occluded leucine-bound LeuT complex, only a few residues directly block access from the primary binding site (Y108, F253), forming a ‘thin’ gate at the base of a solvent-filled cavity to the outside, whereas the cytoplasmic ‘thick’ gate is made up of ~20 Å of packed protein that includes TMs 1a, 3, 6b, 8 and 10, in combination with the amino terminus and IL1 (**Figure 5.5A, C, E**). Similarly, in the substrate-bound state of Glt_{Ph} we find that the extracellular gate is made up of a few residues at the tip of HP2 whereas the cytoplasmic gate is composed of a ~15 Å slab of helices and side chains (HP1, TM7a and TM8).

The substrate-and-ion bound inward-facing occluded state of vSGLT presents the converse situation, with a 'thick' extracellular gate formed by TMs 1b, 3, 6a, 10 and EL4 (LeuT numbering) and a 'thin' cytoplasmic gate defined by Y262, Y263 and W264 (**Figure 5.5B, D, F**). Thus, the 'thin' gates are typically defined by the side chain atoms of a few residues whereas the 'thick' gates are formed by entire TM helices packing close together, in combination with extracellular and intracellular loops such as amino termini, IL1 or EL4 (LeuT numbering). Importantly, the extracellular and intracellular pathways defined by the open-to-out and outward-facing LeuT/Mhp1 and inward-facing vSGLT structures, are defined precisely by the symmetry-related components to the "thick" gate for each transporter. That is, in any one state, the location of the "thick" gate (either extracellular or intracellular) is reciprocal to the solvent-filled pathway, related fundamentally by the 2-fold axis of internal symmetry.

Instances where the same transporter was captured in different states of the transport cycle provide insight into how the thin gate opens and closes. The structures of LeuT, Mhp1, and Glt_{Ph} in open-to-out and in substrate-and-ion bound occluded states demonstrate that substrate and ion binding results in relatively small conformational changes. In Glt_{Ph}, for example, aspartate binding allows HP2 to close over the binding site, whereas TBOA binding holds it open, suggesting that the simple 'flipping' movement of HP2 primarily describes the thin gate motion that occludes the binding site during transport. With LeuT, in comparing the open-to-out conformation of the Trp complex with the occluded Leu-bound state, the most substantial change is the rotation of a subdomain of the transporter composed of TMs 1b, 2a, 6b, and EL4, which, together with rotations of several side chains, collectively move inward to close off the substrate binding site from extracellular solution. For Mhp1, the binding of substrate involves the inward bending of the N-terminal half of TM10. Thus, the thin gate opens and closes around the substrate binding pocket by movements localized to the side of the transporter from which substrate is binding or unbinding (i.e., transitions from $\mathbf{T^{out}}$ to $\mathbf{T^{M}S^{out}}$ or from $\mathbf{T^{M}S^{in}}$ to $\mathbf{T^{in}}$**)** .

In contrast to the local changes associated with substrate binding, the isomerization between the outward-facing ($\mathbf{T^{M}S^{out}}$) and inward-facing ($\mathbf{T^{M}S^{in}}$) states involves larger-scale conformational changes spread throughout the transporter. As first illustrated by Yamashita and colleagues [59], and further elaborated by Forrest et al. [72], one can conceptualize this conformational change by applying the 2-fold axis of internal pseudo-symmetry to the key TM segments 1 and 6. In so doing, one sees that because the conformation of TM1 and 6 deviate from the internal 2-fold axis, a rotation of ∼180° about the internal symmetry axis alternatively 'open' and 'closes' the extracellular and cytoplasmic gates. Forrest and colleagues suggest that the bundle of TMs 1, 2, 6 and 7 moves as a rigid body, in a rocker switch-like mechanism. This simplification, however, is not consistent with the structural comparison of the LeuT-Leu and LeuT-Trp complexes which indicate that there is some degree of independent movement within this bundle and thus further experimental and computational studies are required to validate this hypothesis.

Nevertheless, comparison of the LeuT-leucine (outward-facing, $\mathbf{T^{M}S^{out}}$) and vSGLT-galactose (inward-facing, $\mathbf{T^{M}S^{in}}$) structures suggests that the differences in these states can be described by a reorientation of TMs 1 and 6 (TMs 2 and 7 in vSGLT), together with movement and bending of TMs 2 and 7 (TMs 3 and 8 in vSGLT). In the outward-facing state, near the extracellular opening in LeuT, TM 1, for example, is about 17 Å and 18 Å away from TM3 and 10 respectively (**Figure 5.5A, C**) compared to ~ 7 Å and 5 Å for equivalent elements in vSGLT (**Figure 5.5B, D**). Similarly, the intracellular cavity is open in vSGLT by ~16 Å, measured between TMs 9 and 7 (**Figure 5.5B, F**), whereas the same elements in LeuT (TMs 6 and 8), with the 'thick' intracellular gate closed, are ~ 9 Å apart (**Figure 5.5A, E**). Thus, the similar magnitude to which the extracellular cavity of LeuT collapses to form the 'thick' gate seen in vSGLT and to which the 'thick' intracellular gate of LeuT opens to form the cavity in vSGLT supports the idea that the relationship between the cavities and 'thick' gates is reciprocally related by the 2-fold internal symmetry of the transporter, and that structures of LeuT and vSGLT largely represent distinct occluded-state ternary intermediates that interconvert during transport. The re-orientation of TMs 1, 2, 6, and 7 (LeuT numbering) between an occluded LeuT-like conformation ($\mathbf{T^{M}S^{out}}$) and an occluded vSGLT-like conformation ($\mathbf{T^{M}S^{in}}$) is therefore likely to approximate the conformational transition that re-orients the 'thin' gates of a transporter to the opposite side of the membrane. Additionally, flexing of TMs 3 and 8 may also contribute to opening and closing the gates, with these TMs bending at conserved glycine residues near their midsections and with IL1, EL4, and the amino terminus functioning as flexible 'flaps', helping to seal the gates in the closed states.

Taken together, the analyses described above from the available structures of the LeuT-fold, namely Mhp1, LeuT, and vSGLT, identify two major classes of transitions that occur during transport. First, substrate binding and unbinding closes and opens, respectively, the ‘thin’ gates to occlude or expose substrate in the primary binding site. Second, opening and closing of the ‘thick’ gates 'switch' the transporter from outward-facing to inward-facing states and vice versa. The opening and closing of the ‘thin’ gates stem from relatively local conformational changes, some of which involve helix rotations centered on axes passing through the regions of helical discontinuity. By contrast, the ‘thick’ gate transition reorients the occluded substrate-transporter complex by rotation of entire transmembrane-spanning bundle of helices about a central axis approximately perpendicular to the axis of internal 2-fold symmetry (**Figure 5.6A, B**). How do we know that comparing different transporters in different conformations reliably predicts common mechanistic principles? While there is, at present, no unambiguous answer to this question, the fact that transporters with the LeuT-fold share multiple common elements of structure and symmetry suggests that basic mechanistic principles are also likely common. Specific details, related to substrate and transporter interactions, as well as regulation, as examples, will likely differ, however.

What prevents both gates from opening simultaneously? We suggest that the discontinuous helical regions of TM1 and 6 provide a hinge around which a small degree of conformational change can occur. This is visualized in the movements that accompany binding of the competitive inhibitor, tryptophan to LeuT in which the ‘thin’ extracellular gate opens by outward movements of TMs1b and 6a. However, TMs 1 and 6 are also adjacent to TMs 2 and 7, which all together form a 4-helix bundle. Thus larger scale movement of TMs 1b and 6a are constrained by TMs 2 and 7, perhaps because the latter are continuous α-helices lacking the non helical, hinge-like regions present in TMs 1 and 6. Consequently, substantial outward (opening) movements of TMs 1b and 6a, or TMs 1a and 6b, are limited by TMs 2 and 7. Thus, while both gates may be closed at the same time, both gates are prevented from simultaneously opening by the conformational rigidity enforced by TMs 2 and 7.

Future Prospects

The recent crystallographic advances in sodium-coupled secondary transporters have greatly advanced our understanding of the structural principles that underlie transporter function. The consistency of these models with the decades of elegant functional studies has allowed us to associate specific conformations with different mechanistic states of the transport cycle. However, this mechanistic description is derived from a patchwork of different transporters fortuitously crystallized in different states. Therefore, an accurate description of the precise conformational changes that a given transporter undergoes during transport must await further structural, biophysical and computational studies of individual secondary transporters. Additionally, multiple questions regarding the fundamental nature of the transport cycle remain outstanding. Although it is straightforward to understand how substrate binding leads to closure of a 'thin' gate, what are the chemical and structural principles that drive isomerization of the transporter from outward-facing to inward-facing states, i.e. opening of the 'thick' gate? Unlike mechanical models of gating in primary transporters and in ion channels, in secondary transporters there is no apparent source of mechanical force to open the thick gate. What structural changes occur upon only the binding of ions? What is the sequence of events that leads to release of substrate on the cytoplasmic side? How do ions, such as potassium, catalyze the isomerization of glutamate and serotonin transporters from inward facing to outward facing states? Finally, in order to fully understand and appreciate the biological and pharmacological properties unique to the human transporters, crystal structures of eukaryotic homologs will have to be solved.

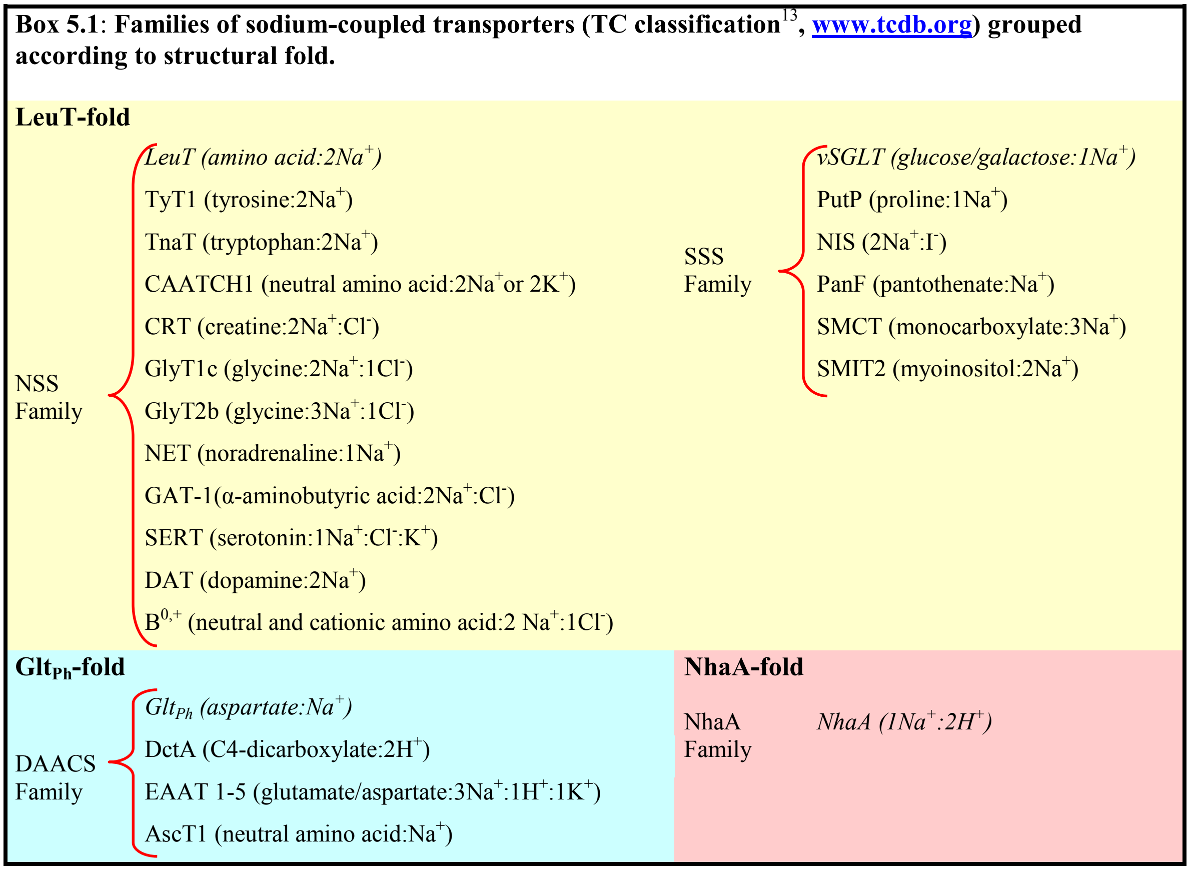

Box 5.1: **Families of sodium-coupled transporters (TC classification**[13]**, www.tcdb.org) grouped according to structural fold.**

LeuT-fold

NSS Family
- *LeuT (amino acid:$2Na^+$)*
- TyT1 (tyrosine:$2Na^+$)
- TnaT (tryptophan:$2Na^+$)
- CAATCH1 (neutral amino acid:$2Na^+$or $2K^+$)
- CRT (creatine:$2Na^+$:Cl^-)
- GlyT1c (glycine:$2Na^+$:$1Cl^-$)
- GlyT2b (glycine:$3Na^+$:$1Cl^-$)
- NET (noradrenaline:$1Na^+$)
- GAT-1(α-aminobutyric acid:$2Na^+$:Cl^-)
- SERT (serotonin:$1Na^+$:Cl^-:K^+)
- DAT (dopamine:$2Na^+$)
- $B^{0,+}$ (neutral and cationic amino acid:2 Na^+:$1Cl^-$)

SSS Family
- *vSGLT (glucose/galactose:$1Na^+$)*
- PutP (proline:$1Na^+$)
- NIS ($2Na^+$:I^-)
- PanF (pantothenate:Na^+)
- SMCT (monocarboxylate:$3Na^+$)
- SMIT2 (myoinositol:$2Na^+$)

Glt_{Ph}-fold

DAACS Family
- *Glt_{Ph} (aspartate:Na^+)*
- DctA (C4-dicarboxylate:$2H^+$)
- EAAT 1-5 (glutamate/aspartate:$3Na^+$:$1H^+$:$1K^+$)
- AscT1 (neutral amino acid:Na^+)

NhaA-fold

NhaA Family
- *NhaA ($1Na^+$:$2H^+$)*

Box 5.1. Families of sodium-coupled transporters (TC classification [11, 184], www.tcdb.org) grouped according to structural fold. NSS, SSS, and NCS1 families adhere to the LeuT-fold, while DAACS family adopts the Glt_{Ph}-fold, and NhaA family adopts the NhaA-fold. Representative transporters from each family are listed, and the ion stoichiometry is indicated when supported by biochemical data. Transporters whose crystal structures have been determined are italicized. Note that some of the transporters are thought to be H^+ rather than Na^+ dependent.

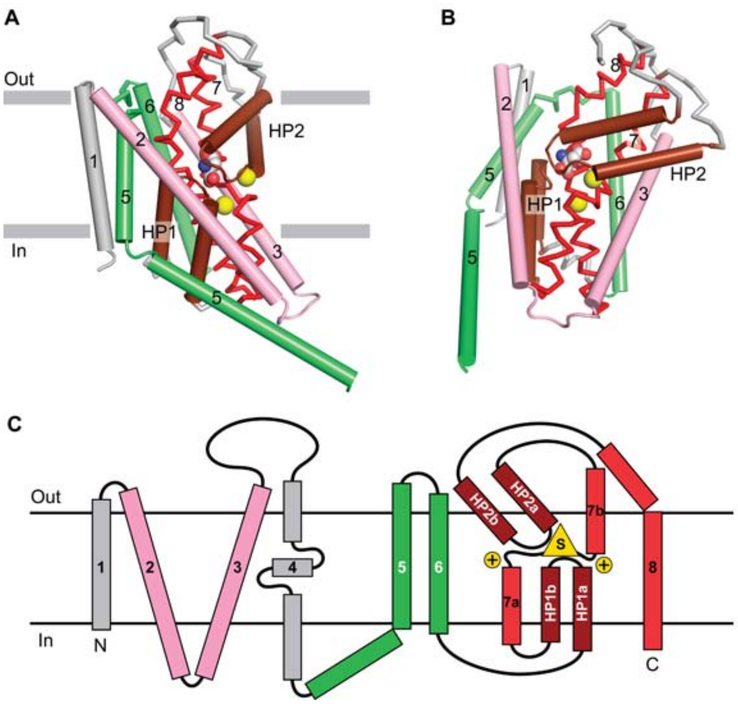

Figure 5.1. Architecture of the Glt$_{Ph}$ fold. (**A**) View of core transmembrane helices for Glt$_{Ph}$ illustrating how the first 6 transmembrane segments form a cradle harboring the elements of the transporter machinery. The functionally essential reentrant hairpin loops (HP1/HP2) are in brown, the partially unwound TM7 and the amphipathic TM8 are in red. View is parallel to the membrane and only one subunit of the Glt$_{Ph}$ trimer is shown. (**B**), Same elements as panel (**A**) viewed approximately perpendicular to the membrane. The bound substrate (carbon, gray; oxygen, red; nitrogen, blue) and sodium ions (yellow) are shown in CPK representation. (**C**) Topology diagram for Glt$_{Ph}$ with substrate and ions depicted as yellow triangle and circles, respectively.

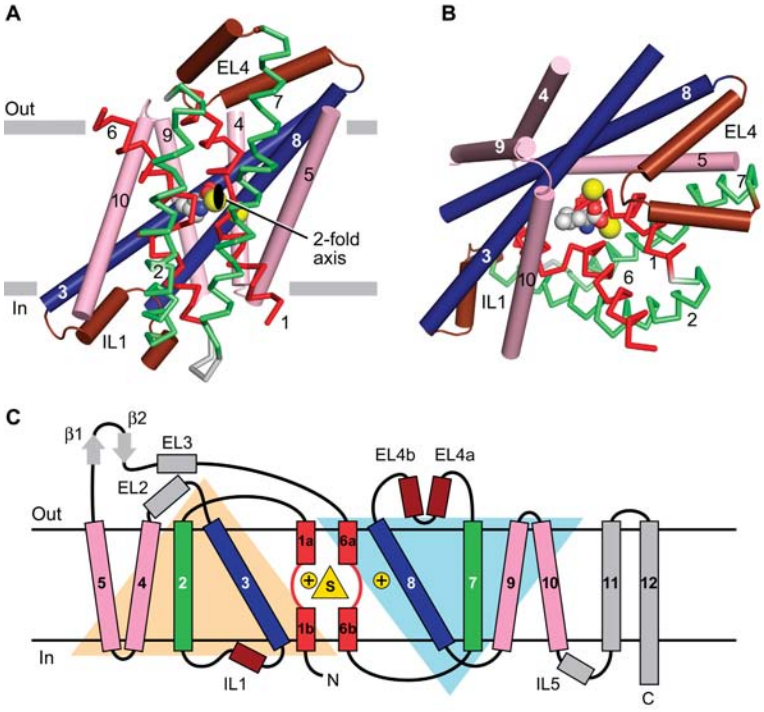

Figure 5.2. Architecture of the LeuT fold. (**A**) View of the core 5+5 repeat structure for LeuT showing the inverted scaffold of TMs 4/5 and 9/10 (pink) holding the long bracing helices (TMs3/8; blue) and the jointed, finger-like and partially unwound TM1/6 helices (red). Bracing TMs 1/6 are TMs 2/7 (green). Reentrant, pseudo 2-fold related loops that either partially (EL4) or fully (IL1) occluded central binding site are shown in brown. View is parallel to the membrane. (**B**) Same elements as in panel (**A**) viewed approximately perpendicular to the membrane. The bound substrate (carbon, gray; oxygen, red; nitrogen, blue) and sodium ions (yellow) are shown in CPK representation. (**C**) Topology diagram for LeuT with substrate and ions depicted as yellow triangle and circles, respectively.

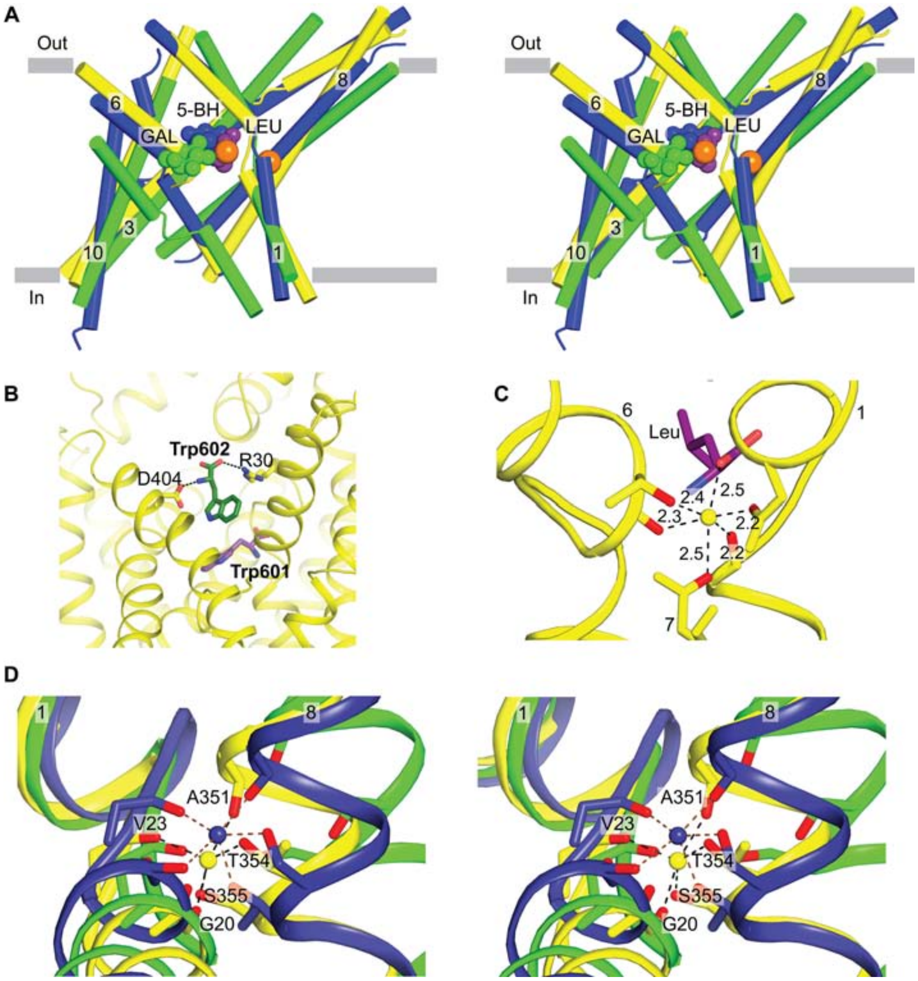
A
Out
6
5-BH
GAL
LEU
8
3
10
1
In
B
Trp602
R30
D404
Trp601
C
6
Leu
1
2.5
2.4
2.3
2.2
2.2
2.5
7
D
1
8
A351
V23
T354
S355
G20

Figure 5.3. Conserved substrate and ion binding sites in LeuT, vSGLT and Mph1. (A) Stereo diagram of the superpositioned occluded structures of LeuT (yellow), Mhp1 (blue), and vSGLT (green) showing the location of their primary substrate binding sites roughly in the middle of the membrane bilayer and close to the discontinuous regions of TMs 1 and 6. Substrates and LeuT Na ions (orange) are shown in CPK representation. For clarity, only TMs 1, 3, 6, 8, and 10 are shown. (**B**) View of the secondary binding site in LeuT. A second Trp molecule, Trp 602, is bound between R30 and D404 in the open-to-out conformation stabilized by Trp 601 in the primary binding site. (**C**) Na1 ion in LeuT is octahedrally coordinated by residues from TMs 1, 6, and 7 as well as bound leucine (purple). (**D**) Stereo representation of superpositioned LeuT (yellow), vSGLT (green), and Mhp1 (blue) structures shows the location of their Na2 sites. Na2 of LeuT and Mhp1 are shown as yellow and blue spheres, respectively. Residues contributing side chain and main chain oxygens that coordinate Na2 are shown as sticks with LeuT residues labeled.

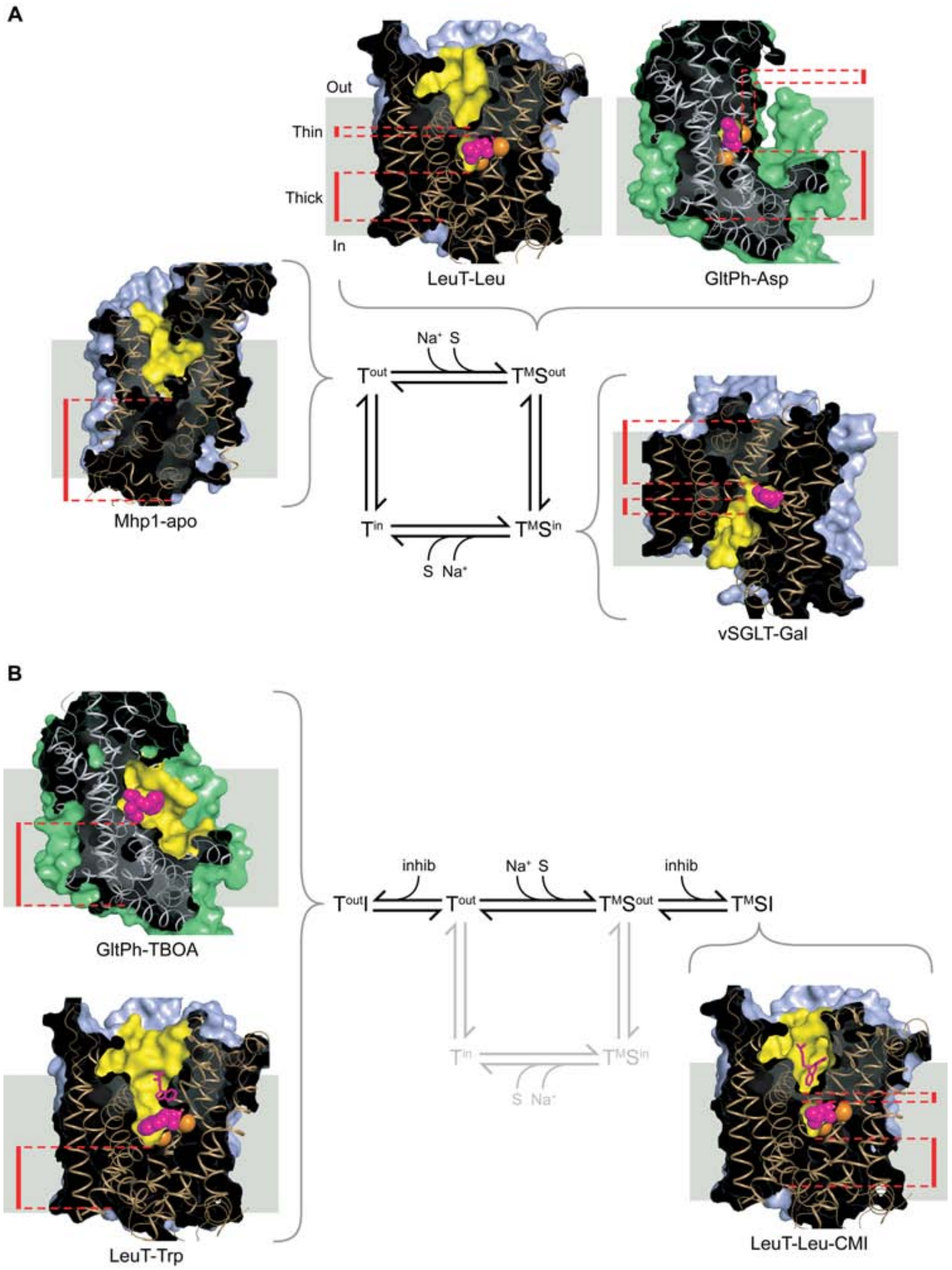
A
Out
Thin
Thick
In
LeuT-Leu
GltPh-Asp
Mhp1-apo
vSGLT-Gal
Na⁺ S
T^out
T^M S^out
T^in
T^M S^in
S Na⁺
B
GltPh-TBOA
LeuT-Trp
LeuT-Leu-CMI
inhib
Na⁺ S
inhib
T^out I
T^out
T^M S^out
T^M SI
T^in
T^M S^in
S Na⁺

Figure 5.4. Crystal structures of transport intermediates. (**A**) Transport cycle based upon an alternating access type mechanism together with insights from crystallographic studies. Known transporter structures that represent intermediate states are shown. Clockwise from the T^{out} state: Mhp1-apo (PDB 2JLN), LeuT-Leu (PDB 2A65), GltPh-Asp (PDB 2NWX), vSGLT-Gal (PDB 3DH4). (**B**) The inhibitory branches of the transport cycle from panel (**A**). On the left, structures of GltPh-TBOA (PDB 2NWW) and LeuT-Trp (PDB 3F3A) represent an open-to-out competitive-inhibitor bound state. On the right, the structure of LeuT-Leu-CMI (PDB 2Q6H) represents a non-competitive inhibitor-bound occluded state. Cross-sectional illustrations of the crystal structures of each transporter are shown associated with the states of the cycle that they represent. The positions of the 'thin' gates and 'thick' gates are highlighted by red dashed lines. The solvent-accessible surface area, calculated with a probe radius of 1.4 Å, is shown in light blue for the LeuT-fold structures or green for GltPh-fold structures. The yellow regions highlight the surfaces of the binding site and cavities that penetrate the structures. Bound ligands, shown as van der Waals spheres, are colored magenta, with sodium ions colored orange. The view of each transporter is approximately parallel to the membrane plane, with the extracellular side at the top of each figure.

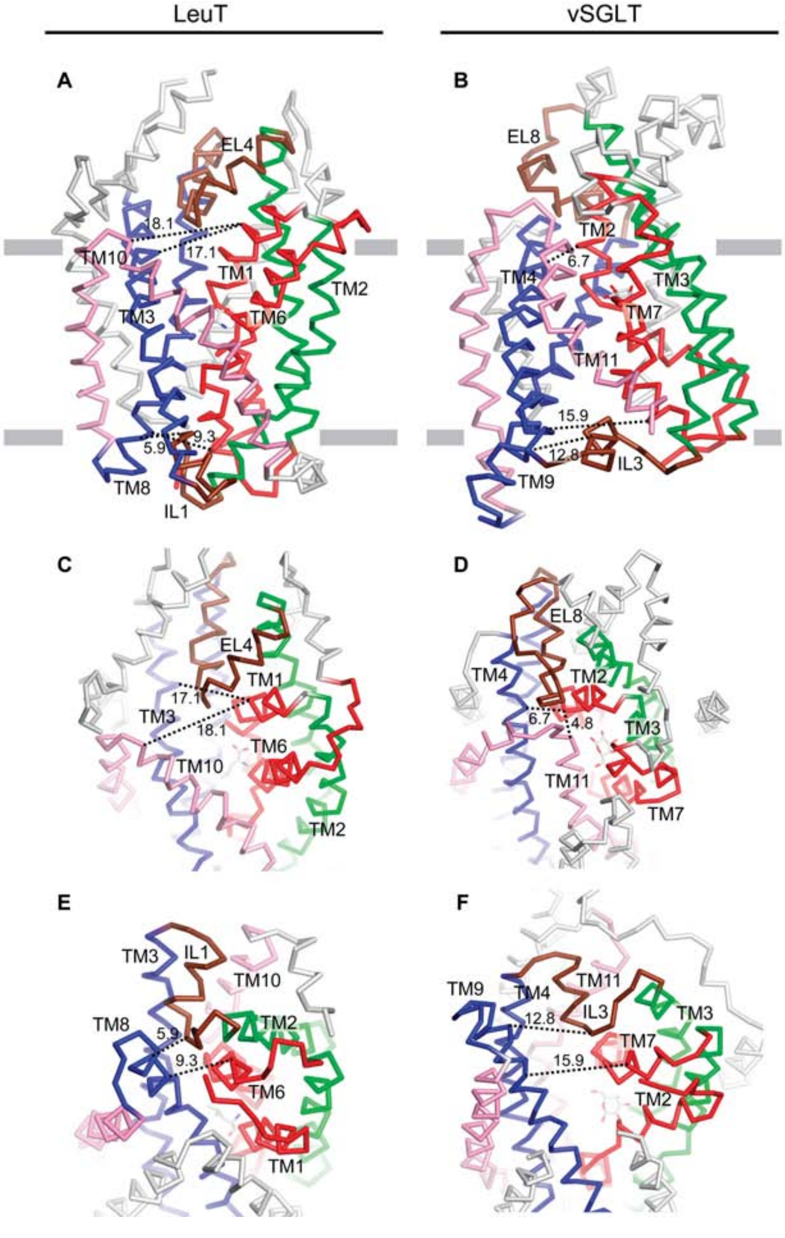
LeuT
vSGLT
A
EL4
8.1
17.1
TM10
TM1
TM2
TM3
TM6
5.9
9.3
TM8
IL1
B
EL8
TM2
6.7
TM4
TM3
TM7
TM11
15.9
12.8
IL3
TM9
C
EL4
TM1
17.1
TM3
18.1
TM6
TM10
TM2
D
EL8
TM4
TM2
6.7
4.8
TM3
TM11
TM7
E
TM3
IL1
TM10
TM8
TM2
5.9
9.3
TM6
TM1
F
TM9
TM4
TM11
IL3
TM3
12.8
TM7
15.9
TM2

Figure 5.5. Comparative views of substrate-bound LeuT (PDB 2A65, panels A, C, E) and vSGLT (PDB 3DH4, panels B, D, F). (**A**) and (**B**) show membrane-parallel views of LeuT and vSGLT. (**C**) and (**D**) show a top-down view of the extracellular pathway. (**E**) and (**F**) show a bottom-up view of the intracellular pathway. Equivalent structural elements are colored the same in both LeuT and vSGLT. To help gauge the re-organization of the extra- and intracellular elements, black dashed lines indicate distance measurements between structural elements, measured from structurally similar residues in the two transporters. Considering the internal two-fold symmetry, note the similar organization of the open LeuT extracellular pathway to the open vSGLT intracellular pathway, and the similarity of the closed vSGLT extracellular pathway to the closed LeuT intracellular pathway.

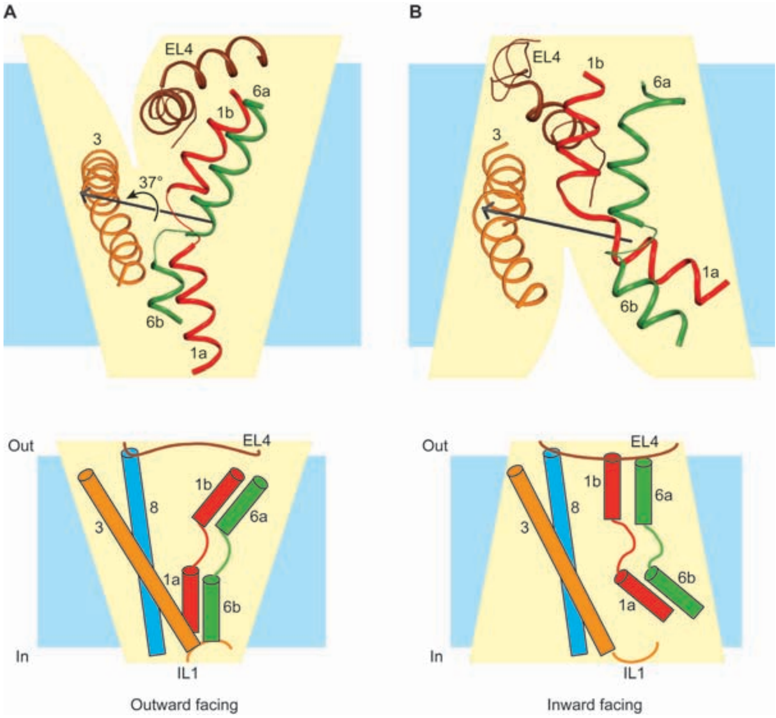

Figure 5.6. Transition between outward-facing and inward-facing states in LeuT-fold transporters. TMs 1 (red), 3 (orange), 6 (green), and 8 line the central translocation pathway with EL4 and IL1 acting as lids that seal the extracellular and intracellular gates, respectively, in their closed states. (**A**) The outward-facing arrangement of central helices in substrate-bound LeuT. (**B**) The inward-facing arrangement of central helices in substrate-bound vSGLT, with LeuT numbering for comparison with panel a. TM 8 and IL1 are omitted from the figure for clarity. TMs 1 and 6 rotate approximately 37 degrees relative to TMs 3 and 8 in transitioning from the outward-facing state adopted by LeuT in (**A**) to the inward-facing state adopted by vSGLT in (**B**). The rotation axis, shown in black, and the angle of rotation were calculated using DynDom [213]. Cartoon representations of outward-facing and inward-facing states, adapted from Yamashita et al, [59] are shown below the corresponding ribbon diagrams.

REFERENCES

1. Widdas, W.F., *Inability of diffusion to account for placental glucose transfer in the sheep and consideration of the kinetics of a possible carrier transfer.* J Physiol, 1952. **118**(1): p. 23-39.

2. Hille, B., *Ionic channels in excitable membranes. Current problems and biophysical approaches.* Biophys J, 1978. **22**(2): p. 283-94.

3. Hodgkin, A.L. and A.F. Huxley, *A quantitative description of membrane current and its application to conduction and excitation in nerve.* J Physiol, 1952. **117**(4): p. 500-44.

4. Jardetzky, O., *Simple allosteric model for membrane pumps.* Nature, 1966. **211**(52): p. 969-70.

5. Mitchell, P., *A general theory of membrane transport from studies of bacteria.* Nature, 1957. **180**: p. 134-136.

6. Mitchell, P., *Translocations through natural membranes*, in *Advances in enzymology and related areas of molecular biology*, F.F. Nord, Editor. 1967, Interscience Publishers: Bronx, New York. p. 33-87.

7. Patlak, C.S., *Contributions to the theory of active transport: II. The gate type non-carrier mechanism and generalizations concerning tracer flow, efficiency, and measurement of energy expenditure.* Bull. Math. Biophysics, 1957. **19**: p. 209-235.

8. Vidaver, G.A., *Inhibition of parallel flux and augmentation of counter flux shown by transport models not involving a mobile carrier.* J. Theoret. Biol., 1966. **10**: p. 301-306.

9. Glynn, I.M., *A hundred years of sodium pumping.* Annu Rev Physiol, 2002. **64**: p. 1-18.

10. Saier, M.H., Jr., *A functional-phylogenetic classification system for transmembrane solute transporters.* Microbiol Mol Biol Rev, 2000. **64**: p. 354-411.

11. Saier, M.H., Jr., C.V. Tran, and R.D. Barabote, *TCDB: the Transporter Classification Database for membrane transport protein analyses and information.* Nucleic Acids Res, 2006. **34**(Database issue): p. D181-6.

12. Morth, J.P., et al., *A structural overview of the plasma membrane Na(+),K(+)-ATPase and H(+)-ATPase ion pumps.* Nat Rev Mol Cell Biol, 2011. **12**(1): p. 60-70.

13. Christensen, H.N., T.R. Riggs, and N.E. Ray, *Concentrative uptake of amino acids by erythrocytes in vitro.* J Biol Chem, 1952. **194**(1): p. 41-51.

14. Ussing, H.H., *The active ion transport through the isolated frog skin in the light of tracer studies.* Acta Physiol Scand, 1949. **17**(1): p. 1-37.

15. Ussing, H.H. and K. Zerahn, *Active transport of sodium as the source of electric current in the short-circuited isolated frog skin.* Acta Physiol Scand, 1951. **23**(2-3): p. 110-27.

16. Ussing, H.H., *The frog skin potential.* J Gen Physiol, 1960. **43**: p. 135-47.

17. Zerahn, K., *Oxygen consumption and active sodium transport in the isolated and short-circuited frog skin.* Acta Physiol Scand, 1956. **36**(4): p. 300-18.

18. Skou, J.C., *The influence of some cations on an adenosine triphosphatase from peripheral nerves.* Biochim Biophys Acta, 1957. **23**(2): p. 394-401.

19. Crane, R.K., *Intestinal absorption of sugars.* Physiol Rev, 1960. **40**: p. 789-825.

20. Csaky, T.Z. and M. Thale, *Effect of ionic environment on intestinal sugar transport.* J Physiol, 1960. **151**: p. 59-65.

21. Schultz, S.G. and P.F. Curran, *Coupled transport of sodium and organic solutes.* Physiol Rev, 1970. **50**(4): p. 637-718.

22. Hediger, M.A., et al., *Expression cloning and cDNA sequencing of the Na+/glucose co-transporter.* Nature, 1987. **330**(6146): p. 379-81.

23. Wells, R.G., et al., *Cloning of a human kidney cDNA with similarity to the sodium-glucose cotransporter.* Am J Physiol, 1992. **263**(3 Pt 2): p. F459-65.

24. Wright, E.M. and E. Turk, *The sodium/glucose cotransport family SLC5.* Pflugers Arch, 2004. **447**(5): p. 510-8.

25. Faham, S., et al., *The crystal structure of a sodium galactose transporter reveals mechanistic insights into Na+/sugar symport.* Science, 2008. **321**(5890): p. 810-4.

26. Whitby, L.G., J. Axelrod, and H. Weil-Malherbe, *The fate of H3-norepinephrine in animals.* J Pharmacol Exp Ther, 1961. **132**: p. 193-201.

27. Herting, G., J. Axelrod, and L.G. Whitby, *Effect of drugs on the uptake and metabolism of H3-norepinephrine.* J Pharmacol Exp Ther, 1961. **134**: p. 146-53.

28. Iversen, L.L., *The Uptake of Noradrenaline by the Isolated Perfused Rat Heart.* Br J Pharmacol Chemother, 1963. **21**: p. 523-37.

29. Iversen, L.L. and E.A. Kravitz, *Sodium dependence of transmitter uptake at adrenergic nerve terminals.* Mol Pharmacol, 1966. **2**(4): p. 360-2.

30. Iversen, L.L. and M.J. Neal, *The uptake of [3H]GABA by slices of rat cerebral cortex.* J Neurochem, 1968. **15**(10): p. 1141-9.

31. Ross, S.B. and A.L. Renyi, *Inhibition of the uptake of tritiated catecholamines by antidepressant and related agents.* Eur J Pharmacol, 1967. **2**(3): p. 181-6.

32. Ross, S.B., A.L. Renyi, and B. Brunfelter, *Cocaine-sensitive uptake of sympathomimetic amines in nerve tissue.* J Pharm Pharmacol, 1968. **20**(4): p. 283-8.

33. Born, G.V. and R.E. Gillson, *Studies on the uptake of 5-hydroxytryptamine by blood platelets.* J Physiol, 1959. **146**(3): p. 472-91.

34. Sneddon, J.M., *Sodium-dependent accumulation of 5-hydroxytryptamine by rat blood platelets.* Br J Pharmacol, 1969. **37**(3): p. 680-8.

35. Stacey, R.S., *Uptake of 5-hydroxytryptamine by platelets.* Br J Pharmacol Chemother, 1961. **16**(3): p. 284-95.

36. Todrick, A. and A.C. Tait, *The inhibition of human platelet 5-hydroxytryptamine uptake by tricyclic antidepressive drugs. The relation between structure and potency.* J Pharm Pharmacol, 1969. **21**(11): p. 751-62.

37. Iversen, L.L., *Role of transmitter uptake mechanisms in synaptic neurotransmission.* Br J Pharmacol, 1971. **41**(4): p. 571-91.

38. Kaback, H.R., *Transport across isolated bacterial cytoplasmic membranes.* Biochim Biophys Acta, 1972. **265**(3): p. 367-416.

39. Kaback, H.R., *Transport studies in bacterial membrane vesicles.* Science, 1974. **186**(4167): p. 882-92.

40. Kanner, B.I., *Active transport of gamma-aminobutyric acid by membrane vesicles isolated from rat brain.* Biochemistry, 1978. **17**(7): p. 1207-11.

41. Kanner, B.I., A. Bendahan, and R. Radian, *Efflux and exchange of gamma-aminobutyric acid and nipecotic acid catalysed by synaptic plasma membrane vesicles isolated from immature rat brain.* Biochim Biophys Acta, 1983. **731**(1): p. 54-62.

42. Kanner, B.I. and L. Kifer, *Efflux of gamma-aminobutyric acid by synaptic plasma membrane vesicles isolated from rat brain.* Biochemistry, 1981. **20**(12): p. 3354-8.

43. Rudnick, G., *Active transport of 5-hydroxytryptamine by plasma membrane vesicles isolated from human blood platelets.* J Biol Chem, 1977. **252**(7): p. 2170-4.

44. Kanner, B.I. and S. Schuldiner, *Mechanism of transport and storage of neurotransmitters.* CRC Crit Rev Biochem, 1987. **22**(1): p. 1-38.

45. Lester, H.A., et al., *Permeation properties of neurotransmitter transporters.* Annu Rev Pharmacol Toxicol, 1994. **34**: p. 219-49.

46. Rudnick, G. and J. Clark, *From synapse to vesicle: the reuptake and storage of biogenic amine neurotransmitters.* Biochim Biophys Acta, 1993. **1144**(3): p. 249-63.

47. Johnstone, R.M., *Ion-coupled cotransport.* Curr Opin Cell Biol, 1990. **2**(4): p. 735-41.

48. Krogsgaard-Larsen, P., et al., *GABA uptake inhibitors: relevance to antiepileptic drug research.* Epilepsy Res, 1987. **1**(2): p. 77-93.

49. Radian, R., A. Bendahan, and B.I. Kanner, *Purification and identification of the functional sodium- and chloride-coupled gamma-aminobutyric acid transport glycoprotein from rat brain.* J Biol Chem, 1986. **261**(33): p. 15437-41.

50. Guastella, J., et al., *Cloning and expression of a rat brain GABA transporter.* Science, 1990. **249**(4974): p. 1303-6.

51. Pacholczyk, T., R.D. Blakely, and S.G. Amara, *Expression cloning of a cocaine- and antidepressant-sensitive human noradrenaline transporter.* Nature, 1991. **350**(6316): p. 350-4.

52. Kilty, J.E., D. Lorang, and S.G. Amara, *Cloning and expression of a cocaine-sensitive rat dopamine transporter.* Science, 1991. **254**(5031): p. 578-9.

53. Shimada, S., et al., *Cloning and expression of a cocaine-sensitive dopamine transporter complementary DNA.* Science, 1991. **254**(5031): p. 576-8.

54. Blakely, R.D., et al., *Cloning and expression of a functional serotonin transporter from rat brain.* Nature, 1991. **354**(6348): p. 66-70.

55. Hoffman, B.J., E. Mezey, and M.J. Brownstein, *Cloning of a serotonin transporter affected by antidepressants.* Science, 1991. **254**(5031): p. 579-80.

56. Androutsellis-Theotokis, A., et al., *Characterization of a functional bacterial homologue of sodium-dependent neurotransmitter transporters.* J Biol Chem, 2003. **278**(15): p. 12703-9.

57. Quick, M., et al., *State-dependent conformations of the translocation pathway in the tyrosine transporter Tyt1, a novel neurotransmitter:sodium symporter from Fusobacterium nucleatum.* J Biol Chem, 2006. **281**(36): p. 26444-54.

58. Trotschel, C., et al., *Methionine Uptake in Corynebacterium glutamicum by MetQNI and by MetPS, a Novel Methionine and Alanine Importer of the NSS Neurotransmitter Transporter Family.* Biochemistry, 2008. **47**(48): p. 12698-709.

59. Yamashita, A., et al., *Crystal structure of a bacterial homologue of Na+/Cl--dependent neurotransmitter transporters.* Nature, 2005. **437**(7056): p. 215-23.

60. Hahn, M.K. and R.D. Blakely, *The functional impact of SLC6 transporter genetic variation.* Annu Rev Pharmacol Toxicol, 2007. **47**: p. 401-41.

61. Andersen, J., et al., *Recent advances in the understanding of the interaction of antidepressant drugs with serotonin and norepinephrine transporters.* Chem Commun (Camb), 2009(25): p. 3677-92.

62. Jones, S.R., et al., *Mechanisms of amphetamine action revealed in mice lacking the dopamine transporter.* J Neurosci, 1998. **18**(6): p. 1979-86.

63. Rudnick, G. and S.C. Wall, *Non-neurotoxic amphetamine derivatives release serotonin through serotonin transporters.* Mol Pharmacol, 1993. **43**(2): p. 271-6.

64. Sulzer, D., N.T. Maidment, and S. Rayport, *Amphetamine and other weak bases act to promote reverse transport of dopamine in ventral midbrain neurons.* J Neurochem, 1993. **60**(2): p. 527-35.

65. Binda, F., et al., *Syntaxin 1A interaction with the dopamine transporter promotes amphetamine-induced dopamine efflux.* Mol Pharmacol, 2008. **74**(4): p. 1101-8.

66. Granas, C., et al., *N-terminal truncation of the dopamine transporter abolishes phorbol ester- and substance P receptor-stimulated phosphorylation without impairing transporter internalization.* J Biol Chem, 2003. **278**(7): p. 4990-5000.

67. Fog, J.U., et al., *Calmodulin kinase II interacts with the dopamine transporter C terminus to regulate amphetamine-induced reverse transport.* Neuron, 2006. **51**(4): p. 417-29.

68. Segel, I.H., *Enzyme Kinetics : Behavior and Analysis of Rapid Equilibrium and Steady State Enzyme Systems*. 1975, New York: Wiley. xxii, 957.

69. Beuming, T., et al., *A comprehensive structure-based alignment of prokaryotic and eukaryotic neurotransmitter/Na+ symporters (NSS) aids in the use of the LeuT structure to probe NSS structure and function.* Mol. Pharmacol., 2006. **70**: p. 1630-1642.

70. Screpanti, E. and C. Hunte, *Discontinuous membrane helices in transport proteins and their correlation with function.* J Struct Biol, 2007. **159**(2): p. 261-7.

71. Kniazeff, J., et al., *An intracellular interaction network regulates conformational transitions in the dopamine transporter.* J Biol Chem, 2008. **283**(25): p. 17691-701.

72. Forrest, L.R., et al., *Mechanism for alternating access in neurotransmitter transporters.* Proc Natl Acad Sci U S A, 2008. **105**(30): p. 10338-43.

73. Forrest, L.R., et al., *Identification of a chloride ion binding site in Na+/Cl- -dependent transporters.* Proc. Natl. Acad. Sci. USA, 2007. **104**: p. 12761-12766.

74. Zomot, E., et al., *Mechanism of chloride interaction with neurotransmitter:sodium symporters.* Nature, 2007. **449**(7163): p. 726-30.

75. Singh, S.K., et al., *A competitive inhibitor traps LeuT in an open-to-out conformation.* Science, 2008. **322**(5908): p. 1655-61.

76. Singh, S.K., A. Yamashita, and E. Gouaux, *Antidepressant binding site in a bacterial homologue of neurotransmitter transporters.* Nature, 2007. **448**(7156): p. 952-6.

77. Zhou, Z., et al., *LeuT-desipramine structure reveals how antidepressants block neurotransmitter reuptake.* Science, 2007. **317**(5843): p. 1390-3.

78. Zhou, Z., et al., *Antidepressant specificity of serotonin transporter suggested by three LeuT-SSRI structures.* Nat Struct Mol Biol, 2009. **16**(6): p. 652-7.

79. Jaronczyk, M., et al., *The molecular interactions of buspirone analogues with the serotonin transporter.* Bioorg Med Chem, 2008. **16**(20): p. 9283-94.

80. Zhang, P., et al., *Structure-activity relationships for a novel series of citalopram (1-(3-(dimethylamino)propyl)-1-(4-fluorophenyl)-1,3-dihydroisobenzofuran-5 -carbonitrile) analogues at monoamine transporters.* J Med Chem, 2010. **53**(16): p. 6112-21.

81. Skovstrup, S., et al., *Homology modelling of the GABA transporter and analysis of tiagabine binding.* ChemMedChem, 2010. **5**(7): p. 986-1000.

82. Gedeon, P.C., et al., *Molecular dynamics of leucine and dopamine transporter proteins in a model cell membrane lipid bilayer.* Proteins, 2010. **78**(4): p. 797-811.

83. Wein, T. and K.T. Wanner, *Generation of a 3D model for human GABA transporter hGAT-1 using molecular modeling and investigation of the binding of GABA.* J Mol Model, 2010. **16**(1): p. 155-61.

84. Ravna, A.W., I. Sylte, and S.G. Dahl, *Structure and localisation of drug binding sites on neurotransmitter transporters.* J Mol Model, 2009. **15**(10): p. 1155-64.

85. Beuming, T., et al., *The binding sites for cocaine and dopamine in the dopamine transporter overlap.* Nat Neurosci, 2008. **11**(7): p. 780-9.

86. Jorgensen, A.M., et al., *Homology modeling of the serotonin transporter: insights into the primary escitalopram-binding site.* ChemMedChem, 2007. **2**(6): p. 815-26.

87. Sen, N., et al., *A pincer-like configuration of TM2 in the human dopamine transporter is responsible for indirect effects on cocaine binding.* Neuropharmacology, 2005. **49**(6): p. 780-90.

88. Torres-Altoro, M.I., et al., *Structural analysis of the extracellular entrance to the serotonin transporter permeation pathway.* J Biol Chem, 2010. **285**(20): p. 15369-79.

89. Field, J.R., L.K. Henry, and R.D. Blakely, *Transmembrane domain 6 of the human serotonin transporter contributes to an aqueously accessible binding pocket for serotonin and the psychostimulant 3,4-methylene dioxymethamphetamine.* J Biol Chem, 2010. **285**(15): p. 11270-80.

90. Indarte, M., J.D. Madura, and C.K. Surratt, *Dopamine transporter comparative molecular modeling and binding site prediction using the LeuT(Aa) leucine transporter as a template.* Proteins, 2008. **70**(3): p. 1033-46.

91. Piscitelli, C.L., H. Krishnamurthy, and E. Gouaux, *Neurotransmitter/sodium symporter orthologue LeuT has a single high-affinity substrate site.* Nature, 2010. **468**(7327): p. 1129-32.

92. Claxton, D.P., et al., *Ion/substrate-dependent conformational dynamics of a bacterial homolog of neurotransmitter:sodium symporters.* Nat Struct Mol Biol, 2010. **17**(7): p. 822-9.

93. Zhao, Y., et al., *Single-molecule dynamics of gating in a neurotransmitter transporter homologue.* Nature, 2010. **465**(7295): p. 188-93.

94. Zhao, Y., et al., *Substrate-dependent proton antiport in neurotransmitter:sodium symporters.* Nat Chem Biol, 2010. **6**(2): p. 109-16.

95. Shi, L., et al., *The mechanism of a neurotransmitter:sodium symporter--inward release of Na+ and substrate is triggered by substrate in a second binding site.* Mol Cell, 2008. **30**(6): p. 667-77.

96. Dodd, J.R. and D.L. Christie, *Selective amino acid substitutions convert the creatine transporter to a gamma-aminobutyric acid transporter.* J Biol Chem, 2007. **282**(21): p. 15528-33.

97. Vandenberg, R.J., K. Shaddick, and P. Ju, *Molecular basis for substrate discrimination by glycine transporters.* J Biol Chem, 2007. **282**(19): p. 14447-53.

98. Broer, A., et al., *Sodium translocation by the iminoglycinuria associated imino transporter (SLC6A20).* Mol Membr Biol, 2009. **26**(5): p. 333-46.

99. Shi, L. and H. Weinstein, *Conformational rearrangements to the intracellular open states of the LeuT and ApcT transporters are modulated by common mechanisms.* Biophys J, 2010. **99**(12): p. L103-5.

100. Shaikh, S.A. and E. Tajkhorshid, *Modeling and dynamics of the inward-facing state of a Na+/Cl- dependent neurotransmitter transporter homologue.* PLoS Comput Biol, 2010. **6**(8).

101. Yu, H., S.Y. Noskov, and B. Roux, *Two mechanisms of ion selectivity in protein binding sites.* Proc Natl Acad Sci U S A, 2010. **107**(47): p. 20329-34.

102. Miloshevsky, G.V., A. Hassanein, and P.C. Jordan, *Shape-Dependent Global Deformation Modes of Large Protein Structures.* J Mol Struct, 2010. **972**(1-3): p. 41-50.

103. Li, J. and E. Tajkhorshid, *Ion-releasing state of a secondary membrane transporter.* Biophys J, 2009. **97**(11): p. L29-31.

104. Caplan, D.A., J.O. Subbotina, and S.Y. Noskov, *Molecular mechanism of ion-ion and ion-substrate coupling in the Na+-dependent leucine transporter LeuT.* Biophys J, 2008. **95**(10): p. 4613-21.

105. Noskov, S.Y. and B. Roux, *Control of ion selectivity in LeuT: two Na+ binding sites with two different mechanisms.* J Mol Biol, 2008. **377**(3): p. 804-18.

106. Celik, L., B. Schiott, and E. Tajkhorshid, *Substrate binding and formation of an occluded state in the leucine transporter.* Biophys J, 2008. **94**(5): p. 1600-12.

107. Jorgensen, A.M., et al., *Molecular dynamics simulations of Na+/Cl(-)-dependent neurotransmitter transporters in a membrane-aqueous system.* ChemMedChem, 2007. **2**(6): p. 827-40.

108. Boudker, O., et al., *Coupling substrate and ion binding to extracellular gate of a sodium-dependent aspartate transporter.* Nature, 2007. **445**(7126): p. 387-93.

109. Yernool, D., et al., *Structure of a glutamate transporter homologue from Pyrococcus horikoshii.* Nature, 2004. **431**(7010): p. 811-8.

110. Parsons, S.M., *Transport mechanisms in acetylcholine and monoamine storage.* FASEB J., 2000. **14**(15): p. 2423-34.

111. Roux, M.J. and S. Supplisson, *Neuronal and glial glycine transporters have different stoichiometries.* Neuron, 2000. **25**(2): p. 373-83.

112. Zerangue, N. and M.P. Kavanaugh, *Flux coupling in a neuronal glutamate transporter.* Nature, 1996. **383**(6601): p. 634-7.

113. Chen, N.H., M.E. Reith, and M.W. Quick, *Synaptic uptake and beyond: the sodium- and chloride-dependent neurotransmitter transporter family SLC6.* Pflugers Arch., 2004. **447**(5): p. 519-31.

114. Kanner, B.I., *Structure and function of sodium-coupled GABA and glutamate transporters.* J. Membr. Biol., 2006. **213**(2): p. 89-100.

115. Warskulat, U., et al., *The osmolyte strategy of normal human keratinocytes in maintaining cell homeostasis.* J. Invest. Dermatol., 2004. **123**(3): p. 516-21.

116. Masson, J., et al., *Neurotransmitter transporters in the central nervous system.* Pharm. Rev., 1999. **51**: p. 439-464.

117. Hahn, M.K. and R.D. Blakely, *Monoamine transporter gene structure and polymorphisms in relation to psychiatric and other complex disorders.* Pharmacogenomics J., 2002. **2**(4): p. 217-35.

118. Ozaki, N., et al., *Serotonin transporter missense mutation associated with a complex neuropsychiatric phenotype.* Mol. Psychiatry, 2003. **8**(11): p. 933-6.

119. Richerson, G.B. and Y. Wu, *Role of the GABA transporter in epilepsy.* Adv. Exp. Med. Biol., 2004. **548**: p. 76-91.

120. Sutcliffe, J.S., et al., *Allelic heterogeneity at the serotonin transporter locus (SLC6A4) confers susceptibility to autism and rigid-compulsive behaviors.* Am. J. Hum. Genet., 2005. **77**(2): p. 265-79.

121. Shannon, J.R., et al., *Orthostatic intolerance and tachycardia associated with norepinephrine-transporter deficiency.* N Engl J Med, 2000. **342**(8): p. 541-9.

122. Salomons, G.S., et al., *X-linked creatine-transporter gene (SLC6A8) defect: a new creatine-deficiency syndrome.* Am. J. Hum. Genet. , 2001. **68**: p. 1497-1500.

123. Heller-Stilb, B., et al., *Disruption of the taurine transporter gene (taut) leads to retinal degeneration in mice.* FASEB J., 2002. **16**(2): p. 231-3.

124. Barker, E.L. and R.D. Blakely, *Norepinephrine and serotonin transporters: molecular targets of antidepressant drugs*, in *Psychopharmacology - the Fourth Generation of Progress*, F.E. Bloom and D.J. Kupfer, Editors. 2000, Raven Press: New York.

125. Krogsgaard-Larsen, P., B. Frolund, and K. Frydenvang, *GABA uptake inhibitors. Design, molecular pharmacology and therapeutic aspects.* Curr. Pharm. Des., 2000. **6**(12): p. 1193-209.

126. Amara, S.G. and M.S. Sonders, *Neurotransmitter transporters as molecular targets for addictive drugs.* Drug Alcohol Depend., 1998. **51**(1-2): p. 87-96.

127. Talvenheimo, J., P.J. Nelson, and G. Rudnick, *Mechanism of imipramine inhibition of platelet 5-hydroxytryptamine transport.* J Biol Chem, 1979. **254**(11): p. 4631-5.

128. Apparsundaram, S., et al., *Antidepressants Targeting the Serotonin Reuptake Transporter (Sert) Act Via a Competitive Mechanism.* J Pharmacol Exp Ther, 2008.

129. Kimelberg, H.K. and E.W. Pelton, 2nd, *High-affinity uptake of [3H]norepinephrine by primary astrocyte cultures and its inhibition by tricyclic antidepressants.* J Neurochem, 1983. **40**(5): p. 1265-70.

130. Henry, L.K., et al., *Tyr-95 and Ile-172 in transmembrane segments 1 and 3 of human serotonin transporters interact to establish high affinity recognition of antidepressants.* J Biol Chem, 2006. **281**(4): p. 2012-23.

131. Cheng, Y. and W.H. Prusoff, *Relationship between the inhibition constant (K1) and the concentration of inhibitor which causes 50 per cent inhibition (I50) of an enzymatic reaction.* Biochem Pharmacol, 1973. **22**(23): p. 3099-108.

132. Asquith, R.S. and D.E. Rivett, *Studies on the photooxidation of tryptophan.* Biochim Biophys Acta, 1971. **252**(1): p. 111-6.

133. Van Duyne, G.D., et al., *Atomic structures of the human immunophilin FKBP-12 complexes with FK506 and rapamycin.* J Mol Biol, 1993. **229**(1): p. 105-24.

134. Otwinowski, Z. and W. Minor, *Processing of X-ray diffraction data collected in oscillation mode.* Methods in Enzymology, 1997. **276**: p. 307-326.

135. Terwilliger, T.C. and J. Berendzen, *Automated MAD and MIR structure solution.* Acta Crystallogr D Biol Crystallogr, 1999. **55**(Pt 4): p. 849-61.

136. Vagin, A. and A. Teplyakov, *An approach to multi-copy search in molecular replacement.* Acta Crystallogr D Biol Crystallogr, 2000. **56**(Pt 12): p. 1622-4.

137. Navaza, J., *AMoRe: an automated package for molecular replacement.* Acta Crystallogr A, 1994. **50**: p. 157-163.

138. Murshudov, G.N., A.A. Vagin, and E.J. Dodson, *Refinement of macromolecular structures by the maximum-likelihood method.* Acta Crystallogr D Biol Crystallogr, 1997. **53**(Pt 3): p. 240-55.

139. Brunger, A.T., et al., *Crystallography & NMR system: A new software suite for macromolecular structure determination.* Acta Crystallogr D Biol Crystallogr, 1998. **54**(Pt 5): p. 905-21.

140. Hendrickson, W.A., *Determination of macromolecular structures from anomalous diffraction of synchrotron radiation.* Science, 1991. **254**(5028): p. 51-8.

141. Jones, T.A., et al., *Improved methods for building protein models in electron density maps and the location of errors in these models.* Acta Crystallogr A, 1991. **47**(Pt 2): p. 110-9.

142. Emsley, P. and K. Cowtan, *Coot: model-building tools for molecular graphics.* Acta Crystallogr D Biol Crystallogr, 2004. **60**(Pt 12,1): p. 2126-32.

143. Hayward, S. and R.A. Lee, *Improvements in the analysis of domain motions in proteins from conformational change: DynDom version 1.50.* J Mol Graph Model, 2002. **21**(3): p. 181-3.

144. Zhou, Y., E.R. Bennett, and B.I. Kanner, *The aqueous accessibility in the external half of transmembrane domain I of the GABA transporter GAT-1 Is modulated by its ligands.* J Biol Chem, 2004. **279**(14): p. 13800-8.

145. Rosenberg, A. and B.I. Kanner, *The substrates of the GABA transporter GAT-1 induce structural rearrangements around the interface of transmembrane domains 1 and 6.* J Biol Chem, 2008. **283**(21): p. 14376-83.

146. Henry, L.K., Adkins, E.M., Han, Q., and Blakely, R.D., *Serotonin and cocaine-sensitive inactivation of human serotonin transporters by methanethiosulfonates targeted to transmembrane domain I.* J Biol Chem, 2003. **278**(39): p. 37052-37063.

147. Hirayama, B.A., A. Diez-Sampedro, and E.M. Wright, *Common mechanisms of inhibition for the Na+/glucose (hSGLT1) and Na+/Cl-/GABA (hGAT1) cotransporters.* Br J Pharmacol, 2001. **134**(3): p. 484-95.

148. Weyand, S., et al., *Structure and molecular mechanism of a nucleobase-cation-symport-1 family transporter.* Science, 2008. **322**(5902): p. 709-13.

149. Echols, N., D. Milburn, and M. Gerstein, *MolMovDB: analysis and visualization of conformational change and structural flexibility.* Nucleic Acids Res, 2003. **31**(1): p. 478-82.

150. Krebs, W.G. and M. Gerstein, *The morph server: a standardized system for analyzing and visualizing macromolecular motions in a database framework.* Nucleic Acids Res, 2000. **28**(8): p. 1665-75.

151. Abramson, J. and E.M. Wright, *Structure and function of Na(+)-symporters with inverted repeats.* Curr Opin Struct Biol, 2009. **19**(4): p. 425-32.

152. Krishnamurthy, H., C.L. Piscitelli, and E. Gouaux, *Unlocking the molecular secrets of sodium-coupled transporters.* Nature, 2009. **459**(7245): p. 347-55.

153. Sobczak, I. and J.S. Lolkema, *Structural and mechanistic diversity of secondary transporters.* Curr Opin Microbiol, 2005. **8**: p. 161-167.

154. Shaffer, P.L., et al., *Structure and mechanism of a Na^+-independent amino acid transporter.* Science, 2009. **325**(5943): p. 1010-1014.

155. Gao, X., et al., *Structure and mechanism of an amino acid antiporter.* Science, 2009. **324**(5934): p. 1565-8.

156. Fang, Y., et al., *Structure of a prokaryotic virtual proton pump at 3.2 Å resolution.* Nature, 2009. **460**(7258): p. 1040-3.

157. Christensen, J.J., J.O. Hill, and R.M. Izatt, *Ion binding by synthetic macrocyclic compounds.* Science, 1971. **174**: p. 459-467.

158. Kawate, T. and E. Gouaux, *Fluorescence-detection size-exclusion chromatography for precrystallization screening of integral membrane proteins.* Structure, 2006. **14**(4): p. 673-681.

159. Wiseman, T., et al., *Rapid measurement of binding constants and heats of binding using a new titration calorimeter.* Anal Biochem, 1989. **179**(1): p. 131-7.

160. Quick, M. and J.A. Javitch, *Monitoring the function of membrane transport proteins in detergent-solubilized form.* Proc. Natl. Acad. Sci. USA, 2007. **104**: p. 3603-3608.

161. Hansen, S.B., et al., *Tryptophan fluorescence reveals conformational changes in the acetylcholine binding protein.* J Biol Chem, 2002. **277**(44): p. 41299-302.

162. Hill, A.V., *The combinations of haemoglobin with oxygen and with carbon monoxide. I.* Biochem J, 1913. **7**(5): p. 471-80.

163. Amara, S.G. and M.J. Kuhar, *Neurotransmitter transporters: recent progress.* Annu Rev Neurosci, 1993. **16**: p. 73-93.

164. Zahniser, N.R. and S. Doolen, *Chronic and acute regulation of Na+/Cl- -dependent neurotransmitter transporters: drugs, substrates, presynaptic receptors, and signaling systems.* Pharmacol Ther, 2001. **92**(1): p. 21-55.

165. Rudnick, G., *What is an antidepressant binding site doing in a bacterial transporter?* ACS Chem Biol, 2007. **2**(9): p. 606-9.

166. Arnold, K., et al., *The SWISS-MODEL workspace: a web-based environment for protein structure homology modelling.* Bioinformatics, 2006. **22**(2): p. 195-201.

167. Eswar, N., et al., *Comparative protein structure modeling using Modeller.* Curr Protoc Bioinformatics, 2006. **Chapter 5**: p. Unit 5 6.

168. Collaborative Computational Project, N., *The CCP4 suite: programs for protein crystallography.* Acta Crystallogr D Biol Crystallogr, 1994. **50**(Pt 5): p. 760-763.

169. Vagin, A.A., et al., *REFMAC5 dictionary: organization of prior chemical knowledge and guidelines for its use.* Acta Crystallogr D Biol Crystallogr, 2004. **60**(Pt 12, 1): p. 2184-95.

170. Kaplan, R.S. and P.L. Pedersen, *Determination of microgram quantities of protein in the presence of milligram levels of lipid with amido black 10B.* Anal Biochem, 1985. **150**(1): p. 97-104.

171. Kerwin, B.A. and R.L. Remmele, Jr., *Protect from light: photodegradation and protein biologics.* J Pharm Sci, 2007. **96**(6): p. 1468-79.

172. Vagin, A.A. and A. Teplayakov, *MOLREP: an Automated Program for Molecular Replacement.* J Appl Cryst, 1997. **30**(6): p. 1022-25.

173. Adams, P.D., et al., *PHENIX: building new software for automated crystallographic structure determination.* Acta Crystallogr. D., 2002. **58**: p. 1948-1954.

174. Davis, I.W., et al., *MolProbity: all-atom contacts and structure validation for proteins and nucleic acids.* Nucleic Acids Res., 2007. **35**: p. W375-83.

175. Cooley, R.B., D.J. Arp, and P.A. Karplus, *Evolutionary origin of a secondary structure: pi-helices as cryptic but widespread insertional variations of alpha-helices that enhance protein functionality.* J Mol Biol, 2010. **404**(2): p. 232-46.

176. Weaver, T.M., *The pi-helix translates structure into function.* Protein Sci, 2000. **9**(1): p. 201-6.

177. Quick, M.W., ed. *Transmembrane transporters*. Receptor Biochemistry and Methodology, ed. D.R. Sibley. 2002, Wiley-Liss, Inc.: Hoboken, NJ.

178. Chakrabarti, A.C. and D.W. Deamer, *Permeability of lipid bilayers to amino acids and phosphate.* Biochim. Biophys. Acta, 1992. **1111**: p. 171-177.

179. Supplisson, S. and M.J. Roux, *Why glycine transporters have different stoichiometries.* FEBS Lett, 2002. **529**: p. 93-101.

180. Hebert, S.C., D.B. Mount, and G. Gamba, *Molecular physiology of cation-coupled Cl- cotransport: the SLC12 family.* Pflugers Arch - Eur. J. Physiol., 2004. **447**: p. 580-593.

181. Sonders, M.S., M. Quick, and J.A. Javitch, *How did the neurotransmitter cross the bilayer? A closer view.* Curr. Opin. Neurobiol., 2005. **15**: p. 296-304.

182. Gamba, G., *Molecular physiology and pathophysiology of electroneutral cation-chloride cotransporters.* Physiol. Rev., 2005. **85**: p. 423-493.

183. Murphy, D.L., et al., *Serotonin transporter: gene, genetic disorders, and pharmacogenetics.* Mol. Interv., 2004. **4**: p. 109-123.

184. Busch, W. and M.H. Saier, Jr., *The transporter classification (TC) system, 2002.* Crit Rev Biochem Mol Biol, 2002. **37**(5): p. 287-337.

185. Hediger, M.A., et al., *The ABCs of solute carriers: physiological, pathological and therapeutic implications of human membrane transport proteins.* Pflugers Arch, 2004. **447**: p. 465-468.

186. Murakami, S., et al., *Crystal structure of bacterial multidrug efflux transporter AcrB.* Nature, 2002. **419**(6907): p. 587-593.

187. Huang, Y., et al., *Structure and mechanism of the glycerol-3-phosphate transporter from Escherichia coli.* Science, 2003. **301**(5633): p. 616-20.

188. Abramson, J., et al., *Structure and mechanism of the lactose permease of Escherichia coli.* Science, 2003. **301**(5633): p. 610-5.

189. Hunte, C., et al., *Structure of a Na+/H+ antiporter and insights into mechanism of action and regulation by pH.* Nature, 2005. **435**(7046): p. 1197-1202.

190. Barker, E.L., et al., *Transmembrane domain I contributes to the permeation pathway for serotonin and ions in the serotonin transporter.* J Neurosci, 1999. **19**(12): p. 4705-17.

191. Rudnick, G., *Serotonin transporters--structure and function.* J Membr Biol, 2006. **213**(2): p. 101-110.

192. Kanner, B.I. and E. Zomot, *Sodium-coupled neurotransmitter transporters.* Chem Rev, 2008. **108**(5): p. 1654-68.

193. Ben-Yona, A. and B.I. Kanner, *Transmembrane domain 8 of the gamma-aminobutyric acid transporter GAT-1 lines a cytoplasmic accessibility pathway into its binding pocket.* J Biol Chem, 2009. **284**(15): p. 9727-32.

194. Slotboom, D.J., J.S. Lolkema, and W.N. Konings, *Membrane topology of the C-terminal half of the neuronal, glial, and bacterial glutamate transporter family.* J. Biol. Chem., 1996. **271**(49): p. 31317-21.

195. Grunewald, M., A. Bendahan, and B.I. Kanner, *Biotinylation of single cysteine mutants of the glutamate transporter GLT-1 from rat brain reveals its unusual topology.* Neuron, 1998. **21**: p. 623-632.

196. Seal, R.P. and S.G. Amara, *A reentrant loop domain in the glutamate carrier EAAT1 participates in substrate binding and translocation.* Neuron, 1998. **21**(6): p. 1487-1498.

197. Toyoshima, C., et al., *Crystal structure of the calcium pump of sarcoplasmic reticulum at 2.6 A resolution.* Nature, 2000. **405**(6787): p. 647-55.

198. Dutzler, R., et al., *X-ray structure of a ClC chloride channel at 3.0 A reveals the molecular basis of anion selectivity.* Nature, 2002. **415**: p. 287-294.

199. Hilger, D., et al., *Role of Ser-340 and Thr-341 in transmembrane domain IX of the Na+/proline transporter PutP of Escherichia coli in ligand binding and transport.* J Biol Chem, 2008. **283**(8): p. 4921-9.

200. De la Vieja, A., et al., *Amino acid residues in transmembrane segment IX of the Na+/I- symporter play a role in its Na+ dependence and are critical for transport activity.* J Biol Chem, 2007. **282**(35): p. 25290-8.

201. Zhou, Y., E. Zomot, and B.I. Kanner, *Identification of a lithium interaction site in the gamma-aminobutyric acid (GABA) transporter GAT-1.* J Biol Chem, 2006. **281**(31): p. 22092-9.

202. Talvenheimo, J., et al., *The serotonin transporter-imipramine "receptor".* J Biol Chem, 1983. **258**(10): p. 6115-9.

203. Gu, H.H., S. Wall, and G. Rudnick, *Ion coupling stoichiometry for the norepinephrine transporter in membrane vesicles from stably transfected cells.* J Biol Chem, 1996. **271**(12): p. 6911-6.

204. Keynan, S. and B.I. Kanner, *gamma-Aminobutyric acid transport in reconstituted preparations from rat brain: coupled sodium and chloride fluxes.* Biochemistry, 1988. **27**(1): p. 12-7.

205. Diez-Sampedro, A., et al., *Na+-to-sugar stoichiometry of SGLT3.* Am J Physiol Renal Physiol, 2001. **280**(2): p. F278-82.

206. Mackenzie, B., D.D.F. Loo, and E.M. Wright, *Relationships Between Na+/Glucose Cotransporter (SGLT1) Currents and Fluxes.* Journal of Membrane Biology, 1998. **162**: p. 101-106.

207. Eskandari, S., et al., *Thyroid Na+/I- symporter. Mechanism, stoichiometry, and specificity.* J Biol Chem, 1997. **272**(43): p. 27230-8.

208. Kavanaugh, M.P., et al., *Mutation of an amino acid residue influencing potassium coupling in the glutamate transporter GLT-1 induces obligate exchange.* J Biol Chem, 1997. **272**(3): p. 1703-1708.

209. Keyes, S.R. and G. Rudnick, *Coupling of transmembrane proton gradients to platelet serotonin transport.* J Biol Chem, 1982. **257**(3): p. 1172-6.

210. Jacobs, M.T., et al., *Ibogaine, a noncompetitive inhibitor of serotonin transport, acts by stabilizing the cytoplasm-facing state of the transporter.* J Biol Chem, 2007. **282**(40): p. 29441-29447.

211. Zhang, Y.W. and G. Rudnick, *The cytoplasmic substrate permeation pathway of serotonin transporter.* J Biol Chem, 2006. **281**(47): p. 36213-20.

212. Zhang, Y.W. and G. Rudnick, *Cysteine-scanning mutagenesis of serotonin transporter intracellular loop 2 suggests an alpha-helical conformation.* J Biol Chem, 2005. **280**(35): p. 30807-13.

213. Hayward, S. and H.J. Berendsen, *Systematic analysis of domain motions in proteins from conformational change: new results on citrate synthase and T4 lysozyme.* Proteins, 1998. **30**(2): p. 144-54.